European Commission | Horizon 2020
European Union funding
for Research & Innovation

REDUCTION OF
RADIOLOGICAL
ACCIDENT
CONSEQUENCES

Action	Research and Innovation Action NFRP-2018-1
Grant Agreement #	847656
Project name	**R**eduction of **R**adiological **C**onsequences of design basis and design extension **A**ccidents
Project Acronym	R2CA
Project start date	01.09.2019
Deliverable #	D4.5
Title	**Final report on rod cladding failure due to secondary hydriding**
Author(s)	Cédric Leclere, Marine Guemas (IRSN), Francisco Feria, Luis Enrique Herranz (CIEMAT), Péter Szabó, Zoltán Hózer (EK), Paul Van Uffelen, Arndt Schubert (JRC)
Version	01
Related WP	WP4 SGTR
Related Task	T4.3. Secondary hydriding phenomena of defective fuel rods and its impact on failure behaviour (IRSN)
Lead organization	IRSN
Submission date	28.02.2023
Dissemination level	PU

This project has received funding from the Euratom research and training programme 2014-2018 under the grant agreement n° 847656

History

Date	Submitted by	Reviewed by	Version (Notes)
28.02.2023	C. Leclere (IRSN)	Z. Hózer (EK) N. Girault (IRSN)	01

Contents

List of Figures and Tables

1 Introduction

The task 4.3 is part of the more general work of the WP4 of the R2CA project dedicated to modeling improvements of key phenomena determining the fission product (FP) release into the environment during a SGTR accident for a better evaluation of their radiological consequences. For this purpose, in WP4 the three following topics were investigated:

- The FP transport and release from the primary circuit to the environment during a SGTR transient (incl. their behaviour in the failed steam generator).
- The FP release from defective fuel rods during a SGTR transient.
- The secondary hydriding phenomena of defective fuel rods and its impact on failure behavior.

This report deals with the latest topic only. The work carried out in task during the project was focused on the phenomena of secondary hydriding of Zr-based alloy claddings at temperatures representative of normal operating conditions (i.e. 300-400°C). Fuel rods in a Nuclear Power Plant can undergo primary defects in normal operation that lead to entry of water, secondary hydriding potentially initiated in the inner cladding part and the formation of weakening secondary defects. Such a phenomena during normal operating conditions have been thus a major issue for BWRs in the last 80s. Indeed, following secondary defect appearances, significant degradations of the defective fuel rod clad were observed mostly consisted in hydrides blisters or axial cracks and, in the most severe cases, in extended fractures.

In case of thermal-hydraulic loading of the weakened clad (as the change of pressure in the primary circuit following a SGTR), the potential clad failure can also lead to the ejection and dispersal of fuel fragments in the primary circuit, increasing drastically its contamination (through fuel fragment leaching). That is why, the risk of a cladding rupture due to this secondary hydriding phenomenon, deserves specific R&D efforts and the development/updating of dedicated models to characterize and simulate the formation/evolution of the brittle hydride zone in the cladding and its impact on the mechanical cladding response to a thermal-hydraulic load.

The final goal of this task in exploring the risk of defective fuel rod failures due to cladding ductility evolution when hydriding is then to better evaluate the radiological consequences of SGTR transients.

Six organizations were involved in this task. The main objectives were to update the models in the different existing simulation codes used within the project (i.e. in integral, fuel rod simulation and fuel performance codes) dealing with secondary hydriding phenomena of defective fuel rod cladding in normal operation conditions of a NPP. More especially it concerns:

- The identification of the different secondary hydriding processes
- The evaluation of the associated clad mechanical embrittlement

In addition, hydrogen uptake tests on Zr-based alloys have also been carried out to complete and enrich the existing database on the subject. Indeed, though there are a large number of tests available in the literature, most of them were carried out at temperatures higher than those of interest to us, i.e. representative of normal operating conditions in a NPP. These tests dedicated to support the improvements of numerical models on the hydrogen uptake process were conducted by EK (investigating two different Zr-based alloys) and were therefore performed between 300 and 400 °C. These new experimental measurements gained during the project advantageously complemented the other scarce experimental data collected within the R2CA database mostly issued from integral tests (i.e. DEFEX and HALDEN tests).

Several partners were involved in the modelling activities which resulted in implementation or refinements of the models already existing in (or coupled with) different codes (i.e. FRAPCON, SHOWBIZ and TRANSURANUS) and mainly related to the gas mixture/transport in the defective fuel rod gap, to the hydrogen re-distribution inside the clad after uptake and to the subsequent hydrogen precipitation/dissolution. From the new measurements performed in EK basic numerical correlations were also derived for the hydrogen uptake at normal condition temperatures.

In the following document, the work performed by each partner within the R2CA project during the two years that the task lasted is detailed.

2 EK: Experimental study of hydrogen uptake at reactor operational temperatures

2.1 Description

In case of steam generator tube rupture (SGTR) events the defective fuel rods may provide significant activity release into the primary coolant. Furthermore, the mechanical loads associated with the accident conditions can cause further degradation of the fuel rods as a consequence of following phenomena:

- The primary coolant may enter the defective fuel rods after the formation of defect.
- Hydrogen can be produced inside of the fuel rod as from water by different mechanism (radiolysis, corrosion).
- The hydrogen will be accumulated in the gas volume of fuel rod and a part of the available hydrogen will be absorbed by the zirconium cladding tube.
- The high local hydrogen content in some parts of the cladding can create hydride blisters and at those positions the cladding becomes very brittle.
- The change of pressure in the primary coolant and/or in the fuel rod will result in stresses that can lead to secondary failure of the fuel rod.

The understanding and detailed numerical modelling of the above listed phenomena need experimental data, which are representative for the physical parameters of the nuclear power plants (NPP).

In the present work the hydrogen uptake by two Zr alloys was addressed. There are a large number of tests available on hydrogen uptake of Zr [1][2][3][4][5], but most of them were carried out at high temperatures. In the defective fuel rods, during normal operational conditions the typical cladding temperatures are in the range of 300-400 °C.

Hydrogen uptake tests have been carried out Zircaloy-4 and E110G cladding tube samples between 300 and 400 °C in the laboratories of Centre for Energy Research (EK), Hungary [9]. The detailed information included in the database allow the R2CA participants to improve numerical models on the H uptake process.

The present report gives a short description of a simple model we improved based on the results of the H uptake tests that allows us to evaluate the hydrogen uptake rate of E110 ring samples in the above-mentioned temperature and pressure range. Using the model and the initial conditions of the original experiments, we calculated the partial pressure history during the measurements to compare it to the experimental one.

2.2 Hydrogen uptake tests with zirconium alloys

2.2.1 Test facility and sample preparation

The sample preparations and the tests were carried out in the laboratories of the Centre for Energy Research.

2.2.1.1 Test facility

The experimental set-up used for hydrogenation of Zr claddings is shown in Fig. 1., while the schematic view of the equipment can be seen in Fig. 2.

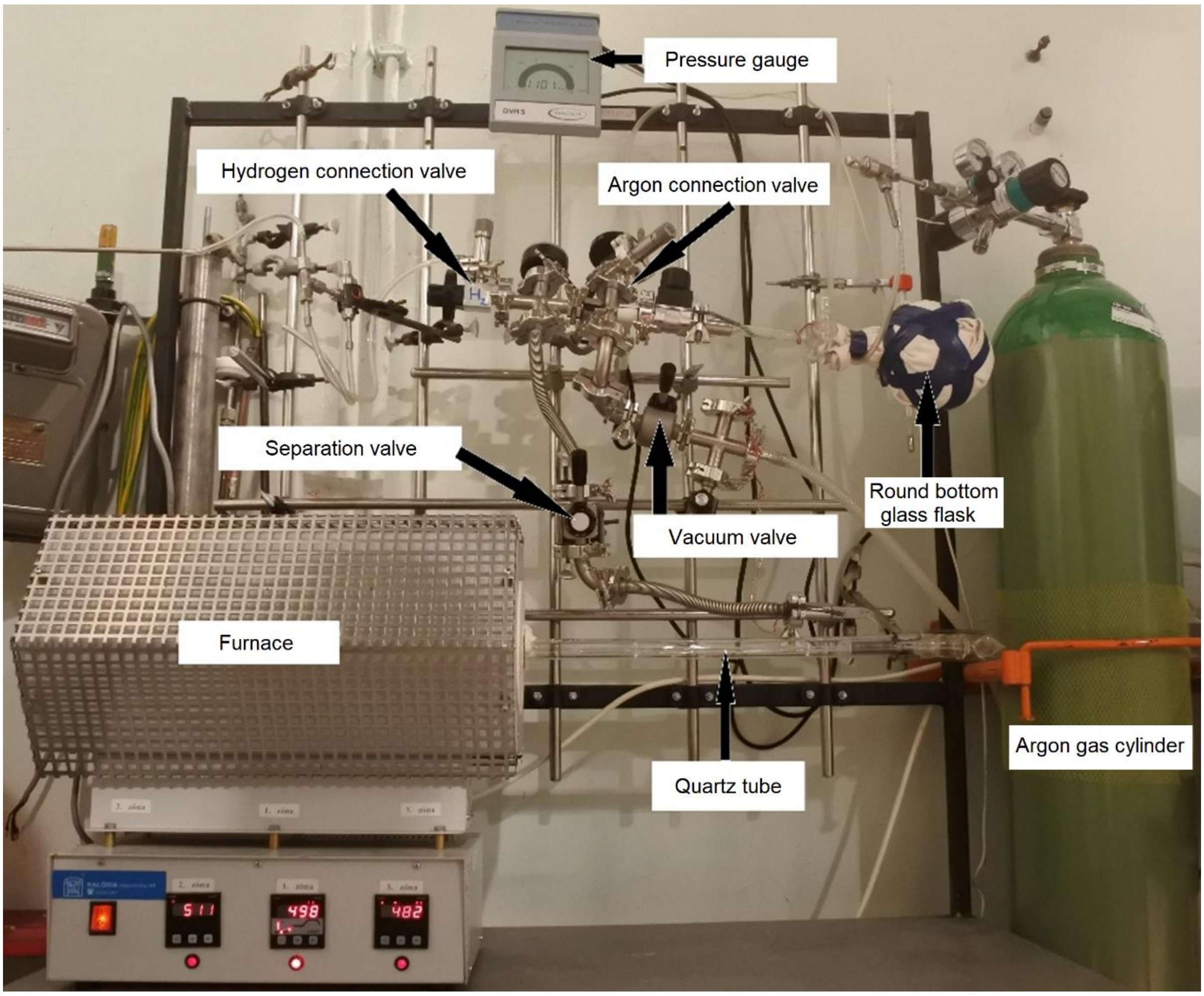

Fig. 1. The equipment used for the E110G and E110 sample hydrogenation

The experimental set-up consists mainly of an electrically heated three-zone tube furnace with a quartz tube put in it that connects to pipe-line system. The quartz tube contains the sample holder and can be evacuated or filled up with argon or hydrogen gas. The pressure of the gas system was measured by a Vacuubrand type DVR 5 pressure gauge and recorded by a computer.

We determined the exact volume of the round bottom glass flask that was used to calculate the V_2 volume (see Fig. 2). While V_2 volume has a role in calculating the amount of hydrogen (see in 2.2.1.4), the exact volume of V_1 is not necessary to be determined for the calculations.

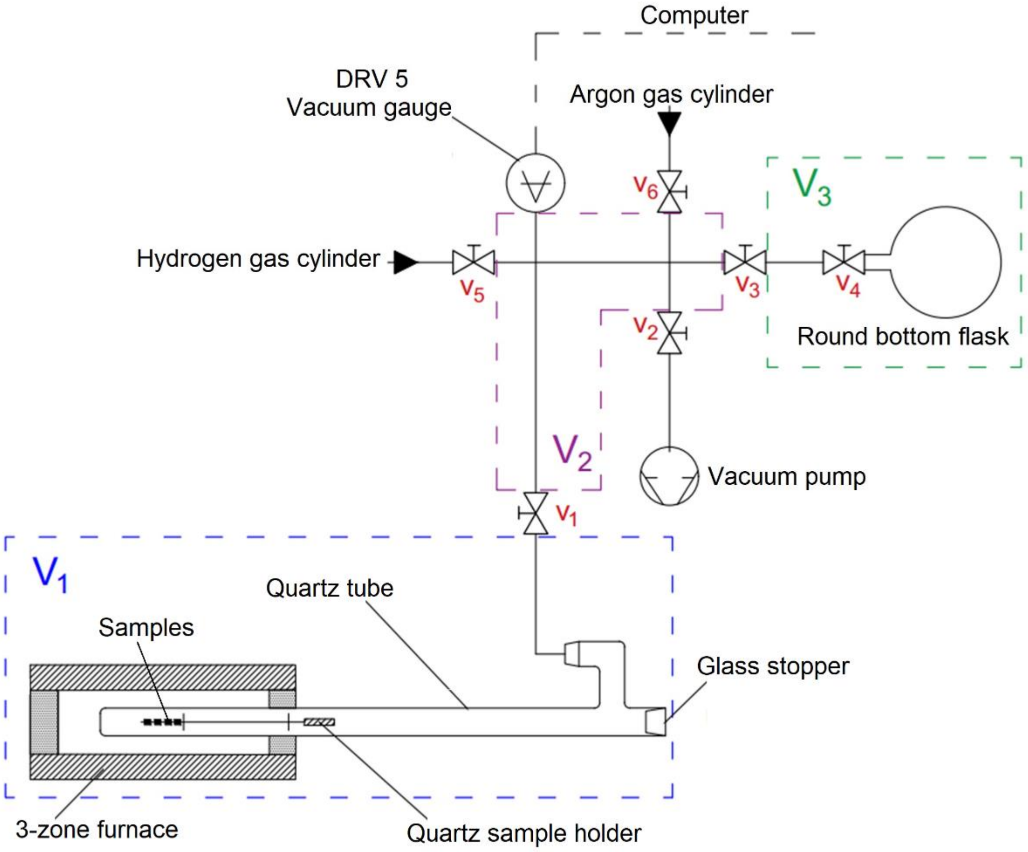

Fig. 2. The schematic view of the equipment for hydrogenation

2.2.1.2 *Tested materials, sample preparation*

The investigated cladding materials were E110G and Zircaloy-4. The E110G is a sponge base Zr-1%Nb alloy while Zircaloy-4 is a tin-bearing alloy with 1.4-1.6 wt% Sn content. Table 1 shows the chemical composition of these alloys.

Table 1. Chemical composition of the E110G and Zry4 alloys (average wt ppm), balance: Zr [6][7]

	Nb	Sn	Ni	Fe	Mg	Al	Si	Cr	Mn	Cu	Hf
E110G	10000	-	15	500	1,5	10	35	30	5	5	10
Zry4	-	13000	70	2100	-	-	-	1000	-	-	-

The E110G (outer diameter: 9.10 mm; wall thickness: 0.67 mm) and Zry-4 (outer diameter: 10.75 mm, wall thickness: 0.73 mm) fuel cladding tubes were cut into 8 mm long specimens. The specimens were open tube segments. Prior to the experiments the tube segments were degreased and cleaned by acetone in ultrasonic bath and weighed carefully.

2.2.1.3 Mass gain measurement

The samples were weighed both before and after the hydrogenation using a Mettler Toledo XP2U type ultra-microbalance having a readability of 0.1 μg.

2.2.1.4 H content measurement

After cleaning, 4 ring samples were placed on the quartz sample holder (see Fig. 3) that was put into the cold part of the quartz tube outside the furnace.

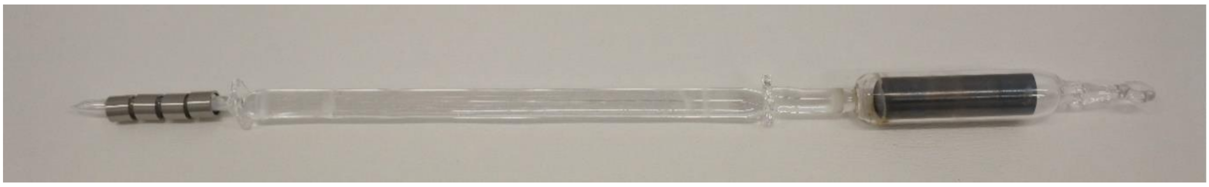

Fig. 3. The 8 mm long ring samples (on the left side) placed on the sample holder containing a soft iron core (on the right side)

The samples were always placed on the sample holder in ascending order by their names (e.g. from AHG-21 on the left side to AHG-24 on the right side), and consequently the samples with higher number in their names were placed closer to the outer part of the quartz tube (Fig. 4).

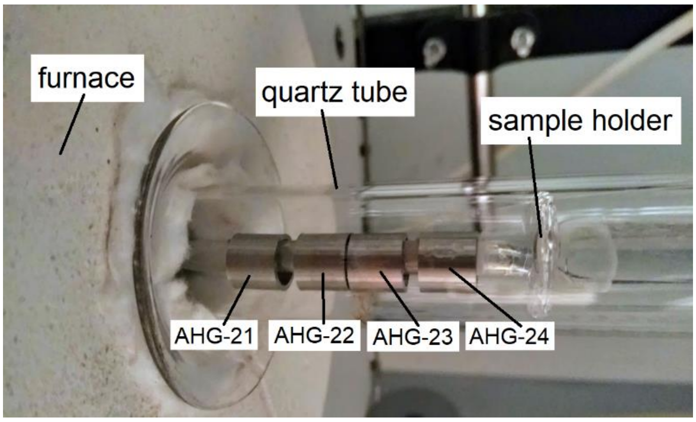

Fig. 4. Sample arrangement on the sample holder

At the cold end of the tube perforated plastic cylinders containing anhydrous calcium-sulphate were placed to adsorb the residual moisture after evacuating (see later). The tube was closed with a greased (Apiezon L type ultra-high vacuum grease) glass stopper.

To remove the air and moisture from the quartz tube, volumes V_1 and V_2 were evacuated and flushed using ultra high purity grade (99.999% (5N)) argon and hydrogen gases. In the end of this process the whole pipeline system was evacuated.

In the next step the volume V_2 was filled up to 1000 mbar with 5N pure hydrogen gas. Then the sample holder was pulled into the furnace using a magnet, so the samples got into the hot end of the quartz tube in the furnace, while the right part of the sample holder on Fig. 3 with the soft iron core remained out of the furnace. After 5 minutes the temperature of the samples reached the target temperature and valve v_1 was opened. The pressure in the (V_1+V_2) volume decreased to a value around 410 mbar. The pressure was continuously measured by the pressure gauge and recorded by a computer during the 23-hour long hydrogenation.

The decreasing of the pressure meant the samples were absorbing the hydrogen. The rate of the pressure decrease was getting lower and lower as an equilibrium was establishing between the hydrogen content of the samples and the gas.

After 23 hours the recording of the pressure was stopped, and the sample holder was fully pulled out from the furnace. After it cooled down to room temperature the system was filled up to around 1000 mbar with argon gas and opened, then the samples were carefully collected and weighed.

Based on the weight of the samples the approximate hydrogen content of the samples can be estimated using the formula:

$$c_{H_i} = \frac{\Delta m}{m_i} \cdot 10^6$$

where: c_{H_i} hydrogen content (however the effects of the possible oxidation are also included) (ppm)

Δm : mass gain of the sample during hydrogenation (grams)

m_i : mass of the sample before hydrogenation (grams)

The amount of the hydrogen absorbed by all the four samples can be calculated as follows. The total mass of the hydrogen in volume V_2 before the hydrogenation can be determined by the ideal gas law as we know the V_2 volume, the temperature and the pressure of the hydrogen gas in the volume V_2. The ratio of the absorbed gas to the total amount of it can be determined based on the pressure ratio of the hydrogen gas measured at the beginning and at the end of the experiment. Knowing the total mass of the 4 samples the average absorbed hydrogen concentration can be calculated (in ppm) since the absorption of the hydrogen is not even among the four samples in the furnace.

The quantitative analysis of the hydrogen absorbed in the samples was carried out using an ELTRA ELEMENTRAC OH-p 2 type elemental analyzer. This device uses the hot extraction method and can be used for quick measurement of oxygen and hydrogen concentrations in inorganic samples like steel, iron, copper, zirconium, titanium, molybdenum, nickel or ceramics. The highly sensitive NDIR and thermal conductivity detectors can reliably detect element concentrations from low ppm content to high percentages.

The device consists of two units, the analyzer that includes the high temperature furnace and a cooling unit. The hydrogen concentrations are determined by a robust and sensitive thermal conductivity cell. The sample falls through three airlocks into a graphite crucible, where it is melted by the high temperature generated by the flow of current through the graphite crucible. To decrease the melting point, the small pieces cut out from different positions of the ring samples and weighed before the measurement are placed in nickel capsules and put into the sample holder of the device. The carrier gas is high purity (99.999%) nitrogen that purges the hydrogen released from the sample to the thermal conductivity cell.

The thermal conductivity detector (TCD) detects the difference in thermal conductivity between effluent flow (carrier gas + hydrogen) and a reference flow of carrier gas alone; it produces a voltage proportional to this difference. During the measurement the TCD signal is continuously recorded, and the differences are finally integrated and converted into hydrogen content [8].

2.2.2 Results of H uptake tests

The rate and the characteristics of hydrogen uptake of the two alloys were determined at 300 °C, 330 °C, 370 °C, and 400 °C; using 4 ring samples at every temperature (Table 2). The effect of the temperature on the hydrogen uptake of the two zirconium alloys was also investigated in the range of 300-400 °C.

Table 2. Test matrix of the hydrogen uptake test series

Temperature (°C)	Sample	
	E110G	Zircaloy-4
300	AHG-29	ZryH-13
	AHG-30	ZryH-14
	AHG-31	ZryH-15
	AHG-32	ZryH-16
330	AHG-21	ZryH-9
	AHG-22	ZryH-10
	AHG-23	ZryH-11
	AHG-24	ZryH-12
370	AHG-25	ZryH-1
	AHG-26	ZryH-2
	AHG-27	ZryH-3
	AHG-28	ZryH-4
400	AHE-12	ZryH-5
	AHE-13	ZryH-6
	AHE-14	ZryH-7
	AHE-15	ZryH-8

The pressure of the hydrogen was measured and recorded during the experiment. The recording of the pressure was started when the pressure dropped from 1000 mbar to around 400-410 mbar after opening valve v_1 (see Fig. 2). The mass gain of the ring samples was determined by weighing the samples before and after the hydrogenation. The absorbed hydrogen content of a few samples was quantitatively determined by an elemental analyzer device.

2.2.2.1 Execution of tests

Notwithstanding the presence of the calcium-sulphate getter placed at the joint of the quartz tube, some water vapor (and oxygen) could enter the system during the measurements, and thus slight oxidation of the samples occurred resulting thin oxide layer on the surface of some samples.

Depending on the circumstances (mainly on the temperature and the alloy type) once an oxide layer was formed, it was either dark gray or colourful (if very thin).

After the measurement of the samples AHE-12_15 (carried out at 400 °C) an even dark grey oxide layer could be seen on the samples (see Fig. 5).

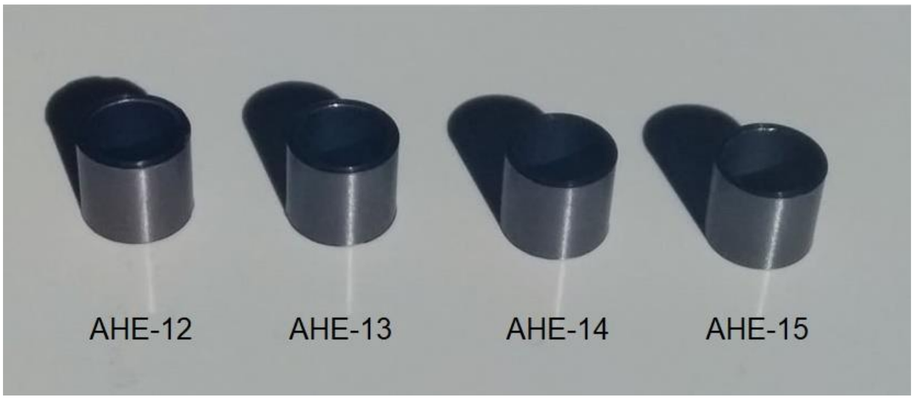

Fig. 5. The gray oxide layer on the samples caused by the undesired oxidation during the hydrogenation

At lower temperatures thinner oxide layers occurred on some samples. It can be seen in Fig. 6 that the sample AHG-24 (placed nearest to the outer part of the quartz tube) has a blue oxide layer while the color of the oxide layer on the sample next to it (AHG-23) varies from purple to yellow depending on the rate of the oxidation.

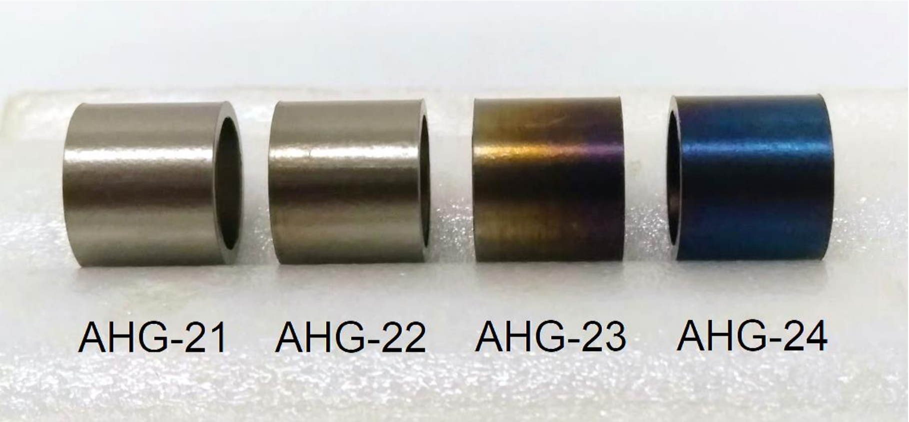

Fig. 6. The colored oxide layer on the outer samples (on the right side) hydrogenated at 330 °C

The oxygen and water vapour diffused from the outer part of the system did react with the sample AHG-24 first, and thus, this sample has the thickest oxide layer on it. The color and the thickness of the oxide layer indicate how much oxygen and water have been consumed by the reactions with the samples. The inner two rings (AHG-21 and AHG-22) did not suffer visible oxidation, and thus, they remained shiny.

2.2.2.2 *Hydrogen uptake results*

The hydrogen uptake of the samples was determined by measuring the hydrogen pressure. Fig. 7 shows the hydrogen pressure as a function of time of hydrogenation in the case of the E110G samples at different temperatures. It can clearly be seen that the higher the temperature the higher the ratio of the absorbed hydrogen is.

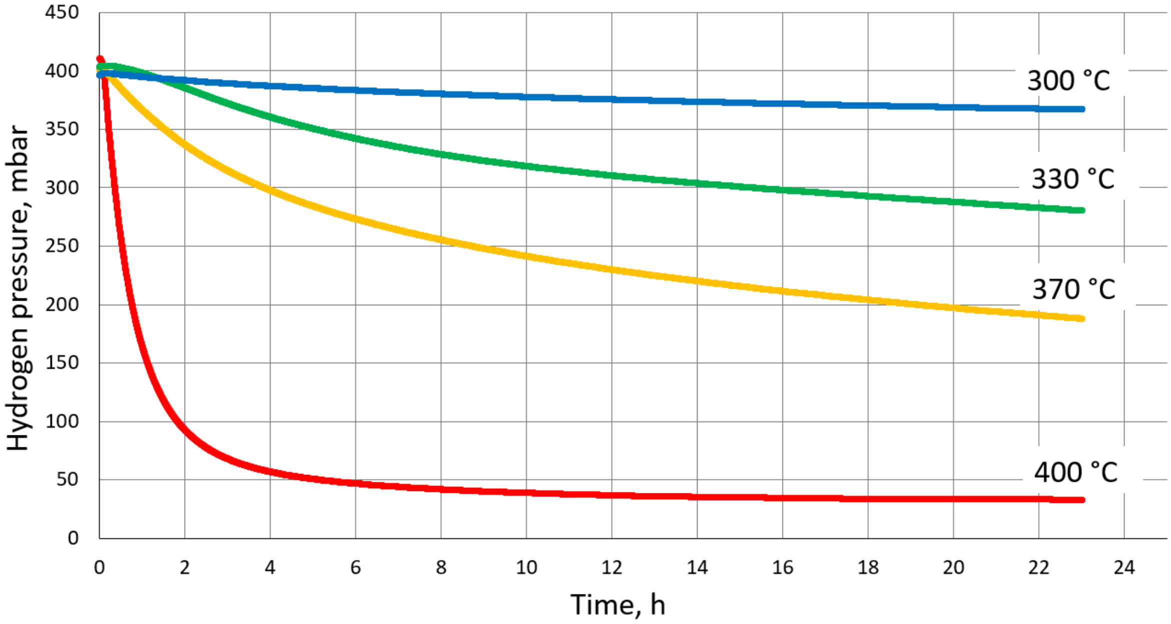

Fig. 7. The hydrogen pressure during the experiments with E110G samples at different temperatures

We can see that only around 8% of the hydrogen has been absorbed by the E110G samples at 300 °C after 23 hours while this ratio is 92% at 400 °C. These ratios are 51% and 94% for the Zircaloy-4 alloy samples, respectively (see Fig. 8).

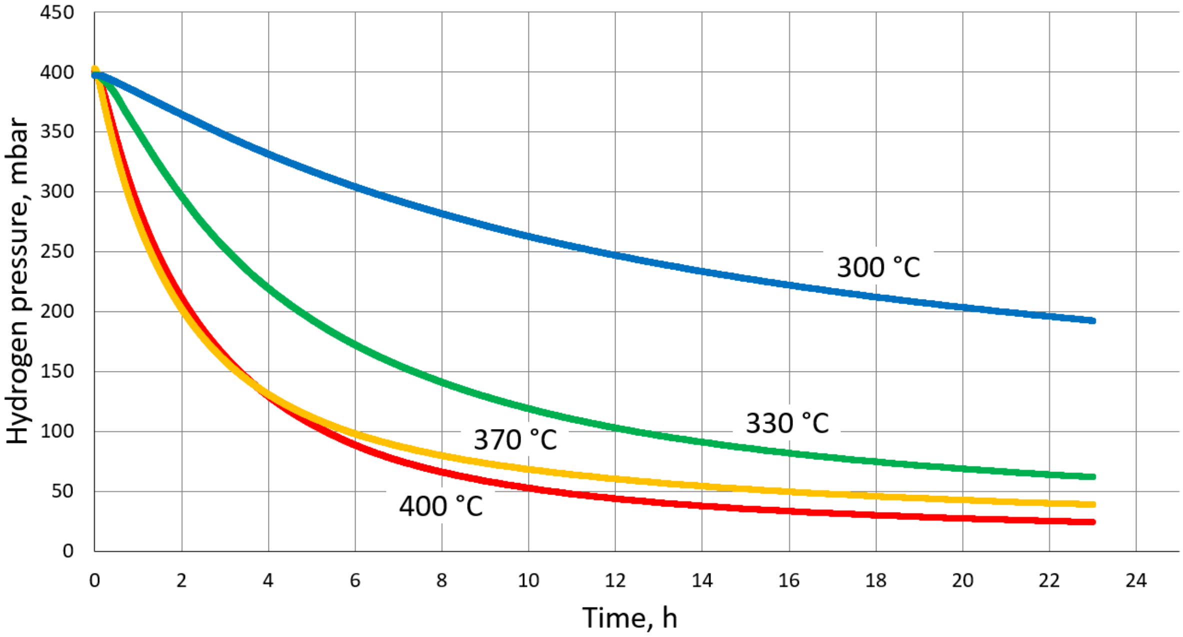

Fig. 8. The hydrogen pressure during the experiments with Zircaloy-4 samples at different temperatures

It can be concluded that the ring samples made of E110G alloy do absorb only a small part of the total hydrogen at 300 °C and this ratio is increasing around evenly at higher temperature values. We found this ratio to be ca. 90% after 8 hours at 400 °C and not to increase much thereafter (see on Fig. 7). In the case of the Zircaloy-4 samples the ratio of the absorbed hydrogen was more than 50% at 300 °C, and this ratio exceeded 80% already at 330 °C (unlike the case of E110G) as well as it didn't increase much at higher temperatures (Fig. 8).

Comparing the two alloys' hydrogen uptake at different temperatures we can see that at 300 °C, 330 °C and 370 °C the E110G samples showed lower tendency to absorb hydrogen (Fig. 9), however at 400 °C the pressure decrease was faster in the experiment with the E110G alloy.

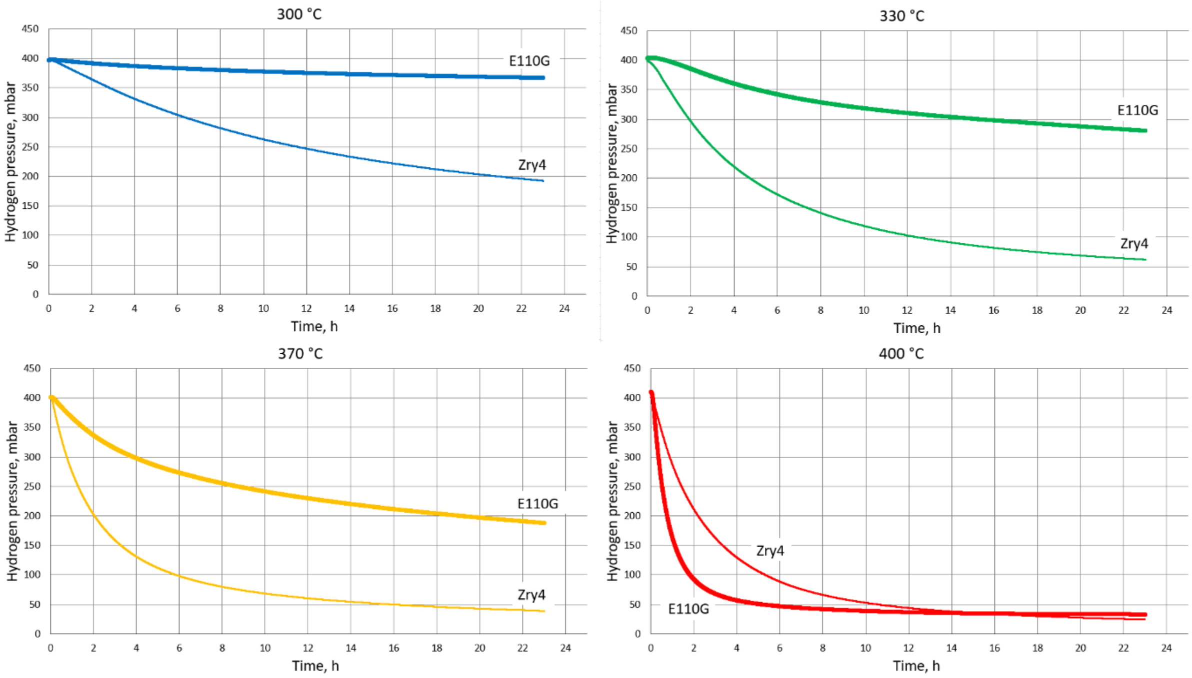

Fig. 9. The difference in the characteristics of the hydrogen uptake between the two alloys at different temperatures

The E110G samples absorbed the 90% of the hydrogen gas already after 8 hours while the Zry-4 samples did the same only after 13 hours however the Zry-4 samples absorbed more hydrogen during the 23-hour long experiment than the samples made of E110G alloy.

2.2.2.3 Mass gain results

The ring samples were weighed (see 2.2.1.3) and mass gain values were calculated. The mass gain was caused both by the absorbed hydrogen and by the slight oxidation of the samples. The results are summarized in Table 3 and Table 4 for E110G and for Zircaloy-4 samples, respectively.

Table 3. The mass gain results for the E110G samples

300 °C		330 °C		370 °C		400 °C	
Sample	Mass gain (ppm)	Sample	Mass gain (ppm)	Sample	Mass gain (ppm)	Sample	Mass gain (ppm)
AHG-29	251.0	AHG-21	1217.6	AHG-25	2017.3	AHE-12	3873.1
AHG-30	210.4	AHG-22	866.8	AHG-26	1525.0	AHE-13	3624.3
AHG-31	205.8	AHG-23	388.7	AHG-27	1111.9	AHE-14	2261.2
AHG-32	203.4	AHG-24	390.4	AHG-28	825.3	AHE-15	1096.7

Table 4. The mass gain results for the Zircaloy-4 samples

300 °C		330 °C		370 °C		400 °C	
Sample	Mass gain (ppm)	Sample	Mass gain (ppm)	Sample	Mass gain (ppm)	Sample	Mass gain (ppm)
ZryH-13	1333.4	ZryH-9	2309.5	ZryH-1	2211.9	ZryH-5	2464.2
ZryH-14	1473.8	ZryH-10	2169.0	ZryH-2	2163.4	ZryH-6	1951.7
ZryH-15	1047.0	ZryH-11	1576.1	ZryH-3	1940.6	ZryH-7	1957.8
ZryH-16	934.0	ZryH-12	1130.5	ZryH-4	1424.4	ZryH-8	1787.3

Samples having the highest number in their names (at a given temperature) were placed on the sample holder closer to the outer part of the quartz tube (from where the undesirable water vapor or oxygen could enter the quartz tube).

An oxide layer on the surface of a sample reduces the hydrogen absorption rate, and thus, the amount of the hydrogen that can be absorbed. Usually thicker oxide layers were formed on the samples which were placed nearer to the outer part of the quartz tube (see in 2.2.2.1), and thus, the inner samples could absorb more hydrogen which can be seen in the mass gain results of the E110G samples (Fig. 10).

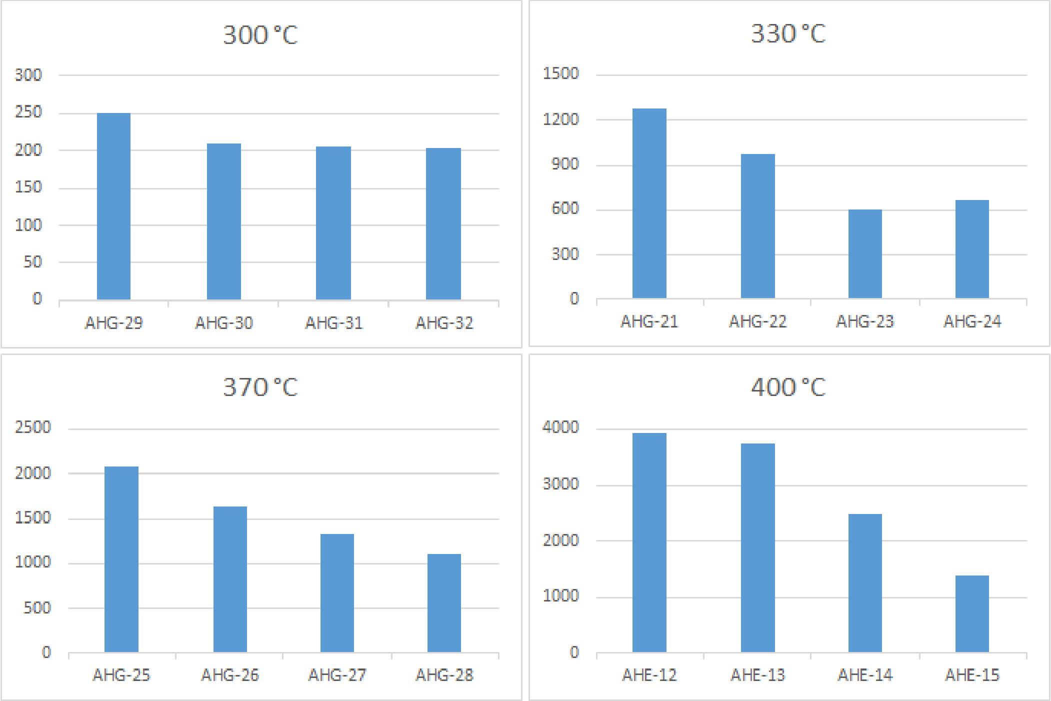

Fig. 10. The calculated mass gain results for the E110G samples

The differences in mass gain were found not to be so big for the Zircaloy-4 samples even at higher temperatures (Fig. 11).

For every temperature an average mass gain was calculated for the four samples that is useful when comparing it to the calculated approximate average amount of absorbed hydrogen (see 2.2.2.4).

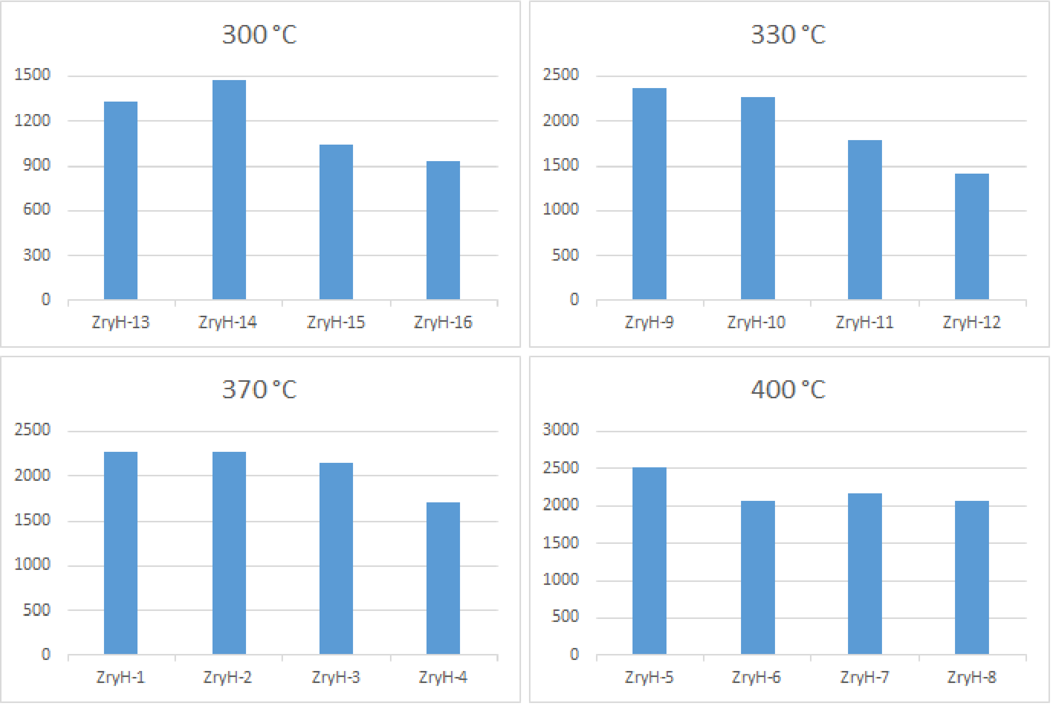

Fig. 11. The calculated mass gain results for the Zircaloy-4 samples

2.2.2.4 H content results

Approximate calculations were made to estimate the total amount of hydrogen absorbed by the four samples placed at once in the furnace. These calculations were made based on the total pressure decreasing during the measurement (see more detailed description in 2.2.1.4).

The results of the average hydrogen contents together with the average mass gain results are summarized in Table 5. for comparison.

Table 5. Comparison of the mass gain and the calculated average hydrogen content results

Temp. (°C)		E110G	difference (ppm)	difference (%)	Zircaloy-4	difference (ppm)	difference (%)
300	H content (ppm)	221.0	3.3	1.49	1203.0	5.9	0.49
	mass gain (ppm)	217.7			1197.1		
330	H content (ppm)	907.0	25.6	2.82	1980.0	18.2	0.92
	mass gain (ppm)	881.4			1961.8		
370	H content (ppm)	1556.0	20.6	1.32	2129.0	28.4	1.33
	mass gain (ppm)	1535.4			2100.6		
400	H content (ppm)	2746.0	133.3	4.85	2188.0	17.8	0.81
	mass gain (ppm)	2879.3			2205.8		

It can be seen that the differences between the calculated average hydrogen content and the mass gain results are under 5% in every case. A more visual comparison can be seen in Fig. 12.

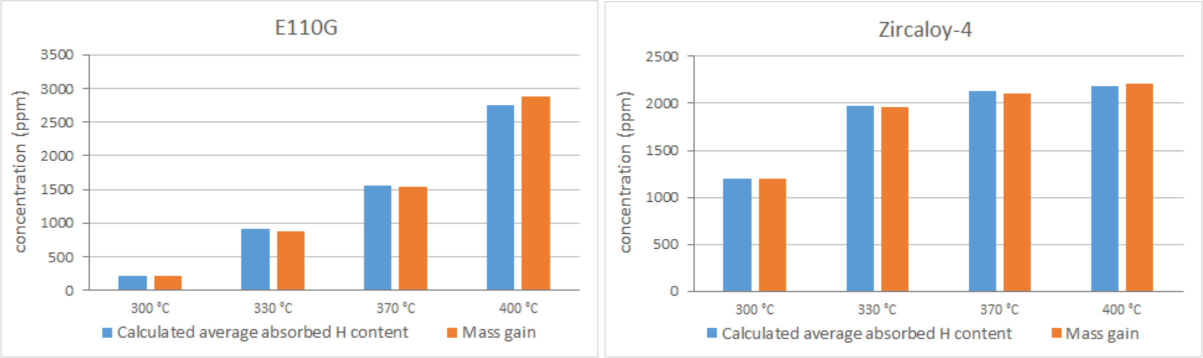

Fig. 12. The calculated average absorbed hydrogen content and the mass gain results

The differences are caused mainly by the slight oxidation of the samples. The absorbed hydrogen content was calculated based on the pressure decreasing which can also be caused by a slight leakage of the hydrogen from the system during the measurement. It should be noted that it can result overestimations in hydrogen contents.

Two E110G and two Zircaloy-4 samples were chosen for quantitative hydrogen content determination carried out by an elemental analyzer device ELTRA. All of these four samples were hydrogenated at 330 °C, and thin oxide layers were formed on some of them (Fig. 6). The results together with the mass gain of those samples are summarized in Table 6 and Fig. 13.

Table 6. Comparison of the mass gain and the quantitative hydrogen content results

	AHG-21	AHG-24	ZryH-9	ZryH-12
mass gain (ppm)	1279	669	2371	1410
H content by ELTRA (ppm)	1310	616	2586	1447

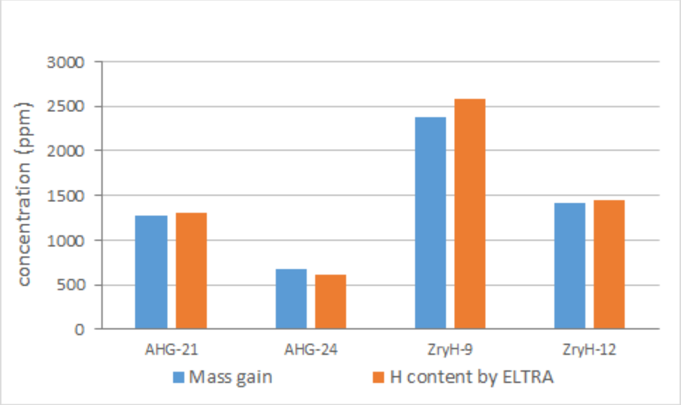

Fig. 13. The mass gain and the results of the quantitative hydrogen content determination

No significant differences can be seen in the results. In the case of the sample AHG-24 the surplus in the mass gain can be explained by the oxide layer, which was also taken into account at the weighing, but three out of the four comparisons show higher hydrogen content than mass gain. It can be explained as follows.

The samples were cut into small (0.03-0.1 gram) pieces for the measurement as hot extraction process required only a very small number of samples. When trying to cut the ring samples they much more easily break at the points where the alloy became more brittle caused by the higher hydrogen content, and therefore some pieces contain averagely more hydrogen than the average for the whole ring sample. In some cases, with such non-representative pieces selected randomly to be measured, a higher hydrogen content was resulted than the mass gain, however the whole ring sample may contain less hydrogen.

2.2.3 Content of the database

In this chapter we summarize the files that have been generated and created relating to the hydrogen uptake tests and calculations.

Data files were generated during each hydrogenation measurement. These .dat files contain the date, the time and the relating pressure values measured in the volume ((V_1+V_2), see Fig. 2). The files were named after the samples' names and the temperature of the measurement (e.g. "AHG-12_15_400.dat").

Excel files were created for both the two investigated alloys and for each temperature separately, named the same way as the .dat files.

The content of the Excel-files is as follows:

- the pressure values (with the relating date and time) imported from the .dat files mentioned above,
- the weight of the sample before the hydrogenation in grams for every weigh,
- the weight of the sample before the hydrogenation in grams for every weigh,
- the calculated mass gain in grams and in ppm,
- the volume V_2 (see Fig. 2),
- the pressure in V_2 before opening valve v_1 in mbars (see Fig. 2),
- the pressure in V_1 after opening valve v_1 and before the hydrogen uptake tests in mbars (see Fig. 2),
- the pressure in V_1 at the end of the hydrogen uptake tests in mbars (see Fig. 2),
- the temperature in the volume V_2 before opening valve v_1 in °C (see Fig. 2),
- the calculated average amount of the absorbed hydrogen in ppm,
- the hydrogen content in ppm, determined by the ELTRA elemental analyzer device (for the samples mentioned in Table 6.

Some photos on samples were also made. They are collected in .jpg format.

Table 7. The files in the database

File		Content of the file
Name:	**AHE-12_15_400.dat**	- **hydrogen pressure** values in mbar during the measurement with a resolution of 0.5 sec, - **date** (yyyy. mm. dd.) **and time** (hh:mm:ss) related to the pressure values
Description:	the raw data file of the measurement of the samples AHE-12, AHE-13, AHE-14, and AHE-15; carried out at 400 °C	
Name:	**AHG-21_24_330.dat**	- **hydrogen pressure** values in mbar during the measurement with a resolution of 0.5 sec, - **date** (yyyy. mm. dd.) **and time** (hh:mm:ss) related to the pressure values
Description:	the raw data file of the measurement of the samples AHG-21, AHG-22, AHG-23, and AHG-24; carried out at 330 °C	
Name:	**AHG-25_28_370.dat**	- **hydrogen pressure** values in mbar during the measurement with a resolution of 0.5 sec, - **date** (yyyy. mm. dd.) **and time** (hh:mm:ss) related to the pressure values
Description:	the raw data file of the measurement of the samples AHG-25, AHG-26, AHG-27, and AHG-28; carried out at 370 °C	

Name: **AHG-29_32_300.dat** Description: the raw data file of the measurement of the samples AHG-29, AHG-30, AHG-31, and AHG-32; carried out at 300 °C	- **hydrogen pressure** values in mbar during the measurement with a resolution of 0.5 sec, - **date** (yyyy. mm. dd.) **and time** (hh:mm:ss) related to the pressure values
Name: **AHE-12_15_400.xlsm** Description: the Excel file relating to the measurement of the samples AHE-12, AHE-13, AHE-14, and AHE-15; carried out at 400 °C	- **hydrogen pressure** values in mbar during the measurement with a resolution of 1 sec, - **date** (yyyy. mm. dd.) **and time** (hh:mm:ss) related to the pressure values, - **name of the samples** in the measurement, - measured **mass of the samples** (with an accuracy of 0.1 μg) before and after the hydrogen uptake test (3-3 weighs for each sample) and the calculated average values, - the calculated **mass gain** for each of the samples both in grams and in ppm, - physical, chemical and measurement-related **constants** (e.g. gas constant, molar mass of hydrogen and zirconium, V_2 volume (see Fig. 2), - the **pressure in the system** before and after opening valve v_1 (see Fig. 2) and at the end of the test in mbar, - the **temperature in V_2** (see Fig. 2) in °C, - the calculated **average absorbed hydrogen** per sample in ppm, - a **mass gain diagram**, - a **hydrogen pressure history diagram**.
Name: **AHG-21_24_330.xlsm** Description: the Excel file relating to the measurement of the samples AHG-21, AHG-22, AHG-23, and AHG-24; carried out at 330 °C	- **hydrogen pressure** values in mbar during the measurement with a resolution of 1 sec, - **date** (yyyy. mm. dd.) **and time** (hh:mm:ss) related to the pressure values, - **name of the samples** in the measurement, - measured **mass of the samples** (with an accuracy of 0.1 μg) before and after the hydrogen uptake test (3-3 weighs for each sample) and the calculated average values, - the calculated **mass gain** for each of the samples both in grams and in ppm, - physical, chemical and measurement-related **constants** (e.g. gas constant, molar mass of hydrogen and zirconium, V_2 volume (see Fig. 2), - the **pressure in the system** before and after opening valve v_1 (see Fig. 2) and at the end of the test in mbar, - the **temperature in V_2** (see Fig. 2) in °C, - the calculated **average absorbed hydrogen** per sample in ppm,

	- **hydrogen content** in ppm for samples AHG-21 and AHG-24 determined by the elemental analyzer device ELTRA (see 2.2.1.4) - a **mass gain diagram**, - a **hydrogen pressure history diagram**.
Name: **AHG-25_28_370.xlsm** Description: the Excel file relating to the measurement of the samples AHG-25, AHG-26, AHG-27, and AHG-28; carried out at 370 °C	- **hydrogen pressure** values in mbar during the measurement with a resolution of 1 sec, - **date** (yyyy. mm. dd.) **and time** (hh:mm:ss) related to the pressure values, - **name of the samples** in the measurement, - measured **mass of the samples** (with an accuracy of 0.1 μg) before and after the hydrogen uptake test (3-3 weighs for each sample) and the calculated average values, - the calculated **mass gain** for each of the samples both in grams and in ppm, - physical, chemical and measurement-related **constants** (e.g. gas constant, molar mass of hydrogen and zirconium, V_2 volume (see Fig. 2), - the **pressure in the system** before and after opening valve v_1 (see Fig. 2) and at the end of the test in mbar, - the **temperature in V_2** (see Fig. 2) in °C, - the calculated **average absorbed hydrogen** per sample in ppm, - a **mass gain diagram**, - a **hydrogen pressure history diagram**.
Name: **AHG-29_32_300.xlsm** Description: the Excel file relating to the measurement of the samples AHG-29, AHG-30, AHG-31, and AHG-32; carried out at 300 °C	- **hydrogen pressure** values in mbar during the measurement with a resolution of 1 sec, - **date** (yyyy. mm. dd.) **and time** (hh:mm:ss) related to the pressure values, - **name of the samples** in the measurement, - measured **mass of the samples** (with an accuracy of 0.1 μg) before and after the hydrogen uptake test (3-3 weighs for each sample) and the calculated average values, - the calculated **mass gain** for each of the samples both in grams and in ppm, - physical, chemical and measurement-related **constants** (e.g. gas constant, molar mass of hydrogen and zirconium, V_2 volume (see Fig. 2), - the **pressure in the system** before and after opening valve v_1 (see Fig. 2) and at the end of the test in mbar, - the **temperature in V_2** (see Fig. 2) in °C, - the calculated **average absorbed hydrogen** per sample in ppm, - a **mass gain diagram**, - a **hydrogen pressure history diagram** of the test.

Name: **Zry4H-1_4_370.dat** Description: the raw data file of the measurement of the samples Zry4H-1, Zry4H-2, Zry4H-3 and Zry4H-4; carried out at 370 °C	- **hydrogen pressure** values in mbar during the measurement with a resolution of 0.5 sec, - **date** (yyyy. mm. dd.) **and time** (hh:mm:ss) related to the pressure values
Name: **Zry4H-5_8_400.dat** Description: the raw data file of the measurement of the samples Zry4H-5, Zry4H-6, Zry4H-7 and Zry4H-8; carried out at 400 °C	- **hydrogen pressure** values in mbar during the measurement with a resolution of 0.5 sec, - **date** (yyyy. mm. dd.) **and time** (hh:mm:ss) related to the pressure values
Name: **Zry4H-9_12_330.dat** Description: the raw data file of the measurement of the samples Zry4H-9, Zry4H-10, Zry4H-11 and Zry4H-12; carried out at 330 °C	- **hydrogen pressure** values in mbar during the measurement with a resolution of 0.5 sec, - **date** (yyyy. mm. dd.) **and time** (hh:mm:ss) related to the pressure values
Name: **Zry4H-13_16_300.dat** Description: the raw data file of the measurement of the samples Zry4H-13, Zry4H-14, Zry4H-15 and Zry4H-16; carried out at 300 °C	- **hydrogen pressure** values in mbar during the measurement with a resolution of 0.5 sec, - **date** (yyyy. mm. dd.) **and time** (hh:mm:ss) related to the pressure values
Name: **Zry4H-1_4_370.xlsm** Description: the Excel file relating to the measurement of the samples Zry4H-1, Zry4H-2, Zry4H-3 and Zry4H-4; carried out at 370 °C	- **hydrogen pressure** values in mbar during the measurement with a resolution of 1 sec, - **date** (yyyy. mm. dd.) **and time** (hh:mm:ss) related to the pressure values, - **name of the samples** in the measurement, - measured **mass of the samples** (with an accuracy of 0.1 μg) before and after the hydrogen uptake test (3-3 weighs for each sample) and the calculated average values, - the calculated **mass gain** for each of the samples both in grams and in ppm, - physical, chemical and measurement-related **constants** (e.g. gas constant, molar mass of hydrogen and zirconium, V_2 volume (see Fig. 2), - the **pressure in the system** before and after opening valve v_1 (see Fig. 2) and at the end of the test in mbar, - the **temperature in V_2** (see Fig. 2) in °C, - the calculated **average absorbed hydrogen** per sample in ppm, - a **mass gain diagram**, - a **hydrogen pressure history diagram**.

Name: **Zry4H-5_8_400.xlsm** Description: the Excel file relating to the measurement of the samples Zry4H-5, Zry4H-6, Zry4H-7 and Zry4H-8; carried out at 400 °C	- **hydrogen pressure** values in mbar during the measurement with a resolution of 1 sec, - **date** (yyyy. mm. dd.) **and time** (hh:mm:ss) related to the pressure values, - **name of the samples** in the measurement, - measured **mass of the samples** (with an accuracy of 0.1 μg) before and after the hydrogen uptake test (3-3 weighs for each sample) and the calculated average values, - the calculated **mass gain** for each of the samples both in grams and in ppm, - physical, chemical and measurement-related **constants** (e.g. gas constant, molar mass of hydrogen and zirconium, V_2 volume (see Fig. 2), - the **pressure in the system** before and after opening valve v_1 (see Fig. 2) and at the end of the test in mbar, - the **temperature in V_2** (see Fig. 2) in °C, - the calculated **average absorbed hydrogen** per sample in ppm, - a **mass gain diagram**, - a **hydrogen pressure history diagram**.
Name: **Zry4H-9_12_330.xlsm** Description: the Excel file relating to the measurement of the samples Zry4H-9, Zry4H-10, Zry4H-11 and Zry4H-12; carried out at 330 °C	- **hydrogen pressure** values in mbar during the measurement with a resolution of 1 sec, - **date** (yyyy. mm. dd.) **and time** (hh:mm:ss) related to the pressure values, - **name of the samples** in the measurement, - measured **mass of the samples** (with an accuracy of 0.1 μg) before and after the hydrogen uptake test (3-3 weighs for each sample) and the calculated average values, - the calculated **mass gain** for each of the samples both in grams and in ppm, - physical, chemical and measurement-related **constants** (e.g. gas constant, molar mass of hydrogen and zirconium, V_2 volume (see Fig. 2), - the **pressure in the system** before and after opening valve v_1 (see Fig. 2) and at the end of the test in mbar, - the **temperature in V_2** (see Fig. 2) in °C, - the calculated **average absorbed hydrogen** per sample in ppm, - **hydrogen content** in ppm for samples Zry4H-9 and Zry4H-12 determined by the elemental analyzer device ELTRA (see 2.2.1.4), - a **mass gain diagram**, - a **hydrogen pressure history diagram**.

Name: **Zry4H-13_16_300.xlsm** Description: the Excel file relating to the measurement of the samples Zry4H-13, Zry4H-14, Zry4H-15 and Zry4H-16; carried out at 300 °C	- **hydrogen pressure** values in mbar during the measurement with a resolution of 1 sec, - **date** (yyyy. mm. dd.) **and time** (hh:mm:ss) related to the pressure values, - **name of the samples** in the measurement, - measured **mass of the samples** (with an accuracy of 0.1 μg) before and after the hydrogen uptake test (3-3 weighs for each sample) and the calculated average values, - the calculated **mass gain** for each of the samples both in grams and in ppm, - physical, chemical and measurement-related **constants** (e.g. gas constant, molar mass of hydrogen and zirconium, V_2 volume (see Fig. 2), - the **pressure in the system** before and after opening valve v_1 (see Fig. 2) and at the end of the test in mbar, - the **temperature in V_2** (see Fig. 2) in °C, - the calculated **average absorbed hydrogen** per sample in ppm, - a **mass gain diagram**, - a **hydrogen pressure history diagram**.

2.3 Hydrogen uptake simulation at reactor operational temperatures

2.3.1 Creating and developing the model

We wanted to create a basic numerical model based on the hydrogen uptake experimental results [9] to calculate the hydrogen uptake rate of E110 alloy tube segments with the main aims:

- The model should *cover* the temperature range of 300-400 °C and the pressure range of 0-400 mbar.
- The model should use a *simple* formula.
- The correlation should calculate the hydrogen uptake rate based *both* on the actual temperature *and* the partial pressure of the hydrogen gas.

In the first step, using the partial pressure history (see Fig. 14) we calculated the hydrogen content in the E110 ring samples for each time step.

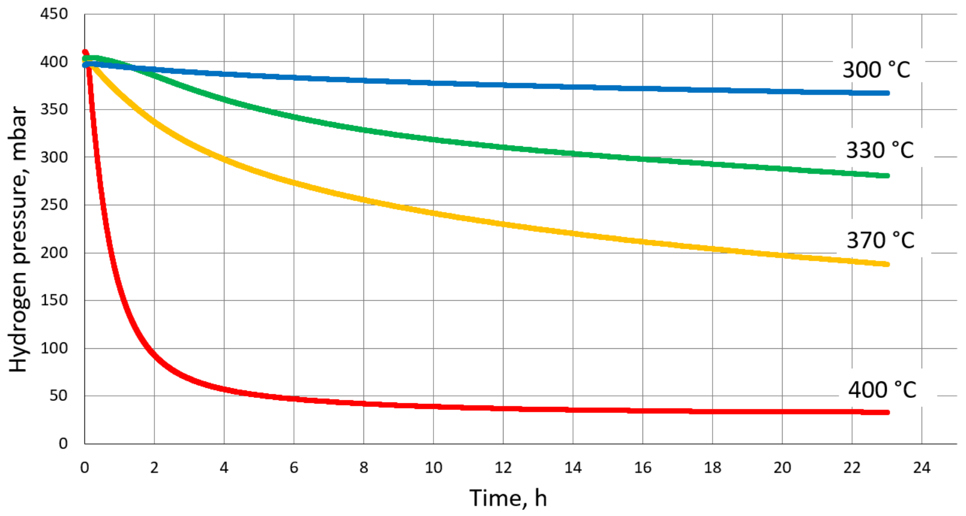

Fig. 14. The partial pressure history of the E110 experiments

After the calculations we determined four correlations for the four temperatures of the experiments between the amount of the absorbed hydrogen per unit time and the partial pressure of the hydrogen gas (Fig. 15).

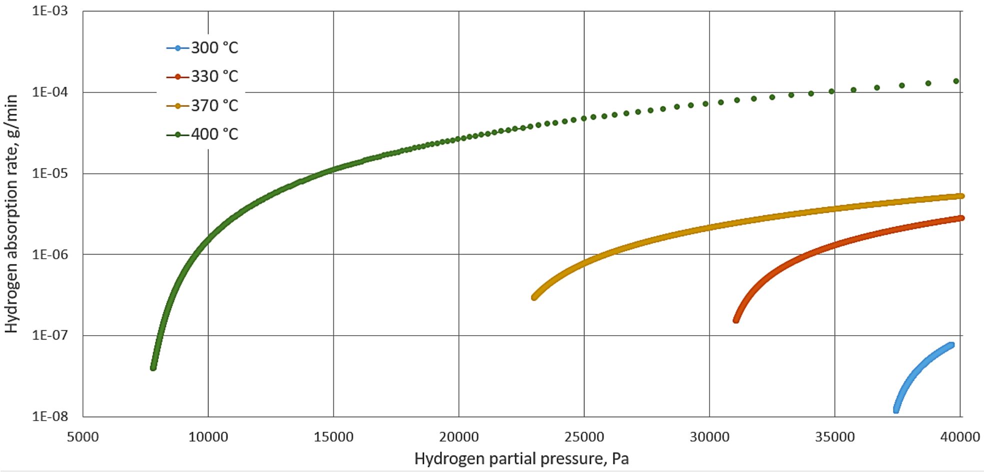

Fig. 15. The hydrogen absorption rate as a function of the hydrogen partial pressure at different temperatures

Based on these results we made verifying calculations using the correlation and the initial parameters and the conditions of the experiments as an input data set. We determined the partial pressure for each time step to be able to compare the real and the model-resulted pressure history. The differences were not larger than 5% but we had 4 different only-pressure-dependent correlations which were only applicable on one constant temperature.

One of our main aims was to invent the temperature dependence, and thus we extended the formula by introducing a temperature-dependent part which was found to be exponential.

We refined the pressure coefficient and the temperature coefficient to reduce the difference in the pressure history between the results given by the formula and the experimental data.

The formula we finally created can be written as follows:

$$dw = A \cdot p_H(t) \cdot e^{B \cdot T}$$

where*:*

dw	hydrogen uptake rate $(g \cdot min^{-1})$
A	pressure constant, $7.5 \cdot 10^{-14}\ mbar^{-1}$
$p_H(t)$	actual partial pressure of hydrogen $(mbar)$
B	temperature constant, $0.0345\ °C^{-1}$
T	temperature $(°C)$

This simple formula with the above-mentioned values for the constants A and B can give the decentest results when we want to cover the temperature range from 300 to 400 °C.

After determining the hydrogen uptake rate, the model calculates the *amount of the absorbed hydrogen* for the actual time step, then the *partial pressure of the hydrogen gas* is determined and will be the input for the next time step. The model can compute the *hydrogen content of the samples* as well.

The input parameters the model needs to do the above-mentioned calculations are as follows:

- the temperature of the zirconium samples,
- the initial partial pressure of the hydrogen gas in the gas volume,
- the (average) temperature of the gas,
- the volume of the gas(es),
- the mass of the zirconium samples,
- the length of the measurement.

Four sets of calculations have been done covering the temperature range of 300-400 °C, and the results have been compared to the data originating from the measurements.

2.3.2 Results

After running a calculation with a set of the input parameters (including the above-mentioned constants), a plot has been generated making it easier to compare the results to the experimental data. After refining a coefficient, the plot gave us information about how the accuracy of the model changed. In each case we compared the calculated hydrogen partial pressure in the system during the simulation to the measured pressure values for the proper time of the experiment. Since we wanted to keep the formula simple, its accuracy could not be increased above a certain level in some cases, however the formula with the coefficients mentioned above resulted in the least difference taking into account all the temperature values the comparison could be done at.

It can be seen that at 300 °C (Fig. 16) and at 330 °C (Fig. 17) the model resulted almost a linear pressure history, however the differences were not large at all.

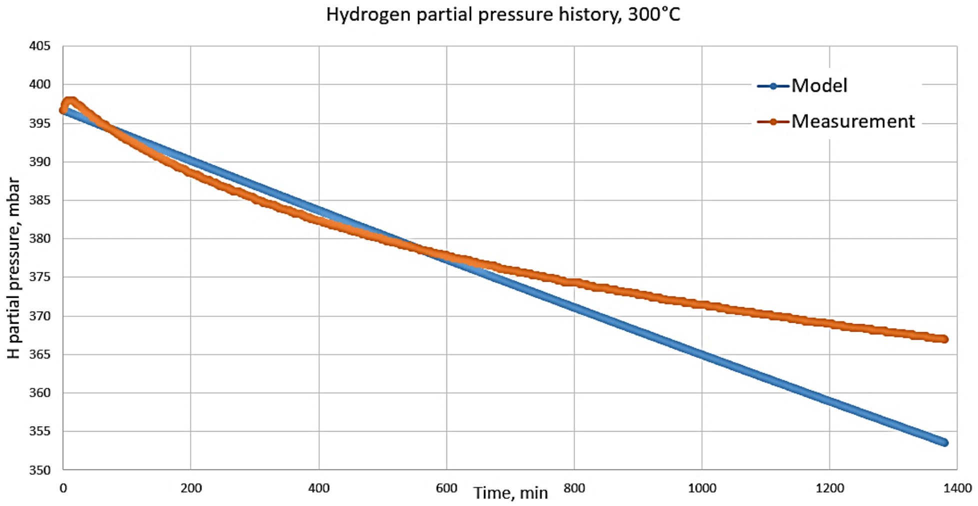

Fig. 16. Comparison of the calculated pressure history and the experimental data at 300 °C

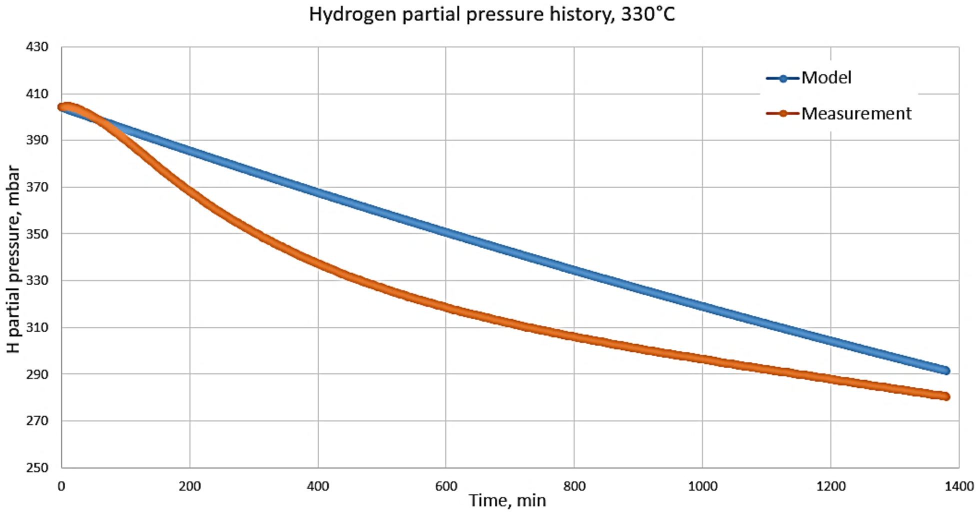

Fig. 17. Comparison of the calculated pressure history and the experimental data at 330 °C

The difference varied between +0.5% and -4.0% at 300 °C (Fig. 18) while it stayed between -0.5% and +9.5% at 400 °C (Fig. 19).

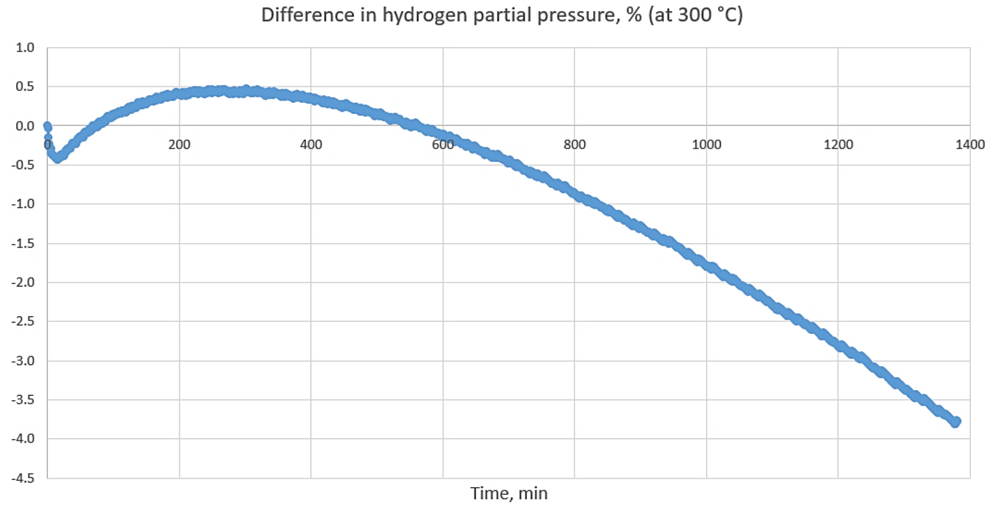

Fig. 18. The relative difference between the model-calculated and the real pressure history at 300 °C

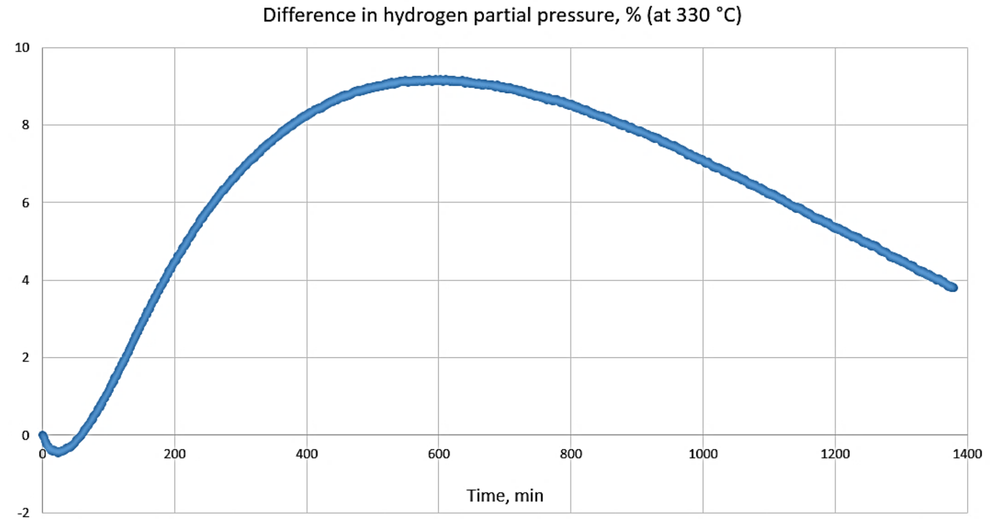

Fig. 19. The relative difference between the model-calculated and the real pressure history at 330 °C

It can be seen at 370 °C (Fig. 20) that the model calculated lower hydrogen uptake rates at higher hydrogen partial pressure while the hydrogen uptake coefficient has been overestimated at lower partial pressure values. It is even more noticeable in the case of 400 °C (Fig. 21).

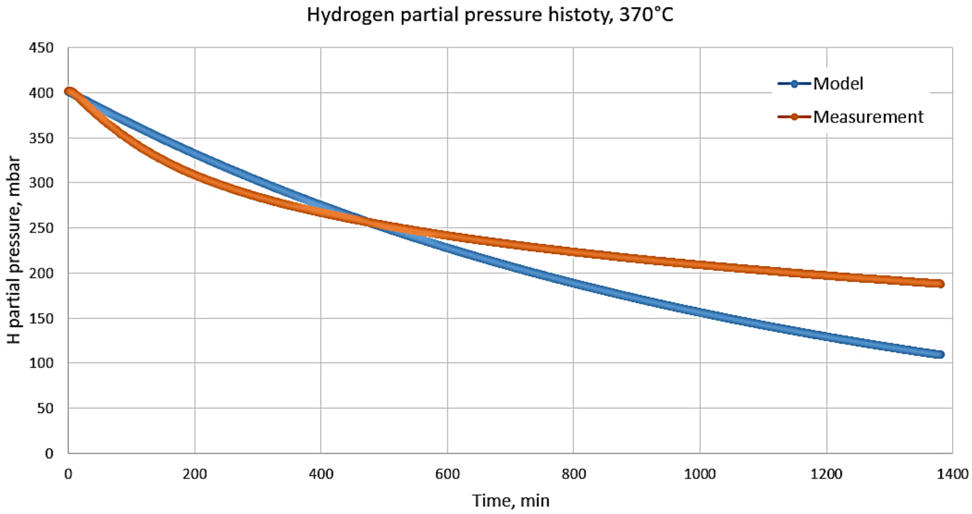

Fig. 20. Comparison of the calculated pressure history and the experimental data at 370 °C

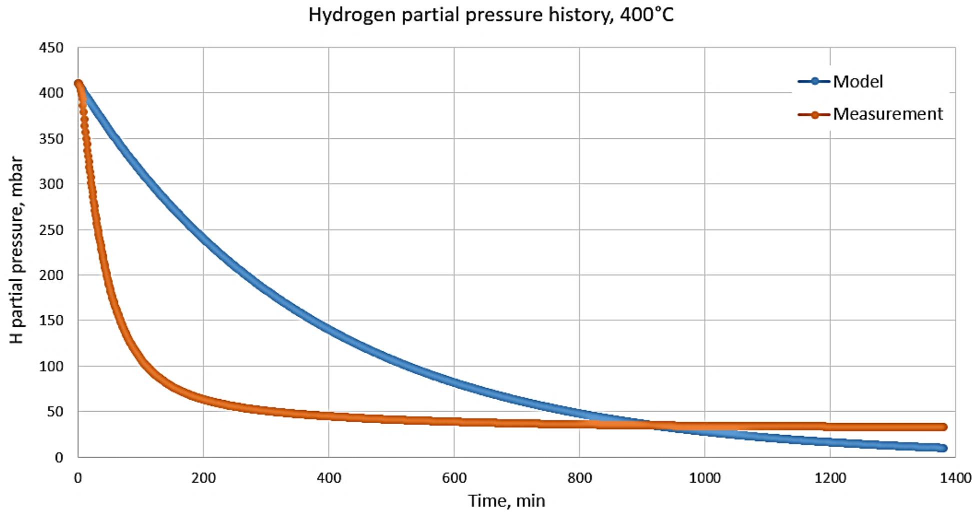

Fig. 21. Comparison of the calculated pressure history and the experimental data at 400 °C

Fig. 22 shows the difference in percent between the pressure history of the model and the experiment carried out at 370 °C. It can be seen that the model goes conservative after ca. 500 minutes (when the partial pressure of the hydrogen gas is less than 250 mbar) by overestimating the hydrogen uptake coefficient resulting in higher hydrogen content of the E110 alloy samples (Table 9).

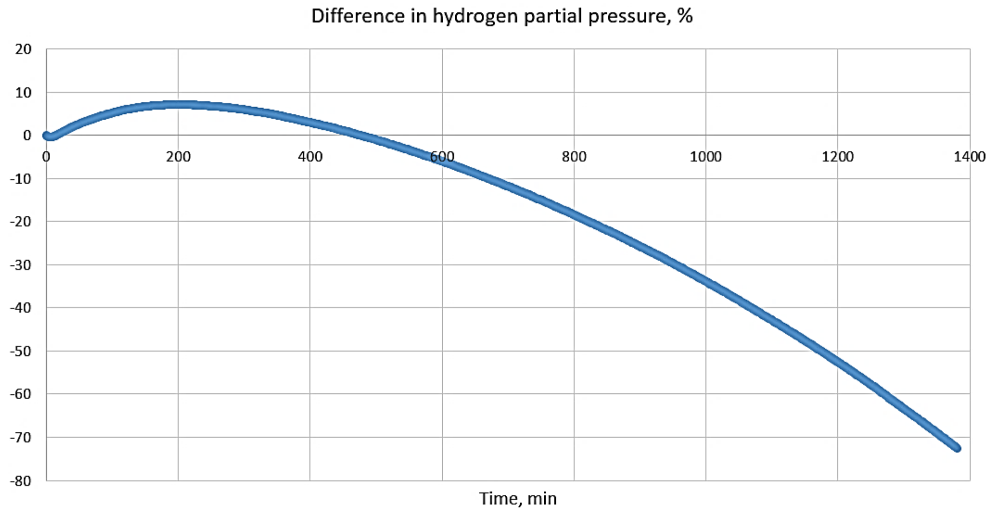

Fig. 22. The relative difference between the model-calculated and the real pressure history at 370 °C

The partial pressure of the hydrogen gas starts to drop quite quickly in the case of 400 °C but the formula can't produce large hydrogen uptake coefficients enough at this temperature. We can see even larger differences at lower partial pressure values which means less difference in pressure (Fig. 23). For example, at the end of the measurement there is a 228% difference but that means only 22 mbar. (Table 8).

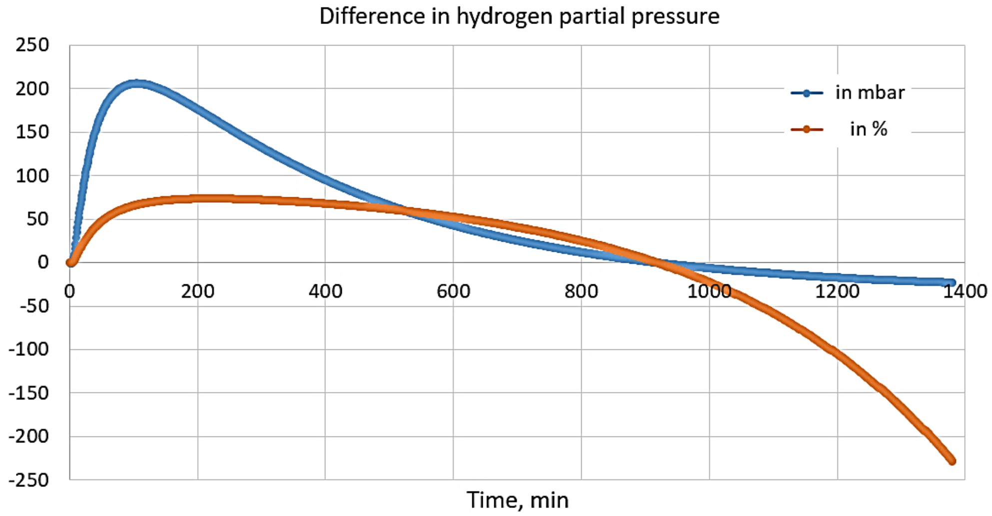

Fig. 23. The absolute and the relative difference between the model-calculated and the real pressure history at 400 °C.

Table 8 summarizes the largest pressure differences between the model calculations and the experimental data at the four temperatures in mbar and in %.

Table 8. The largest differences in hydrogen partial pressure between the model and the experiments

Temperature (°C)	Largest differences (mbar)		Largest differences (%)	
300	- 13.5	+ 1.8	- 3.8	+ 0.5
330	- 1.9	+ 32.5	- 0.5	+ 9.2
370	- 79.0	+23.8	- 72.5	+ 7.1
400	- 22.9	+ 206.2	- 228.3	+ 73.8

Notice that the negative largest difference in mbar should not be coupled to the negative largest difference in percent (at the same temperature) as they don't refer to the same state or moment of the experiment.

As the model can calculate the total amount of the absorbed hydrogen in the samples, there is another way for comparison. Table 9 summarizes the mass gain values given by the model and the calculated mass gains based on the experiments [9].

Table 9. The calculated and the measured hydrogen content of the samples

Temperature (°C)	Calculated hydrogen content (ppm)	Measured average hydrogen content (ppm)
300	319	221
330	825	907
370	2131	1556
400	2887	2746

It can be concluded that the values calculated by the model are higher in 3 cases out of 4 as the model is rather conservative. The values are close to each other at 400 °C, however after checking Fig. 21 it can be said that the dynamics are way more different.

2.4 Summary and conclusions

Hydrogen uptake tests have been carried out Zircaloy-4 and E110G cladding tube samples between 300 and 400 °C in the laboratories of Centre for Energy Research (EK), Hungary. Using the results of these experiments we created a basic numerical model to calculate the hydrogen uptake rate of E110 alloy tube segments.

The experimental series with hydrogen charging of Zircaloy-4 and E110 alloys were successfully completed in the laboratories of Centre for Energy Research.

- The tests covered the temperature range of 300-400 °C.
- The experimental data showed the increase of hydrogen uptake with the increase of temperature.
- The hydrogen uptake of the two tested alloys was significantly different.

The experimental data were collected, and the database is available for model development purposes.

The model we created can cover the temperature range of 300-400 °C and the pressure range of 0-400 mbar using the same simple formula based both on the actual temperature and the partial pressure of the hydrogen gas. The model can also calculate the amount of the total absorbed hydrogen in the samples.
Using this simple formula, the model works well, especially at lower temperatures. At higher temperatures it becomes conservative by overestimating the hydrogen uptake coefficient at lower pressure values.

References

[1] Steinbrück, M. (2004). Hydrogen absorption by zirconium alloys at high temperatures. Journal of Nuclear Materials, 334(1), 58-64.

[2] Yuji Hatano, Kanetsugu Isobe, Ryuji Hitaka & Masayasu Sugisaki (1996) Role of Intermetallic Precipitates in Hydrogen Uptake of Zircaloy-2, Journal of Nuclear Science and Technology, 33:12, 944-949,

[3] Novotny, T., Perez-Feró, E., & Horváth, M. (2015). Hydrogenation and high temperature oxidation of Zirconium claddings. In Mitev, M. (Ed.). 11 International Conference on WWER Fuel Performance, Modelling and Experimental Support Proceedings, (p. 712). Bulgaria

[4] M. Grosse, M. van den Berg, C. Goulet, E. Lehmann, B. Schillinger, In-situ neutron radiography investigations of hydrogen diffusion and absorption in zirconium alloys, Nuclear Instruments and Methods in Physics Research Section A: Accelerators, Spectrometers, Detectors and Associated Equipment, Volume 651, Issue 1, 2011, Pages 253-257,

[5] Choo, K. N., Pyun, S. I., & Kim, Y. S. (1995). Oxidation and hydrogen uptake of Zr based Nb alloys at 400 C under 10 MPa H2O steam atmosphere. Journal of Nuclear Materials, 226(1-2), 9-14.a

[6] Z. Hózer, E. Perez-Feró, T. Novotny, I. Nagy, M. Horváth, A. Pintér-Csordás, A. Vimi, M. Kunstár, and T. Kemény, Experimental Comparison of the Behavior of E110 and E110G Claddings at High Temperature, Zirconium in the Nuclear Industry: 17th Volume, ed. B. Comstock and P. Barberis (West Conshohocken, PA: ASTM International, 2015), 932-951,

[7] Jong-Youl Park, Tae-Hyung Na, Tae-Hyuk Lee, Jong-Hyeon Lee, Bo-Young Lee, Jae-Sung Kim, Effect of applied current on the formation of defect in PWR nuclear fuel rodsin resistance pressure welding process, Journal of Nuclear Science and Technology, 2015 Vol. 52, No. 5, 748–757,

[8] Manual ELTRA ELEMENTRAC ONH-p series, Eltra GmbH, 28.07.2017, Version 0005

[9] P. Szabó, Z. Hózer, Hydrogen uptake tests with zirconium alloys at reactor operational temperatures, technical report EK-2020-437-1-1-M0

3 CIEMAT: Hydrogen migration and precipitation in the cladding

3.1 In-clad hydrogen modelling background

3.1.1 Diffusion

The general equation used to model the diffusion of the hydrogen concentration, H, is based on the Fick's second law. Focusing on the radial direction, r, it is expressed as:

$$\frac{dH}{dt} = -\frac{dJ}{dr} \qquad (1)$$

where H is the hydrogen concentration, J the hydrogen flux and r the radial direction. The hydrogen flux is calculated taking into account both the concentration gradient (Fick's first law) and the temperature gradient (Soret's law):

$$J = -D\left(\frac{dH}{dr} + \frac{Q^{*} \cdot H}{RT^{2}}\frac{dT}{dr}\right) \qquad (2)$$

where D is the diffusion coefficient, Q^* the heat of transport, T the temperature and R the ideal gas constant. The hydrogen concentration is split into dissolved, H_d, and precipitated, H_p, based on the solubility limits, as is shown in the following section. In order to consider the mass transfer through a two phase-region, the volume fraction of the hydride phase, f, is accounted for. It is determined through the ratio between H_p and the local concentration of hydrogen in hydride precipitates, H_δ. The details of D, Q^* and H_δ are reported elsewhere (Stafford, 2015; Veshchunov, 2016).

Moreover, CIEMAT´s implemented an additional contribution to the hydrogen migration based on the effect of the oxidation front (Feria and Herranz, 2018). Particularly, from experimental observations made by Tupin et al. (2015) it is modelled that hydrogen from hydrides incorporated in the oxide are pushed ahead of the oxidation front, which implies inwards transport and reprecipitation of the corresponding hydrogen.

3.1.2 Precipitation/dissolution

3.1.2.1 *Classic*

The classic modelling of hydrogen precipitation/dissolution in the zirconium alloy is based on empirical terminal solid solubilities concerning precipitation (TSS_p) and dissolution (TSS_d), assuming that there is hysteresis (Courty et al., 2014). Thus, precipitation occurs when the matrix is oversaturated with hydrogen, but stops when the precipitation limit is reached. The calculation of the precipitation rate is based on the linear approximation in the hydride precipitation model (Marino, 1972); concretely, the rate of precipitation was measured to be proportional to the hydrogen supersaturation. If the concentration in solid solution lies between TSS_p and TSS_d (i.e., hysteresis area), neither dissolution nor precipitation occurs. When the concentration in solid solution is below the TSS_d, there is only change in the precipitation rate if hydrides are present (i.e., dissolution of the hydrides). Therefore, the precipitation rate is determined from TSS_p, TSS_d and the precipitation and dissolution rate parameters (k_p and k_d, respectively):

$$\frac{dH_p}{dt} = \begin{cases} k_p \cdot (H_d - TSS_p) \text{ if } H_d > TSS_p \\ 0 \text{ if } TSS_p \geq H_d > TSS_d \\ k_d \cdot (H_d - TSS_d) \text{ if } H_d \leq TSS_d \text{ and } H_p > 0 \\ 0 \text{ if } H_d \leq TSS_d \text{ and } H_p = 0 \end{cases} \qquad (3)$$

The solubility limits are estimated through an Arrhenius function with temperature. The dissolution kinetics is usually assumed to be very fast compared to the precipitation kinetics, as is shown in Figure 1. The details of these parameters are shown elsewhere (Stafford, 2015; Veshchunov, 2016).

3.1.2.2 New

Recent work has brought a new model based on experimental evidence (Passelaigue et al., 2021). In this model, hydride precipitation is divided into nucleation of new hydrides and growth of existing ones. Nucleation and growth of new hydrides occurs when the dissolved hydrogen is above the TSS_p, which is identified as the supersolubility limit. The TSS_d is identified as the only thermodynamic solubility limit and the growth of existing hydrides occurs when the solid solution content is above. The kinetics of precipitation by hydride growth is described using the Johnson-Mehl-Avram-Kolmogorov model (Avrami, 1939). In this model hydride dissolution is no longer considered instantaneous.

The equations describing this model are the following:

$$\frac{dH_p}{dt} = \begin{cases} k_N\cdot\left(H_d - TSS_p\right) + k_G\cdot(H - TSS_d)\cdot p\cdot(1-x)\cdot(-\ln(1-x))^{1-1/p} \text{ if } H_d > TSS_p \\ k_G\cdot(H - TSS_d)\cdot p\cdot(1-x)\cdot(-\ln(1-x))^{1-1/p} \text{ if } TSS_p \geq H_d > TSS_d \\ k_D\cdot(H_d - TSS_d) \text{ if } H_d \leq TSS_d \text{ and } H_p > 0 \\ 0 \text{ if } H_d \leq TSS_d \text{ and } H_p = 0 \end{cases} \tag{4}$$

where K_D, K_N and K_G are the kinetic parameters for dissolution, nucleation and growth, respectively, which are function of the temperature (K_G also depends on the precipitated hydrides), x is a measure of the advancement of the precipitation reaction and p is the dimensionality of the growth. The details of the model's parameters are given in Passelaigue et al. (2021).

In order to compare the kinetic parameters used by each model, Fig. 24 illustrates the evolution of these parameters with the temperature. Different trends with the temperature are observed regarding the modelling of each parameter for dissolution and precipitation. Note that the kinetic parameter for nucleation used by the new modelling is various orders of magnitude greater than the kinetic parameter for precipitation used by the classic modelling.

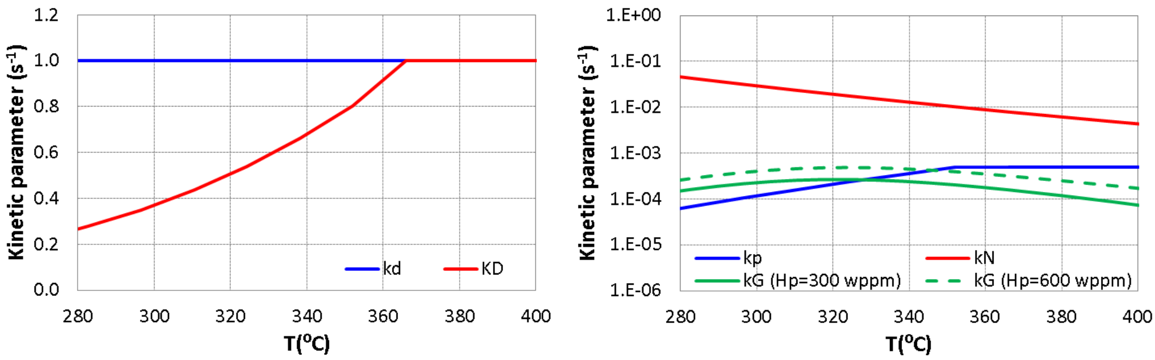

Fig. 24. Kinetic parameters for dissolution (figure on the left) and for precipitation (figure on the right with y-axis in logarithmic scale) as a function of temperature

3.2 CIEMAT´s model

3.2.1 Overview

CIEMAT derived a 1D model of the hydrogen performance across the cladding thickness (i.e., radial distribution) (Feria and Herranz, 2018). It is based on the formulation previously described with the classic precipitation/dissolution modelling. The model is solved by the numeric method of finite differences. To do that, the time step, Δt, and the number of radial nodes throughout the cladding thickness, N, are defined in the input of the model, as well as the initial conditions (i.e., as-fabricated cladding thickness, th, and hydrogen concentration, H_i) and the end time, t_{end}.

Regarding the boundary conditions (i.e., hydrogen pickup, H_{pk}, oxide thickness, δ_{ox}, and thermal conditions), the model is adapted to account for them both through the input and by the coupling with a fuel performance code. Particularly, the model is prepared to be coupled with the FRAPCON code (version 4.0) (Geelhood et al., 2015). The hydrogen pickup provided by FRAPCON is used as the boundary condition in the waterside node and the oxide thickness given by the code is used for the above-mentioned oxidation front modelling. Concerning the thermal conditions, FRAPCON calculates the inner and outer cladding temperature (T_{in} and T_{out}, respectively), so the model uses these values to estimate the thermal gradient in the nodes established; to do that, a linear interpolation is assumed. Fig. 25 illustrates the coupling described.

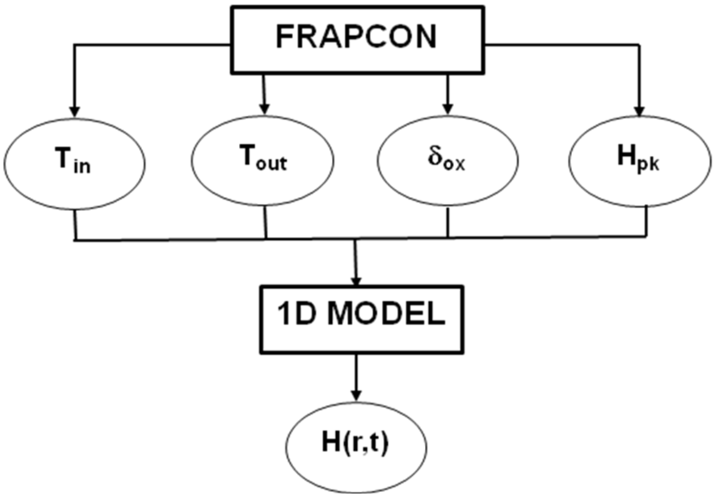

Fig. 25. Model coupling with FRAPCON.

3.2.2 Adaptation

The CIEMAT´s model has been adapted to account for the hydrogen pickup in the cladding fuel side through a parameter controlled by the input (f_{pk}); this parameter represents a hydrogen concentration instantaneously available at the gap-cladding interface at a given time, which is also set in the input (t_{sh}). This hydrogen pickup is given as an average across the cladding thickness. Concerning this boundary condition, although further adaptation is foreseen to be done in FRAPCON in order to simulate the anticipated scenario of secondary hydriding in defective fuel rods, the parameterization implemented is enough to reach the goal of the study carried out so far.

Additionally, another adaptation carried out in this work has been the implementation of the new modelling of precipitation/dissolution shown in section 2.2.2 as an alternative option in the CIEMAT´s model. Furthermore, given the variability found in the TSSs (Zanellato et al., 2012), alternative options to the ones considered by default (McMinn et al., 2000) have been added. Particularly, the correlations given by Kearns (1967) (for TSS_d) and

Zanellato et al. (2012) (for TSS_d and TSS_p) have been implemented. Fig. 26 depicts the TSSs taken into account in the model. As it can be seen from the curves represented, the variability is not negligible, especially between McMinn's and Zanellato's curves (relative deviations greater than 30% at 300 ºC).

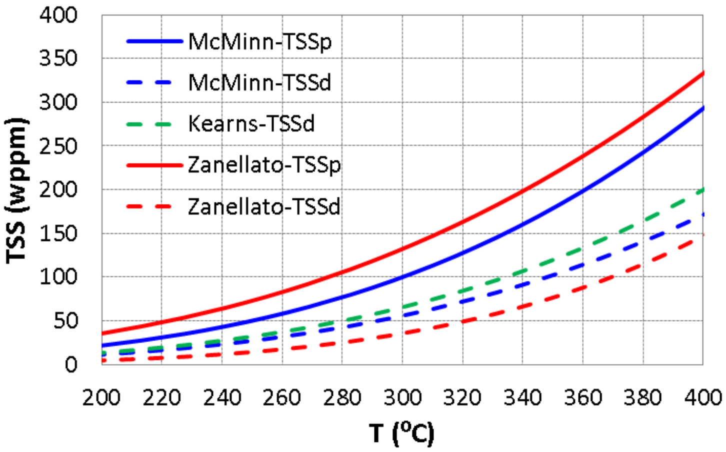

Fig. 26. TSS curves implemented in the model.

3.3 Assessment

3.3.1 Separate effect test

The CIEMAT´s model adaptations concerning precipitation/dissolution modelling have been checked through data from an experiment that consists of a series of thermal transients applied to a 254 wppm hydrogen-loaded sample (Lacroix et al., 2018). It was designed to highlight the different phenomena occurring in the sample by inducing successive dissolution and precipitation.

Figure 4 shows the heating and cooling cycles at which the sample was submitted (red dashed line), as well as the model-to-data comparison in terms of the dissolved hydrogen concentration evolution. The different modelling options cited above have been checked. Particularly, the results from the classic and new precipitation/dissolution approaches have been represented; in each case, two options of the TSSs correlations available in the model have been simulated: the option by default (McMinn's correlations for TSS_d and TSS_p) and the option that better fits to the solubility limits observed with the experimental data (Kearn´s correlation for TSS_d and Zanellato's correlation for TSS_p).

From Fig. 27, it can be observed that the classic modelling of precipitation/dissolution does not capture the evolution of the dissolved hydrogen, while the new modelling follows the data trend. The divergences of the classic modelling appear from the first cooling cycle, due to the fact that the precipitation kinetics applied is too slow to simulate the precipitation observed. On the contrary, the nucleation and growth modelling for precipitation notably enhances the prediction by capturing the observed precipitation rate after each cooling. It has been checked that there is no difference between using the classic kinetic parameter for dissolution or the new one. Furthermore, it is shown that the TSSs notably impact the prediction made; indeed, the option used by default gives rise to important deviations with respect to the experimental data in the case of using the new modelling.

It should be noted that further validation of the new modelling of hydrogen precipitation/dissolution is shown in Passelaigue et al. (2021), although with hydrogen concentrations up to 300 wppm. In spite of the fact that further validation would be needed at higher hydrogen contents, an extrapolation out of the validity range of the new modelling is assumed, given that it brings an improved understanding of the physics involved in hydride precipitation and dissolution.

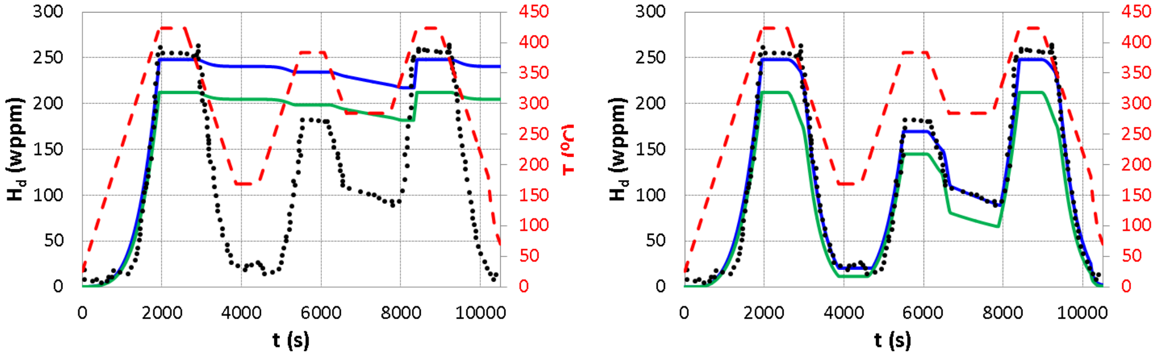

Fig. 27. Evolution during the simulated experiment of the temperature (red dashed line) and the dissolved hydrogen, both measured (black dots) and predicted with the classic modelling (figure on the left) and with the new modelling (figure on the right), by using the TSSs by default (green line) or the fitted TSSs (blue line).

3.3.2 Postulated secondary hydriding scenario

The above shown effect of the precipitation/dissolution modelling has been assessed in the context of a secondary hydriding; particularly, it has been studied on the hydrogen distribution after a massive hydriding in a Zircaloy-4 fuel rod that becomes defective at the beginning of life.

The coupling between the CIEMAT´s model for in-clad hydrogen performance with FRAPCON has been used to simulate the target scenario. To obtain the beginning of life conditions, a typical PWR 17x17 fuel rod irradiated to an average linear power close to 20 kW/m has been simulated with FRAPCON; the details of rod design and irradiation are shown elsewhere (Feria et al., 2020). The study has been focused on the upper part of the fuel rod, where cladding temperatures of 378ºC and 348 ºC has been obtained in the inner and outer side, respectively (cladding thickness of 570 μm).

Based on the CIEMAT´s model, two cases of massive hydriding have been analysed through the parameter f_{pk}, by imposing 500 wppm and 5000 wppm, as approximated observed bounds from fuel rods submitted to secondary hydriding (Matsson, 2006). In both cases, the massive hydriding in the cladding fuel side has been simulated after 30 days of irradiation (i.e., t_{sh}=30 days), assuming a previous entrance of water due to the defect in the cladding.

Fig. 28Fig. 27 represents the results obtained in terms of the precipitated hydrogen distribution across the cladding thickness. Two times after the massive hydriding have been analysed: once an important hydrogen concentration reaches the outer half of the cladding (1 hour) and after the hydrogen migration reaches the steady state (1 month). The predictions of the different modelling options studied in this work have been represented in the figures. The following observations should be highlighted:

The classic modelling gives rise to a rapid distribution across the whole cladding thickness of the hydrogen absorbed, even at 1 hour and the lower hydrogen pickup. This means that the in-clad hydrogen performance is governed by the diffusion mechanisms (related to concentration and temperature gradients), which lead to a migration rate faster than the precipitation rate.

The new modelling results in a slower distribution across the cladding thickness of the hydrogen absorbed, giving rise to localized accumulation of hydrides which extension depends on the hydrogen absorbed, as expected (i.e., the higher the pickup the higher the extension). This is due to the faster precipitation rate simulated (through the nucleation and growth kinetic parameters), which is capable of slowing down the diffusion mechanisms. It has been checked that the diffusion due to the temperature gradient (i.e., Soret effect) is the responsible for the hydride's accumulation in the outer side of the cladding (i.e., the deactivation of the Soret effect avoids the accumulation of hydrides in this side).

The TSSs variability does not show an important impact on the in-clad hydrides distribution, independently of the precipitation/dissolution modelling used. Only in the case of lower hydrogen pickup (f_{pk}=500 wppm) applying the new modelling, some effect is observed in the extension of the hydride's accumulation.

Therefore, the results obtained in this work point out that the predictability enhancement of the in-clad hydrides distribution in case of secondary hydriding implies to properly model the hydrogen precipitation. In this regard, further verification/validation is foreseen based on data made available. To do so, further adaptation is foreseen to be done in order to properly simulate the boundary conditions anticipated in defective fuel rods.

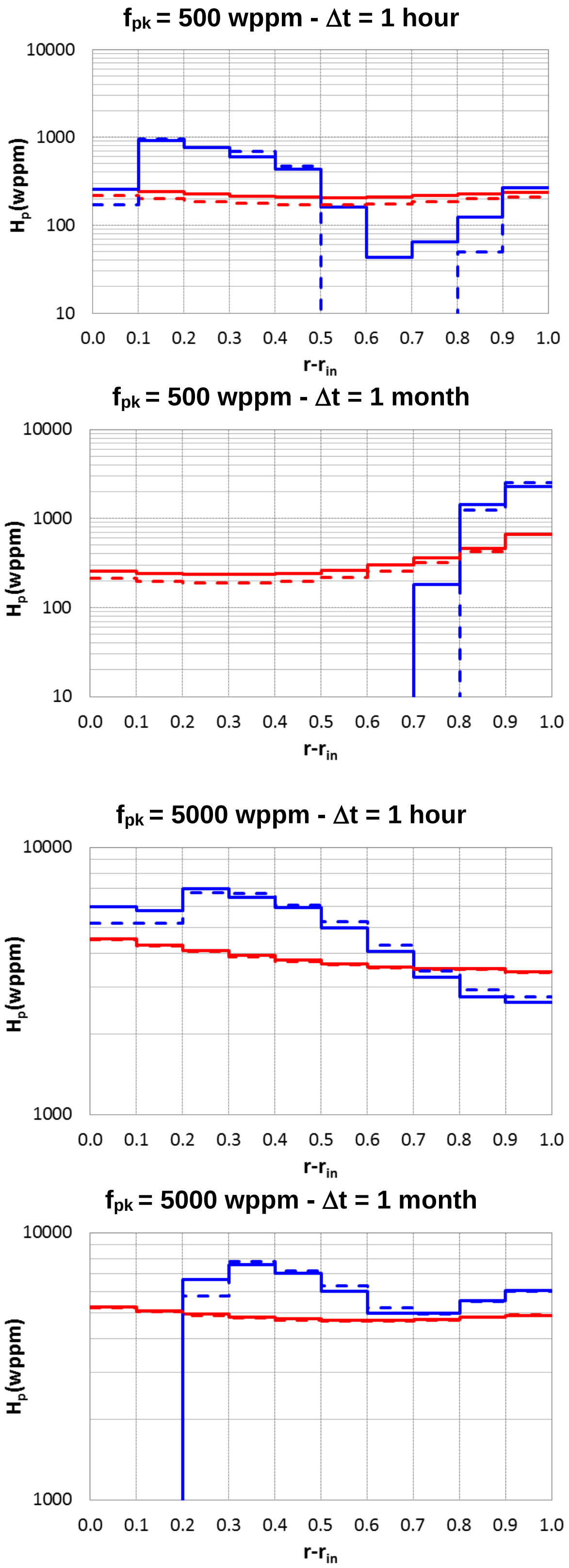

Fig. 28. Precipitated hydrogen distribution across the cladding thickness (normalization of the radius, r, minus the inner radius, r_{in}) at different times, Δt, after the massive hydriding simulated, f_{pk}. Comparison of the classic modelling (red lines) with the new modelling (blue lines) and the TSSs by default (continuous lines) with the fitted TSSs (dashed lines).

References

[1] Avrami, M., 1939. Kinetics of Phase Change. I General Theory, The Journal of Chemical Physics, 7, 1103–1112.

[2] Courty, O.F., Motta, A.T., Hales, J.D., 2014. Modeling and simulation of hydrogen behavior in Zircaloy-4 fuel Cladding. Journal of Nuclear Materials, 452, 311-320.

[3] Feria, F., Herranz, L.E., 2018. Effect of the oxidation front penetration on in-clad hydrogen migration. Journal of Nuclear Materials, 500, 349-360.

[4] Feria, F., Aguado, C., Herranz, L.E., 2020. Methodology for a realistically conservative characterization of spent fuel in dry storage. Annals of Nuclear Energy, 140, 107148.

[5] Kearns, J.J., 1967. Terminal solubility and partitioning of hydrogen in the alpha phase of zirconium, zircaloy-2 and zircaloy-4. Journal of Nuclear Materials, 22, 292-303.

[6] Lacroix, E., Motta, A., Almer, J., 2018. Experimental determination of zirconium hydride precipitation and dissolution in zirconium alloy. Journal of Nuclear Materials, 509, 162–167.

[7] Marino, G.P., 1972. A numerical calculation of the redistribution of an interstitial solute in a thermal gradient. Nuclear Science and Engineering, 49, 93-98.

[8] Matsson, I., 2006. Studies of Nuclear Fuel Performance Using On-site Gamma-ray Spectroscopy and

[9] In-pile Measurements. Dissertation presented at Uppsala University, ISBN 91-554-6582-X.

[10] McMinn, A., Darby, E.C., Schofield, J.S., 2000. The terminal solid solubility of hydrogen in zirconium alloys, in: 12th Int. Symp. On Zr in the Nuclear Industry, Toronto, CA, pp. 173-195.

[11] Passelaigue, F., Lacroix, E., Pastore, G., Motta, A.T., 2021. Implementation and Validation of the Hydride Nucleation-Growth-Dissolution (HNGD) model in BISON. Journal of Nuclear Materials, 544, 152683.

[12] Stafford, D.S., 2015. Multidimensional simulations of hydrides during fuel rod lifecycle. Journal of Nuclear Materials, 466, 362-372.

[13] Tupin, M., Bisor, C., Bossis, P., Chêne, J., Bechade, J.L., Jomard, F., 2015. Mechanism of corrosion of zirconium hydride and impact of precipitated hydrides on the Zirclaoy-4 corrosion behavior. Corrosion Science, 98, 478-493.

[14] Veshchunov, M.S., Shestak, V.E., Ozrin, V.D., 2016. A new model of hydrogen redistribution in Zr alloy claddings during waterside corrosion in a temperature gradient. Journal of Nuclear Materials, 472, 65-75.

[15] Zanellato, O., Preuss, M., Buffiere, J.Y., Ribeiro, F., Steuwer, A., Desquines, J., Andrieux, J., Krebs, B., 2012. Synchrotron diffraction study of dissolution and precipitation kinetics of hydrides in Zircaloy-4. J. Nucl. Mater. 420, 537-547.

4 IRSN: Simulation of secondary hydriding

IRSN contribution to task 4.3 is divided into two parts:

- A bibliographic study of the secondary hydriding phenomena (see [33]),
- Secondary hydriding modelling in the SHOWBIZ software [34].

IRSN completed a review of available literature on secondary hydriding phenomena during normal operating condition and of French Nuclear Power Plants experience of defective fuel rods during normal operation [33]. Since the first observations of such degradations, especially for boiling water reactors, scenarios have been proposed to explain the origin of secondary hydriding. Among the mechanisms involved, some of them are now widely accepted and have been confirmed by a few integral tests. This is the case of the internal oxidation of the cladding as a source of hydrogen or steam depletion conditions necessary for massive hydriding. However, the kinetics and triggering of such hydriding are still subject to controversy. For instance, incubation times, internal communication of gaseous species and loss of protection by the internal zirconia are still open questions.

This bibliographic report allows the implementation of models in the version 2022 of the SHOWBIZ software [36]. They take advantage of laws already implemented in SHOWBIZ and which will be parameterized based on experimental results found in the literature, in particular the clad oxidation and hydriding rates. The implementation of a model inspired by the Veschunov's model has been established to treat the gas mixture/transport in the gap. A massive hydriding model compatible with the SHOWBIZ software architecture has been envisaged.
The technical report [34] resumes this contribution.

IRSN has then developed a multi-physics model in order to simulate the secondary hydriding phenomena from the water ingress to the formation of hydrides blister. In particular, the dedicated CHANNEL module in the SHOWBIZ software deals with the internal gas mixture and transport that are calculated together with the chemical interaction with the inner side of the fuel rod clad. A coupling of this 1D structure with the 3D cladding geometry has also been achieved and allows to consider both hydrogen and oxygen uptake coming from internal oxidation and hydriding processes. Pre-existing models for hydrogen bulk diffusion were used for modelling the H redistribution in the cladding.

4.1 Secondary hydriding during normal operating condition: IRSN bibliography

4.1.1 Description of the secondary hydriding phenomena

Secondary hydriding phenomena during normal operating condition have been a major issue for BWR in the last 80s. A great amount of work has been done and most of the studies are related to this context. In fact, during rapid power ramp transients using the control rods, cracks were created by pellet-clad interaction [1], resulting in so-called primary defects and a leaking fuel rod. Secondary defects then appear, and significant degradation of defective fuel rods were observed. Such severe degradation that affected Zircaloy alloy and consisted mainly of hydrides blisters or axial cracks, but in the most severe case end cap rupture or extended fracture (2-3 meters) were observed.
For the PWR, the occurrence of defective fuel rods is unusual and the secondary hydriding degradation is less severe. Hence, few data and experimental studies are available in the literature. However, feedback from NPP operating experience shows that the primary defects are often attributed to grid or migrating debris fretting and more rarely to manufacturing defect. Number of defective fuel rods in PWR have been drastically reduced with design modification such as anti-debris filters or reinforcement bottom grid. During the past ten years, the assembly failure rate has been reduced to lower than 0.2% in French NPP.
Nevertheless, defective fuel rods with secondary defects are very unfavorable for the operator because it can lead to radionuclides release in the primary circuit, maneuverability restrictions, or even premature shutdown and unloading of the defective assembly. In some cases, where the secondary defects are significant in size, fuel

washout may occur with consequences such as the release of volatile radionuclides, dissemination of fissile material in the primary circuit and increased risks in terms of radiological consequences. Finally, handling of defective fuel rods with secondary defects can also be problematic due to the risk of breakage. The extraction of an affected fuel rod might be impossible due to the risk of fracture and thus prevent any repair of the assembly.

4.1.2 Primary defect root causes

Loss of integrity of fuel rods are associated to different types of primary defects. Among the causes identified as being at the origin of primary defects, we note mainly localized vibratory usury of the rods. This is the phenomenon of fretting, for which the origin can be:

- a lack of support in the cells of the lower grid,
- the presence of abnormal crossflows which increase the vibration of the rods,
- cracking of the grid springs by stress corrosion and subsequent degradation of fuel rod holding,
- the presence of small migrating debris trapped in the grid cells,
- localized corrosion induced by the presence of CRUD-type corrosion deposits (CILC),
- manufacturing-related reasons such as welding defects of fuel end cap.

4.1.3 Secondary hydriding sequence

Following the occurrence of a primary defect, water enters the fuel rod through this defect. On contact with the very hot pellets, the water vaporizes and progresses through the free volumes of the fuel rod until the internal pressure of the rod and the pressure of the primary circuit are balanced. The presence of steam inside the fuel rod causes an oxidation reaction of the cladding and the fuel. This oxidation reaction together with radiolysis of the water leads to a release of hydrogen. A steam-hydrogen mixture thus propagates through the rod free volumes. This mixture becoming richer in hydrogen as the oxygen is consumed by oxidation. In parallel, the oxidation of the clad creates a protective oxide layer on the inner side of the cladding.

When the amount of hydrogen is sufficiently high, and the amount of oxygen is no longer sufficient to sustain the oxidation reaction on the inner side of the cladding (steam starvation), the conditions for hydrogen uptake by the cladding are reached. Massive hydriding of the cladding can then occur if the inner oxide layer is no longer sufficiently protective - too thin inner oxide layer or radial cracking of this layer allowing easy diffusion of hydrogen to the metal.

This phenomenon is generally favored if it occurs locally at cold spots, characterized as high-stress regions with very high (thousands of ppm) hydrogen content. At such concentrations, the hydrogen absorbed by the cladding precipitates in the form of hydrides whose accumulation leads to the formation of secondary defects. Depending on the development of the secondary hydriding phenomenon, a secondary defect gradually takes the form of a high local hydrogen content or an accumulation of hydrides leading to cladding blistering.

Further damage to the defective fuel rod is then possible either by the evolution of the secondary defect until the perforation of the clad, or departure of cracks from the secondary defect associated with various mechanical stresses (thermomechanical loading of the rod during a power ramp or incidental/accidental driving scenario).

Secondary hydriding therefore takes place in three phases:

- An incubation phase between the onset of the primary defect and the moment when the conditions for massive hydriding are met;
- A hydriding phase during which the clad is subject to hydrogen uptake and the secondary defect is formed;
- A damage phase during which a crack appears from the secondary defect either by external mechanical stress or by evolution of the secondary defect.

The main physical mechanisms identified are:

- In the incubation phase:
  - The water ingress into the gap and the characterization of the primary defect,
  - The circulation of gases (steam-hydrogen mixture) in the free volumes, in particular the pellet-clad gap,
  - The creation of hydrogen (radiolysis, fuel oxidation, cladding oxidation),

  - The oxidation of the cladding on the inner side and its protective character.
- In the hydriding phase:
  - Hydriding caused by the release of hydrogen from the cladding oxidation,
  - Massive hydriding under the necessary conditions:
    - Concentration of the gas mixture with steam starvation (critical p_{H2}/p_{H2O} ratio),
    - Loss of the protective character of the internal oxide layer (reduction/cracking),
  - Radial and axial diffusion of hydrogen in the cladding,
  - Precipitation of hydrides,
  - The formation of secondary defects.
- In the damage phase:
  - The influence of hydrogen concentration on mechanical properties,
  - Localized embrittlement of the cladding by hydrogen and hydrides,
  - Crack propagation in the presence of hydrogen,
  - Determination of the thermomechanical stresses that can lead to further damage.

4.1.4 Typology of secondary defects

Post-irradiation examinations (PIE) show different types of secondary defects which can be classified according to their morphology and severity. Depending on their degree of development, secondary defects may not be open or may result in a crack of a few millimeters. For BWR and in rare cases for PWR, very extensive secondary defects have been observed. Thus, secondary defects can be classified as follows:

- massive localized hydriding, known as hydride **blister**. A large accumulation of hydrides can be observed in the inner side of the clad with a size of about one millimeter;
- the **sunburst**. A local increase in volume is induced by the formation of a massive hydride in the inner side of the clad, together with radial hydrides radiating through the thickness of the cladding. A second blister is likely to be formed opposite at the outer side of the clad;
- **perforation** is the ultimate stage in the evolution of a blister / sunburst. The blister is all through the clad and the apparent hole is of the order of a millimeter. The fuel is visible from the outside of the rod. This configuration leads to a significant dissemination of fuel particles in the primary circuit;
- small **cracks** that can be axial, circumferential or transverse and often start from a massively hydrided region. The size of small cracks is in the order of a millimeter.

These defects can lead to severe degradation of the fuel rod resulting from the ultimate evolution of the previous stages. Two specific forms are observed:

- axial fracture extending over several cm or even dm, formed by propagation of a smaller crack created from a secondary defect. This type of degradation leads to a significant release of volatile fission products and can result in significant contamination of the primary circuit with loss of fuel containment.
- « guillotine » rupture, massive hydriding takes place all over the circumference of the clad and causes a rupture of the clad into two sections[1].

  These ruptures can also be associated with the presence of hydride rings that weaken the cladding, particularly at cold spots, where the hydrogen solubility limit is low. The presence of temperature or stress gradient will favor the formation of these highly-hydrided regions. It is common to observe hydride rings in between pellets areas, which are colder than the current part [1]. Observations are also reported at the top cap, in areas affected by the melting of the liner during the welding process [1].

---

[1] Ruptures of this type appear to have been caused by handling operations [1].

4.1.5 French NPP feedback

4.1.5.1 Type and location of secondary defects

A secondary defect can occur whatever the primary defect type. The secondary defect type does not seem to be influenced by the nature of the primary defect. The distribution of the secondary defect type is equivalent between crack type defects and sunburst type defects. The most common type of cracks encountered are axial cracks, circumferential cracks being unusual. However, the location of the secondary defect depends on the location of the primary defect. Indeed, a large majority of primary defects are located in the lower part of the assembly because the vibrations are more important, and the debris are generally blocked at the first grid. In such cases, secondary defects are often observed 2 to 3 meters above, at the upper part of the fuel rod.

Small distances between primary and secondary defects are systematically associated with a very small primary defect (non-through weld defect type).

The occurrence of a secondary hydriding zone is not systematic. The phenomena can be delayed by the low oxidation kinetics of the inner side of the clad and by the closure of the gap between the pellet and the cladding, which limits the quantity of steam inside the fuel rod. However, about half of the defected fuel rods develop one or more secondary defects. The number of secondary defects is lower when the primary fault is located in the maximum heat flux zone (between grid 2 and grid 8 on 900MW PWRs) and several secondary defects can be observed when the primary fault is close to a plenum.

4.1.5.2 Influence of the irradiation time

The occurrence of secondary defects in defective fuel rods does not seem to be influenced by the irradiation time. The number of secondary defects is not obviously correlated to the irradiation duration starting from the detection of a primary defect. In one hand, it is observed that many secondary defects can occur shortly after the primary defect, and on the other hand that many fuel rods with primary defects do not develop secondary defects even after a very long irradiation time (full cycle). It has to be noticed that this observation has not been linked with the size of the primary defect.

Furthermore, the burnup of the fuel rod at the time of the primary defect appearance does not seem to have any influence on the number or the axial position of the secondary defects. As the burnup is correlated with the size of the pellet-clad gap (whose opening or closing can influence the axial transport of steam and hydrogen), it is possible to deduce from these observations that the development of secondary defects could be independent of the open/closed state of the gap. However, such a statement is subject to debate.

4.1.5.3 Influence of the irradiation power

The occurrence of secondary defects is correlated with the average power of the defective rod. The number of secondary defects is as high as the average power of the rod is higher. It is highly probable that a defective fuel rod will develop secondary defects above 150W/cm. Severe degradation is observed in particular for high power operating rods [3].

4.1.6 Physical and chemical mechanisms involved

The important physical mechanisms identified are detailed in the following.

4.1.6.1 Incubation phase

It is reminded that the appearance of a secondary defect following a primary defect is not immediate and can take from a few days to a hundred days.

Water ingress and steam propagation in free volumes

Just after the occurrence of a primary defect in normal PWR operation, the coolant pressure (outside the rod) is much higher than the internal pressure of the rod. Thus, water enters in the fuel rod. In contact with the hot pellets, the water vaporizes and spreads into the free volumes inside the rod until the internal and external pressures are balanced.

In a second step, the steam is consumed either by oxidation or radiolysis. Oxidation contributes to the creation of an inner oxide layer and the release of hydrogen. The pressure of the steam-hydrogen mixture decreases as the reaction proceeds, allowing water to enter again in the rod. The partial pressure of steam decreases and the partial pressure of hydrogen increases: the further away from the primary defect, the more hydrogen-rich is the gas mixture.

Very small primary defects (needle-sized holes or small cracks of about 100 microns) do not always cause significant hydriding in the reactor. In particular, these very small defects can be re-filled quickly after their appearance, as localized corrosion forms an oxide that is larger than the metallic phase and fills the defect [6]. On the other hand, very small defects (weld defects) generally generate secondary hydriding close (0.5-1 m) to the primary defect.

Oxidation at the inner face

The inner face oxidation phenomenon is one of the key mechanisms to understand secondary hydriding. As the protective character of the oxide layer towards hydriding is commonly accepted, a necessary condition for the initiation of massive hydriding is the absence of the oxide layer or the loss of its protective character. This fundamental point is the subject of several hypotheses discussed later on.

Internal oxidation differs from external oxidation. On one hand, the oxidation takes place in the steam phase and not in the liquid phase and, on the other hand, the internal cladding temperature is higher than the external temperature. The effects of irradiation are also greater inside the fuel rod.

In the case of a primary defect leading to steam entry and due to the conditions mentioned above, the corrosion rate and thickness of the internal oxide layer is significantly increased compared to further away regions [4].

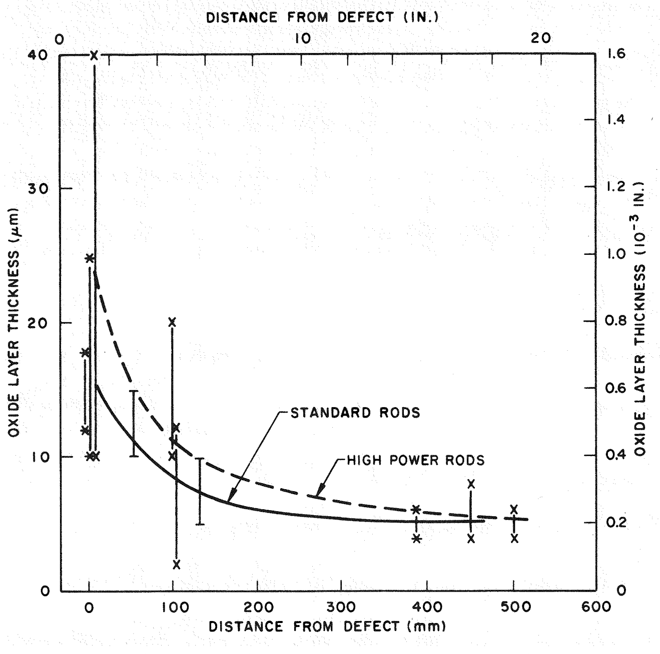

Fig. 29. Internal oxide thickness as a function of distance from primary defect. Post-irradiation measurements of a defective Zircaloy rod [4]

It is commonly accepted that the internal oxide is thick close to the primary defect and gets thinner as one moves away from the primary defect (see Fig. 29). However, temperature is the most important parameter in the kinetics of the oxidation reaction and in the case of a peaked heat profile along the rod, the oxide thickness also follows the temperature profile (see Fig. 30).

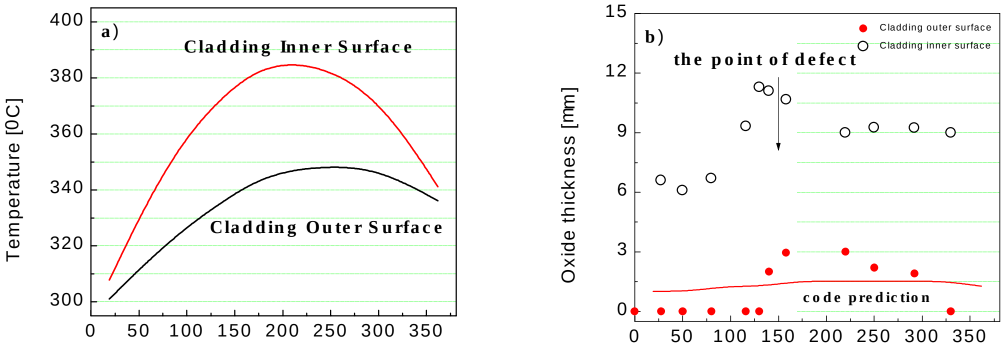

Fig. 30. Thickness of internal and external oxide layer as a function of clad temperature on defective B208-R8 rod (reactor case) [12]

According to Lee et al [23], the oxidation with steam-hydrogen gas mixture for temperatures between 300 and 500°C follows a cubic evolution law with:

$$\Delta W_{ox}^{3} = k_{ox} t$$
$$k_{ox} = k_{ox}^{0} \exp\left(-\frac{Q_{ox}}{RT}\right)$$

Hydrogen sources

Internal oxidation of the cladding

The presence of steam in contact with the inner face of the clad causes an oxidation reaction. The reaction is as follows:

$$Zr + 2\,H_2O \rightarrow ZrO_2 + 2H_2$$

The oxidation reaction releases hydrogen. Some of this hydrogen is consumed during the reaction by hydriding the cladding. The other part is released and contributes to the formation of a steam-hydrogen mixture in the free volumes. The hydrogen release kinetics directly follows the oxidation kinetics with a hydrogen release rate of about 75-90% for Zircaloy-4. It is the most important source of hydrogen enrichment of the gas mixture in the pellet-clad gap [4].

Radiolysis of water

Radiolysis reaction can break down water and release hydrogen:

$$H_2O \rightarrow H^{+} + OH^{-}$$
$$2H_2O \rightarrow H_2 + H_2O_2$$

The former is more likely in the presence of γ radiation and the latter in the presence of α particles due to fission products. Hydrogen production by radiolysis is a non-equilibrium phenomenon because the rate of recombination of free radicals is much lower than the rate of their production. In addition, the peroxide can react with the fuel and contribute to the creation of even more hydrogen. There is no consensus on the contribution of radiolysis of water to the creation of hydrogen; it is likely to contribute to the enrichment of the gas mixture [5] or is negligible compared to internal oxidation according to some authors [7].

Fuel oxidation

The steam present in the free volumes of the defective fuel rod can lead to fuel oxidation during the incubation phase. Fuel oxidation is therefore potentially a significant source of hydrogen in a defective fuel rod [7].
The fuel reacts directly with steam according to the reaction:

$$2H_2O + \frac{2}{\varepsilon} UO_{2+x} \rightarrow 2H_2 + \frac{2}{\varepsilon} UO_{2+x+\varepsilon}$$

or with the peroxide released by the radiolysis of water

$$H_2O_2 + \frac{2}{\varepsilon} UO_{2+x} \rightarrow H_2 + \frac{2}{\varepsilon} UO_{2+x+\varepsilon}$$

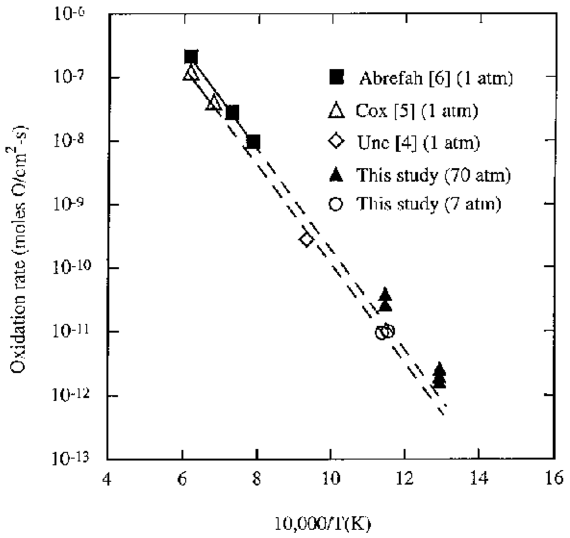

Fig. 31. Steam oxidation rate of UO2 fuel [9]

Only few studies concern the oxidation rate of UO_2 at low temperatures. For temperatures of the order of 500 to 600°C, the stable phase of uranium oxide is U_3O_8 and the UO_2 fuel is in substoichiometry with a probable affinity to oxygen. However, the presence of hydrogen shifts the stoichiometric equilibrium so that the equilibrium composition of the fuel with a steam-hydrogen mixture at 10%/mol of H_2 is $UO_{2.000001}$ [10].

At 525°C and 70 bar, oxidation rates of the order of 5 10^{-12} mol.cm2 with an activation energy of 21 kcal.mol-1 were measured by Olander [9]. The oxidation rate with pressure p shows a square root ($rate \propto \sqrt{p}$) or even Langmuir-type ($rate \propto \frac{Ap}{1+Ap}$).

If the presence of hydrogen in the gas mixture delays the oxidation of the fuel rapidly, then the creation of hydrogen by oxidation of the fuel is low compared to that linked to the oxidation of the cladding.

Hydrogen dissolved in the coolant

Hydrogen contained in the coolant is likely to contribute to the hydrogen supply. In the case of French PWRs, the hydrogen content of the primary water is about 30 cm^3/kg. The resulting quantity would be negligible compared to the hydrogen produced by oxidation or radiolysis [8].

4.1.6.2 Hydriding phase

Hydrogen uptake is possible at the external face of the cladding (a well-known phenomenon leading to the formation of the hydride rim) and at the internal face of the cladding.

At the external face, it results from oxidation in the liquid phase by the coolant water. This is the classic hydrogen pick-up by the primary coolant that is often observed for intact rods.

At the internal face of the clad, a primary hydriding is possible for defect-free fuel rods and results from the presence of hydrogen related to moisture or contaminants (moisture or manufacturing process residues).

The secondary hydriding of defective fuel rods is particular because it results from the presence of water in the fuel rod. Different secondary hydriding regimes are possible: expected hydriding due to oxidation (50-500 ppm), accelerated hydriding (thousands of ppm) or massive hydriding (> 10000 ppm).

Massive hydriding causes the formation of secondary defects. This phenomenon is surprising because secondary defects are often observed several meters away from the primary defect. To explain such a distance, there are several hypotheses in the literature. These hypotheses are based on the nature of the gas mixture (state and p_{H2}/p_{H2O} ratio) and on the local state of the internal oxide (not present, reduced or degraded).

Hydrogen uptake due to internal oxidation

Hydrogen is released during oxidation reactions of the fuel or the cladding. Some of the hydrogen released during the oxidation reaction is released in gaseous form into the pellet-clad gap and some contributes to hydrogen uptake by the cladding.

The hydriding kinetics follows the oxidation kinetics and the hydrogen content is proportional to the oxide thickness. This rate depends on the zirconium alloy, it is of the order of 5 to 25% for Zircaloy-4 according to [4]. As a first approximation, the hydrogen uptake would be the same as the one associated with corrosion on the external surface by the coolant, i.e. of the order of 10 to 20%. The rate of hydrogen absorption by the cladding would tend to be established after a phase of total absorption at the beginning of the oxidation reaction [4].

The presence of a zirconium oxide prevents the direct hydriding of the cladding by gas, and for these reasons, zirconia is qualified as a protective layer. This phenomenon is particularly noticeable in the case of hydrogen charging of laboratory samples, where an incubation time is required before beginning of the process. This incubation time is related to the time required for the reduction of the protective oxide.

From the first studies of hydriding, the retarding effect of an oxide layer have been observed (see Fig. 32) and the lacunar diffusion of hydrogen is claimed to explain the temperature dependence. Indeed, hydriding is activated at the same time as the electrical conductivity of ZrO_{2-x}, which is itself governed by the oxygen concentration in the gap. Hydrogen diffusion is therefore related to the oxygen vacancy concentration, which increases from $5.0.10^{-50}$ at 300°C to $2.5.10^{-37}$ at 400°C.

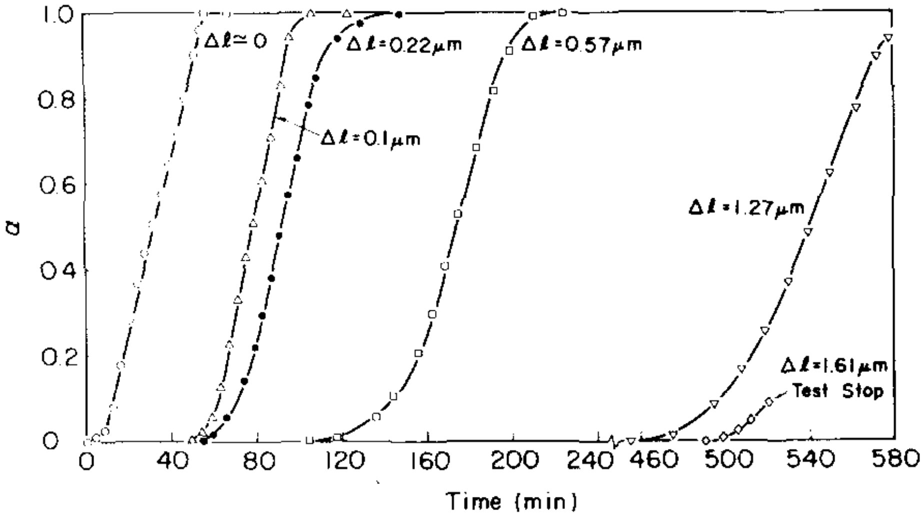

Fig. 32. Evolution of the fraction of hydrogen absorbed by the metal at 400°C as a function of the thickness of the protective oxide film [13]

Massive hydriding

Hydrogen to steam ratio

The steam-hydrogen mixture is charged with hydrogen through various mechanisms. In addition, steam is consumed faster than it is supplied (by vaporization of the coolant near the primary defect) once the internal and external pressures are balanced; this contributes to the hydrogen enrichment of the steam-hydrogen mixture.

When this steam-hydrogen mixture becomes very rich in hydrogen or poor in steam (steam starvation), hydriding takes precedence over cladding oxidation. Above a critical threshold expressed as the ratio of partial pressures p_{H2}/p_{H2O}, a massive hydriding is observed.

Early studies on Zircaloy-2 have shown that the critical ratio is greater when the interface temperature is lower [13], i.e. massive hydriding is more likely where the internal clad temperature is high. The available data on Zircaloy-2 are reported in Table 10.

Table 10. Critical p_{H2}/p_{H2O} ratio for Zircaloy-2

Material	T (°C)	P (bar)	Critical ratio	Ref.
Zircaloy-2	320	1	10^5	Gibby1965
Zircaloy-2	400	1	10^2	Shannon1963
Zircaloy-2	343	1	10^6-10^8	Boyle1958
Zircaloy-2	300	1	10^5	One1978
Zircaloy-2	400	1	10^2	One1978
Crystal-bar Zr	400	1	10^5	KWO97
Zircaloy-2	400	70	2.10^2	KWO99
Zircaloy-2	350	70	$2.5.10^3$	KWO99

These studies on Zircaloy-2 show in most of the cases a linear trend [13][4][14][15][22][23] even if a parabolic evolution has also been reported [16][17]. This evolution is proportional to the contact surface and the reaction seems to be controlled by hydriding front evolution [13]. Activation energies of the order of 70 kJ.mol^{-1} are measured for Zircaloy-2 (16.3 kcal.mol^{-1}[13], 17.2 kcal.mol^{-1}[17]).

As early as 1978, Une et al. proposed a formulation for the fraction α of absorbed hydrogen in the form [13]:

$$\alpha \sim \frac{2kt}{r_{out} - r_{int}} \sim k't, \text{ avec } k[mm.min^{-1}] = 1.5510^3 \exp(-16300/RT)$$

with k the speed of the front, r_{int} and r_{out} respectively the inner and outer radius of the clad and k' the apparent reactivity rate. The authors also show that in the absence of new hydrogen supply, massive hydriding is followed by a delayed hydriding phase and then ends as shown in Fig. 33.

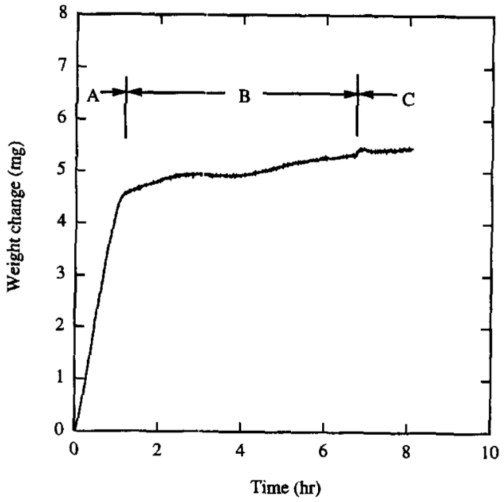

Fig. 33. Hydriding evolution of Zircaloy-2 at 70 bar and 400°C for a steam-hydrogen mixture. A: massive hydriding (p_{H2}/p_{H2O}=10^5), B: delayed hydriding (p_{H2}/p_{H2O}=50) and C end of hydriding (p_{H2}/p_{H2O}=25) [15]

Influence of pressure

The effect of pressure on hydriding has also been studied on Zircaloy-2 for an atmosphere composed of pure hydrogen [14] and a steam-hydrogen mixture [15]. While the critical ratios are of the same order of magnitude, the rate of hydriding is strongly influenced by pressure (see Fig. 34).

Two hydriding modes are distinguished: slow at 10^{-8} mol.cm^{-1}and fast at 10^{-6} mol.cm^{-1}.

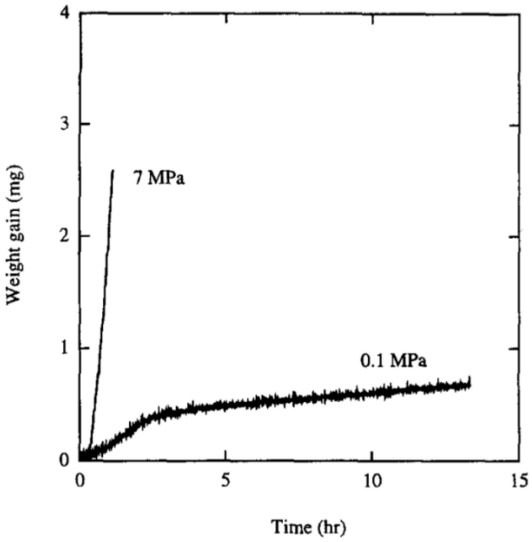

Fig. 34. Influence of pressure on hydriding of zirconium at 400°C in hydrogen atmosphere [14]

Influence of irradiation

The influence of irradiation could justify the critical ratio differences between the analytical experiments and the reactor cases. Evdokimov et al. mentioned that the drastic increase of the vacancies with irradiation could explain the lower ratios observed in reactor. Taking into account the irradiation on the critical ratio $\beta_{critical}$ is proposed through a corrective term taken as the ratio of the temperature-induced K_c and induced by irradiation $\alpha_c\dot{F}$ of defect creation in the oxide:

$$\frac{\beta_{rad}}{\beta_{therm}} = \frac{K_c}{\alpha_c\dot{F}}$$

with $\dot{F}$ the fission rate at the pellet periphery, and α_c a weighting to take into account radiative recombination. The evolution of this corrective term is shown in Fig. 35.

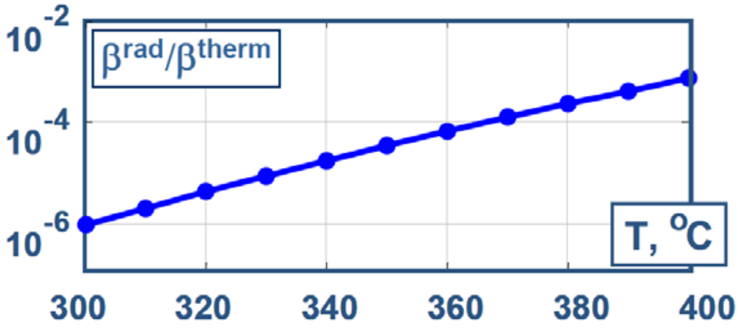

Fig. 35. Evolution of the critical p_{H2}/p_{H2O} ratio with irradiation [20]

Evdokimov et al. propose the following model for the critical ratio:

$$\beta_{critical} = \left({}^{P_{H_2}}\!/_{P_{H_2O}}\right)_{critical} = 6\ 10^{-16}\exp^{26670/T}$$

More recent studies have also been carried out on Zircaloy-4 and ZIRLO between 300 and 500°C [22]. A dependence of the activation energies on the alloy is noticed (see Fig. 36):

- $k_{Zircaloy-2}$=1.1 10^7 exp(87.0/RT),
- $k_{Zircaloy-4}$ =6.9 10^7 exp(100/RT),

- k $_{ZIRLO}$=1.5 10^6 exp(75.3/RT)

with k in mg/dm^2 and Q in kJ/mol.

The authors confirm a linear trend after an incubation period due to the oxide layer. However, below 400°C, a deviation from the linear law is observed and is attributed to the slow diffusion of hydrogen into the hydride layer formed.

It is notable that, without radial temperature gradient in the cladding (as in a reactor), the authors still observe sunburst type defects.

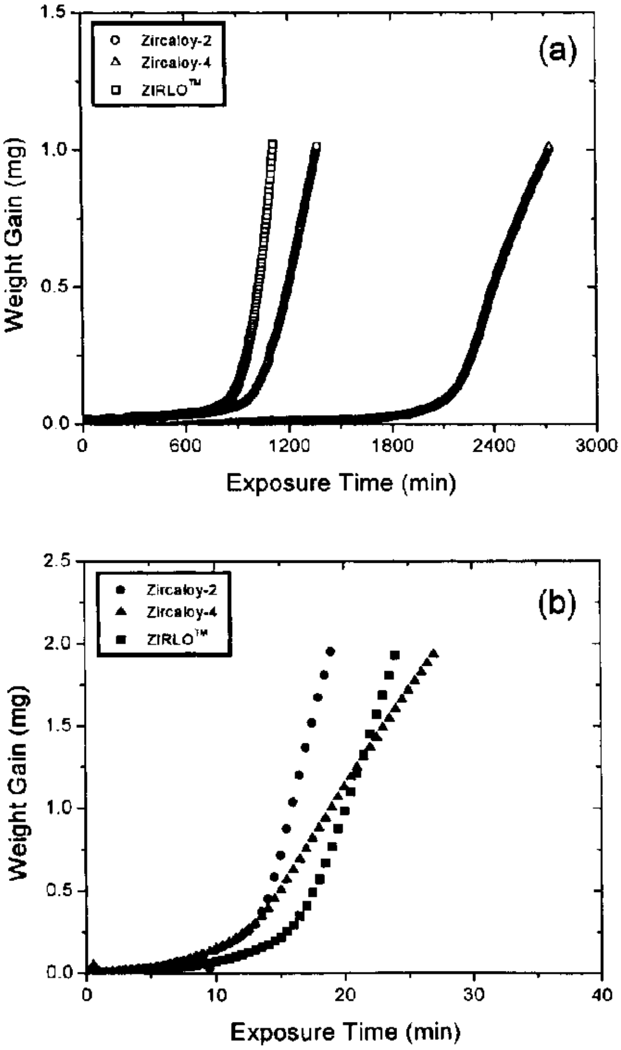

Fig. 36. Mass gain evolution for Zircaloy-2, Zircaloy-4 and ZIRLO samples at 350°C (left) and 400°C(right) [22]

Influence of the power profile

According to [21], the power profile affects the distribution of the hydrogen-oxygen ratio in the fuel rod. Reactor operating is often performed with a negative axial offset in order to have a power maximum in the lower part of the core. In this case, the hydrogen-to-steam ratio favorable to massive hydriding could be reached at a lower value than in the case of a uniform axial power profile. This is illustrated in Fig. 37.

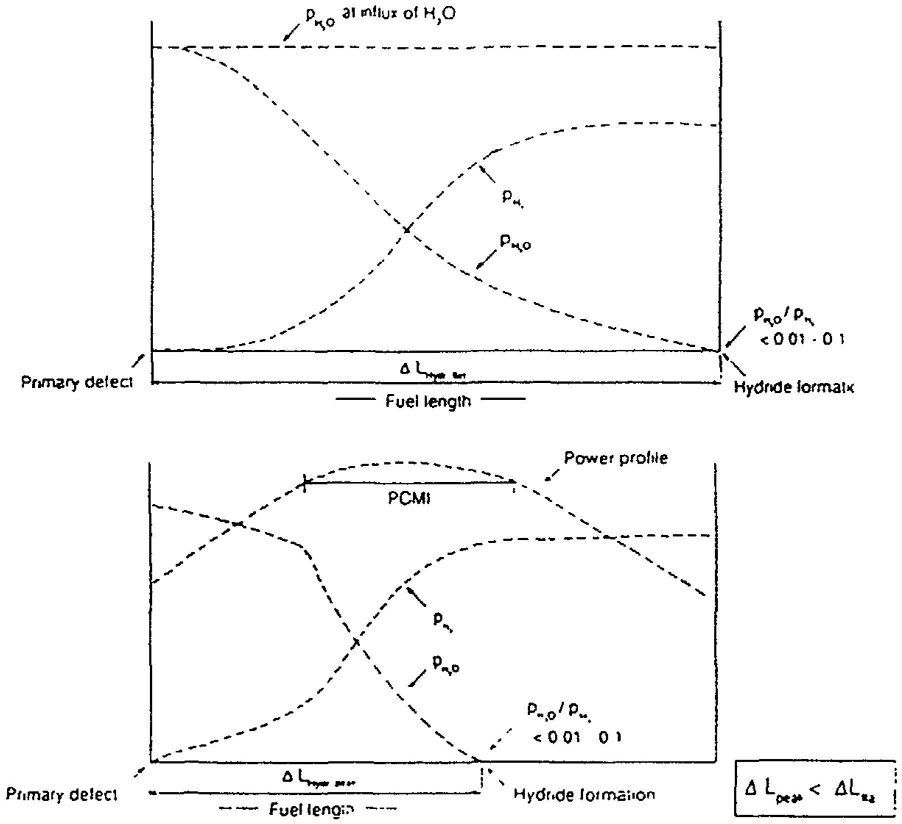

Fig. 37. Influence of axial power profile on hydrogen-steam partial pressures [21]]

Latest studies on Zircaloy-4 (Lee et al. @KAERI)

A recent study is dedicated to Zircaloy-4 and explores the hydrogen uptake between 400-500°C and for different steam-hydrogen mixtures (10^5, 10^4, $10^3$and 5 10^2) [23]. Even if temperatures below 400°C are not explored, this study discuss the critical aspect of this ratio. Indeed, and as shown in Fig. 38, hydriding is dominant in the steam starvation condition (ratio beyond 10^4). However, massive hydriding is triggered at all temperatures for a given ratio. Hydriding is only delayed and the hydriding rate decreases continuously with temperature (see Fig. 39).

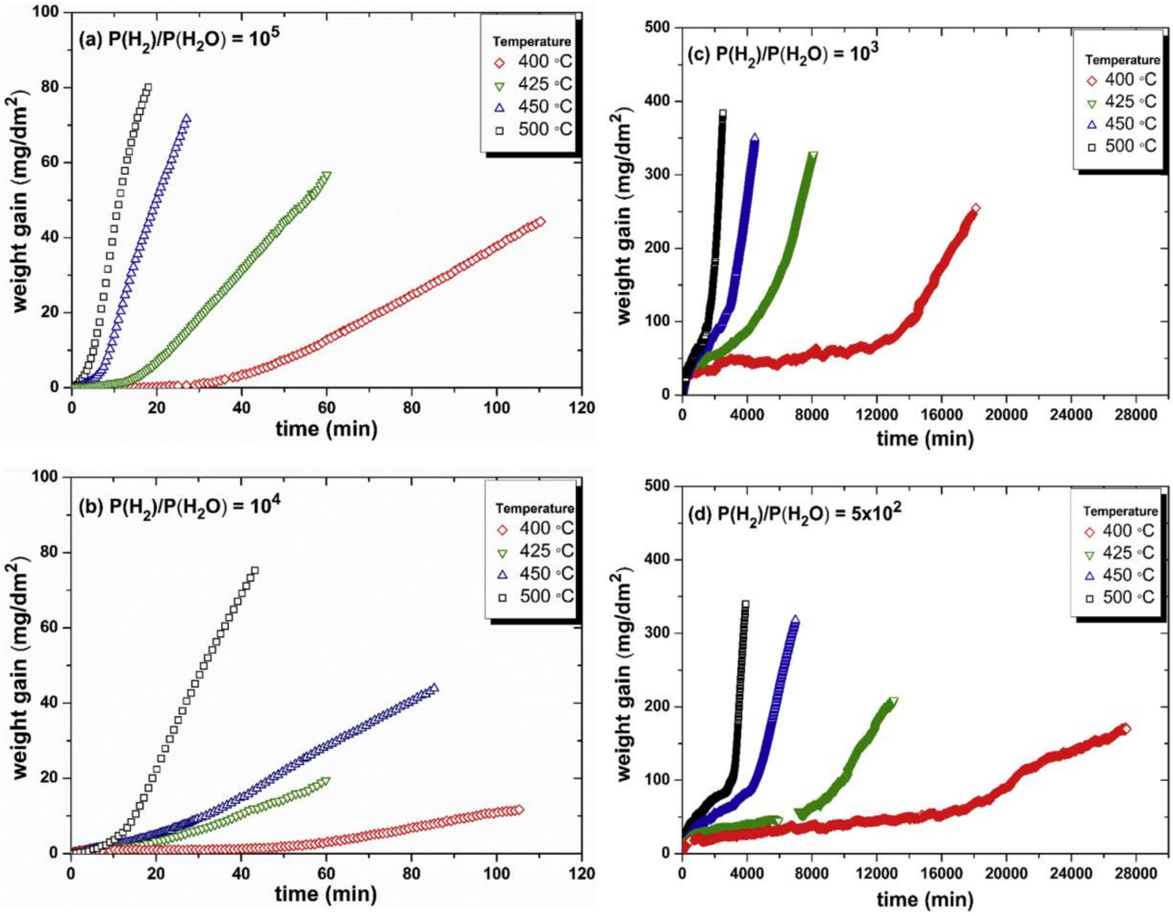

Fig. 38. Evolution of the mass gain of a Zircaloy-4 tube in a steam-hydrogen mixture and at different temperatures. (a) $p_{H2}/p_{H2O}=10^5$, (b) $p_{H2}/p_{H2O}=10^4$, (c) $p_{H2}/p_{H2O}=10^3$, (d) $p_{H2}/p_{H2O}=5\ 10^2$[23]

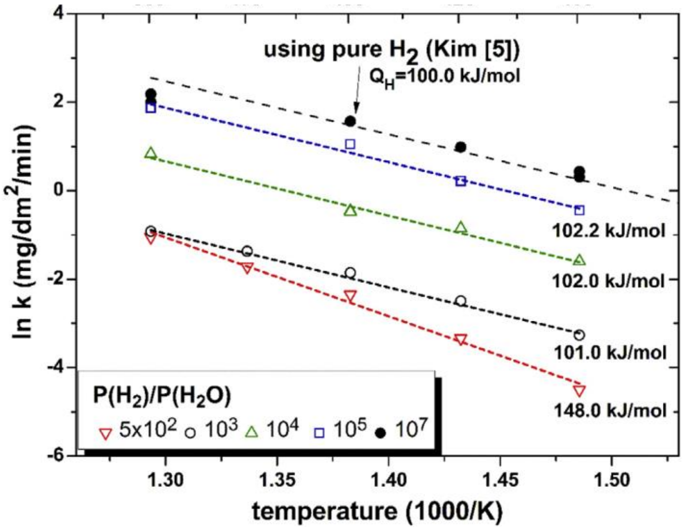

Fig. 39. Activation energies derived from the massive hydriding reaction rate of Zircaloy-4 [23]

For ratios lower than 10^4, the authors observe a coexistence of both hydriding and oxidation. Oxidation under these conditions is accelerated by the presence of hydrogen and follows a cubic law (see Fig. 40). This regime induces

an accelerated hydriding. These observations are consistent with the fast (10^{-6} mol.cm^{-1}) and slow (10^{-8} mol.cm^{-1}) regimes observed by [14][15].
Thus, the mass gain related to hydriding ΔW_H and oxidation ΔW_{ox} can be expressed as:

$$\Delta W_H = k_H t$$

$$k_H = k_H^0 \exp\left(-\frac{Q_H}{RT}\right)$$

$$\Delta W_{ox}^3 = k_{ox} t$$

$$k_{ox} = k_{ox}^0 \exp\left(-\frac{Q_{ox}}{RT}\right)$$

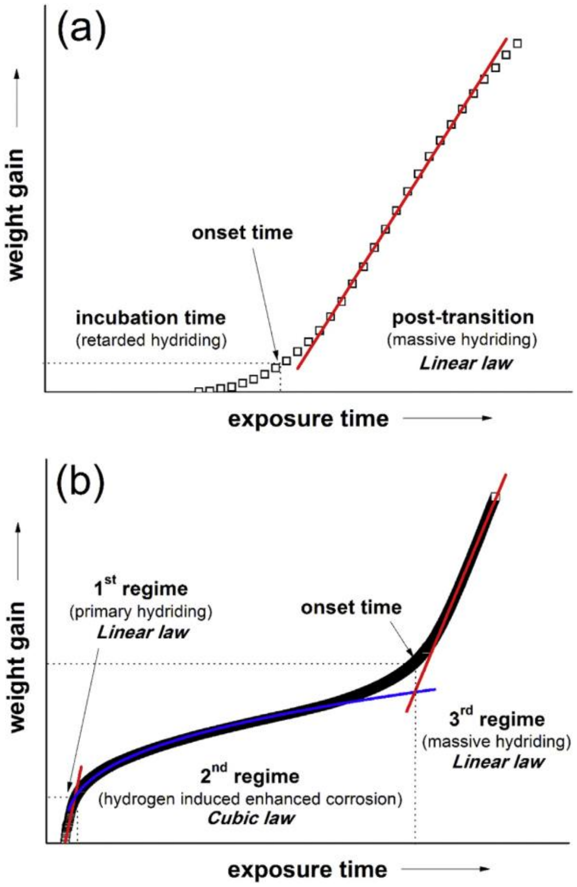

Fig. 40. Typical hydriding evolution of Zircaloy-4 in a hydrogen-rich environment $p_{H2}/p_{H2O}>10^4$(a) and hydrogen-steam mixture $p_{H2}/p_{H2O}<10^4$(b) [23]

Onset of the hydrogen uptake and influence of the internal oxide

Hydrogen enrichment is a necessary condition for secondary hydriding but is not sufficient to explain the incubation time, the onset of the reaction and the distance to the primary defect.

Several hypotheses can be found in the literature:

- The steam content is lower further away from the primary defect. From a certain distance, the mixture is sufficiently rich in hydrogen. It is commonly accepted;
- The oxide thickness is thinner further away from the primary defect. From a certain distance, the oxide thickness is too thin to be protective [4][22];
- The water is in liquid state at the bottom of the rod and is in steam state only from a certain distance. Massive hydriding is only possible in the gas phase, i.e. from the axial altitude where the internal temperature of the clad is higher than the saturation temperature of the water;

- Above a certain thickness, the zirconium oxide cracks radially and creates a direct hydrogen diffusion path to the cladding. See Lee et al. [23].

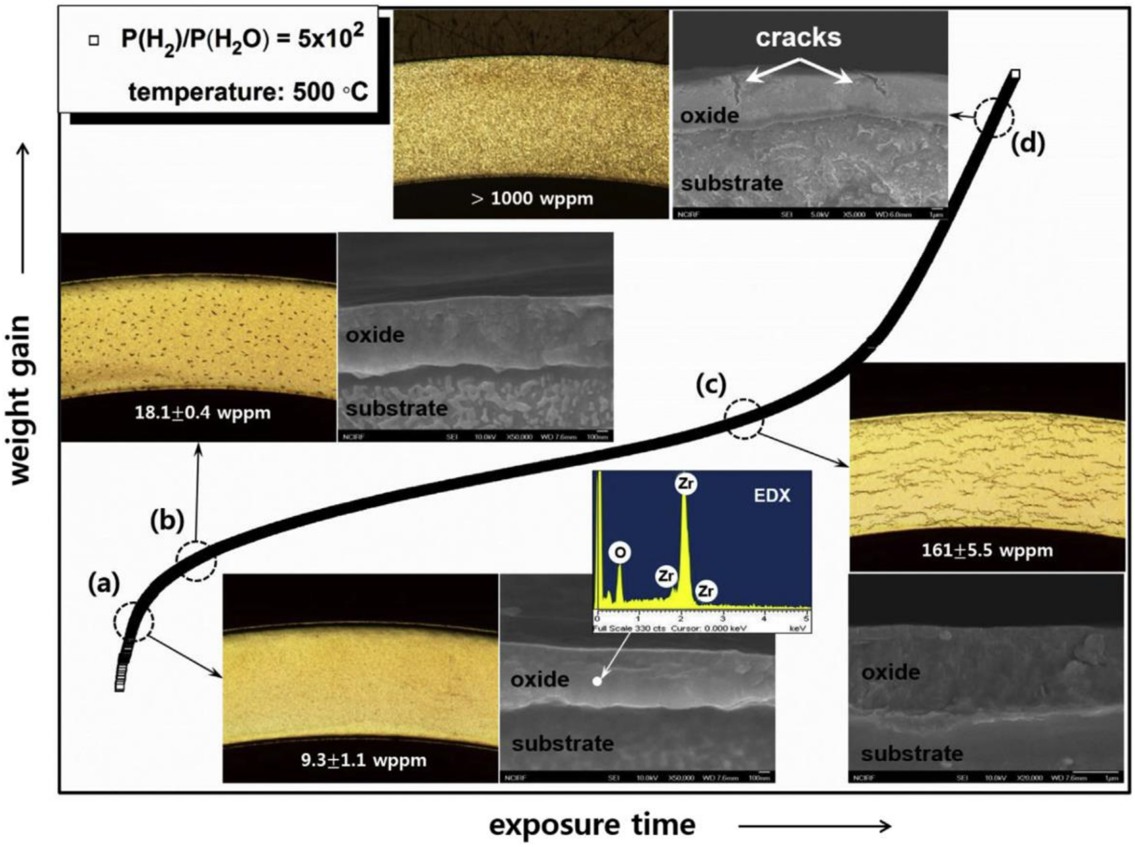

Fig. 41. Illustration of oxide cracking as a precursor to massive hydriding. Metallography and revelation of hydrides during hydriding on Zircaloy-4 [23]

- At a given axial altitude, the gap closes and there is no more possibility of water supply. Above the closed gap zone, the steam-hydrogen mixture evolves towards a steam depletion. It is not a common assumption [9]. It does not explain the occurrence of primary and secondary defects for 3rd cycle fuel rods for which the gap is closed;
- The zirconium oxide is attacked in a hydrogen reducing atmosphere, it disappears faster with high temperature, thus at the top of the rod. No data available;
- The oxide is metastable and disappears in favour of the Zr(O) phase, but this process is limited by the diffusion rate of oxygen in the zirconium. No data available;
- Irradiation and fission product attack make the internal oxide highly defective and therefore permeable to hydrogen. The effect of irradiation on the initiation of secondary hydriding must be linked to the issue of oxide integrity. No data available.

4.1.6.3 Damage phase

Hydrogen diffusion and precipitation

Once massive hydriding conditions are reached, hydrogen is rapidly absorbed by the cladding. This gaseous absorption is much faster than the diffusion of hydrogen into the zirconium. High hydrogen contents are therefore found at the inner side of the clad.

As the solubility limit of hydrogen in zirconium is low at operating temperature, hydrogen precipitates and forms hydrides. Hydride accumulation zones form blister on the inner side of the clad.

Perforation mechanism

A secondary hydriding zone is characterized by very high local hydrogen content: the hydrogen uptake can reach several thousand ppm [30], in particular for blister-type defects.

,

This sunburst evolution scenario is illustrated in Fig. 42.
The results of the HALDEN IFA-600 tests carried out under REB conditions (70 bar and 250°C) show that blisters can form very quickly (over a period of 48 hours) after the steam has entered.

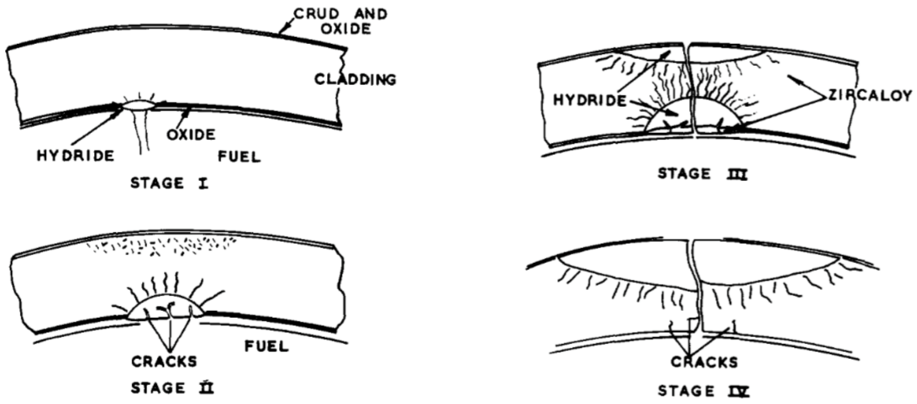

Fig. 42. Illustration of formation mechanism of a perforating sunburst secondary defect type [24]

4.1.7 Integral test

The few integral tests referenced in the literature concern Zircaloy-2 to study BWRs representative secondary hydriding. The secondary hydriding is relatively well reproduced but the phenomenon is much faster than in the reactor.

4.1.7.1 DEFEX (Studsvik)

About twenty tests were conducted in the R2 reactor with the objective of studying the secondary hydriding after simulation of a primary fault. Zircaloy-2 cladding was studied, with different types of liners.
After feasibility tests (DEF-I and DEF-2), 11 experiments were carried out on unirradiated fuel between 1993 and 1995 in the framework of the DEFEX program. The primary defect is simulated by the prior presence of a quantity of water in a dedicated plenum above the rod [26][32].
In 1996, two additional experiments were conducted on pre-irradiated fuel at 25 GWd/tU with a different concept for the primary defect simulation: the water was contained in a fusible ampoule allowing the steam to be released after a certain time [27][32](see Fig. 43).

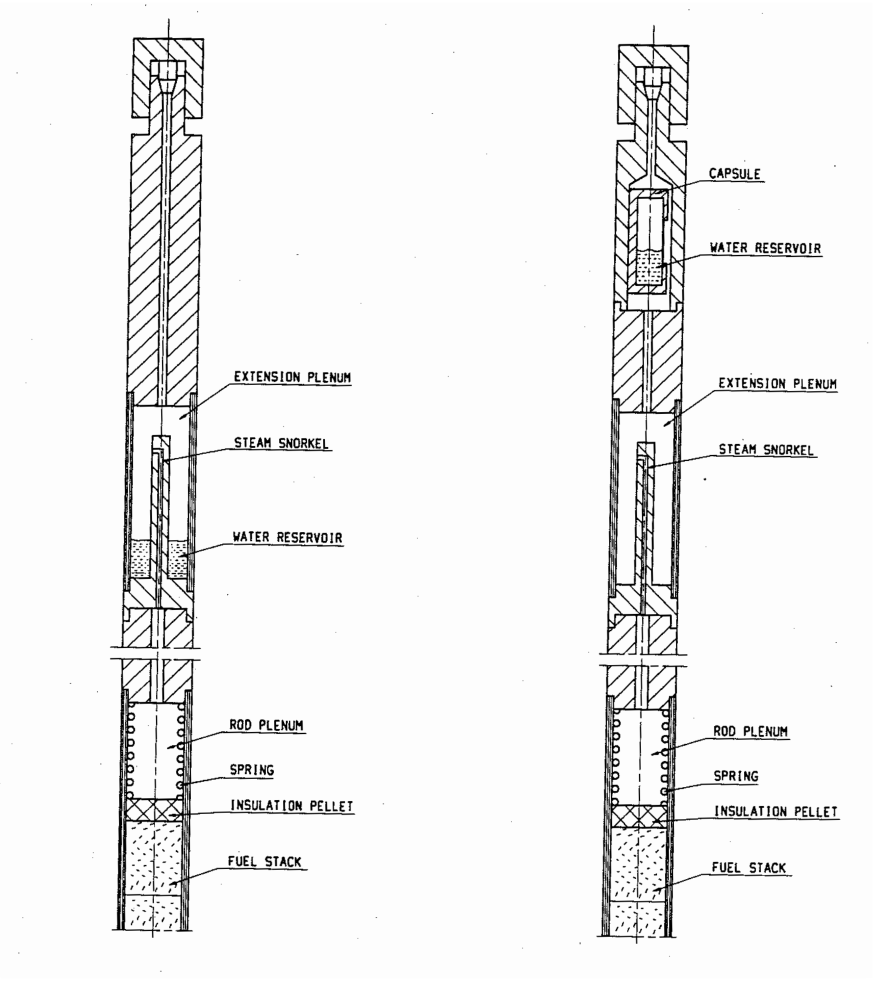

Fig. 43. Experimental devices for the simulation of a primary defect. Design principle for the DEFEX program (left) and capsule concept of the DEFEX II DEMO program (right)

In the DEFEX program, four rods had an initial clearance of 0.15 µm and different types of cladding. These tests shown significant hydriding for powers of 40 and 50 kW/m. Failure was relatively rapid, from 76 h to 216 h following the occurrence of the primary defect. The rod embrittlement was deduced from the total rod elongation that shown rapid evolutions attributed to hydriding, quite different from rod elongation induced by the contribution of irradiation alone.

The two DEFEX II DEMO tests were conducted at 35 and 40 kW/m respectively. The first rod cracked at the bottom weld and the crack propagated in the circumferential direction. The second rod developed several cracks with the origin of high local hydride concentrations. SEM analysis shows brittle fracture surfaces and no evidence of ductility. The cracks propagated both radially and axially. This second test is considered representative of a reactor case.

4.1.7.2 HALDEN

The IFA-600 and IFA-622 tests were conducted in Halden in the late 1990s as part of the NFIR-III program. The IFA-631, IF-684 and IFA-742 tests were conducted by a collaboration of industrial actors in the framework of the SFDP (Secondary Fuel Degradation Program) summarized in [28].

IFA-600

The objective of these in pile tests is to follow the hydriding evolution of a 1 m Zircaloy-2 cladding section following a simulated flow-controlled water ingress. The ingress is planned after an irradiation leading to a burnup of 10 GWd/tU. The test is terminated by a power ramp leading to a mechanical PCI failure. Conditions are representative of a BWR (70 bar and 250°C). The test matrix is designed to study the influence of the pellet-clad gap (100-200 µm) and the influence of a liner in the inner side of the clad.

Despite the uncontrolled entry of steam during the initial irradiation phase, monitoring of the fuel temperature and internal pressure of the rods showed that:

- The entry of steam and the rapid consumption of the steam by the oxidation reaction of the cladding on the inner side - the decrease of the internal pressure is proportional to the rate of hydrogen appearance. This confirms the important part of oxidation kinetics as a source of hydrogen;
- The influence of the material: the oxidation kinetics of Zircaloy-2 with liner being faster than the kinetics of Zircaloy-2 without liner;
- The influence of the gap: the evolution was faster for the biggest gap;
- Blisters can form very quickly, in 48 hours after steam entry under certain conditions;
- The thickness of the zirconia on the inner side is about 4 to 12 µm.

IFA-622

These tests follow the IFA-600 campaign. The experiments seem to be representative of the reactor case except that the mechanisms are much faster, especially in the establishment of the maximum hydrogen content.

The conclusions drawn from the online monitoring and destructive examinations are:

- Water ingress and vaporization;
- Progression of steam in the clad and oxidation of the liner;
- Absorption of hydrogen in regions far from the defect;
- Embrittlement and crack propagation in the hydrided regions.

IFA-631

The IFA-631 campaign demonstrated the feasibility of commercial BWRs representative test with respect to the secondary hydriding phenomenon. These tests are dedicated to the study of the mechanisms of secondary hydriding in normal operation and in particular the influence of the size of the pellet-clad gap. The mechanical loading by PCI is not studied here and no power ramp is applied. The role of a pre-oxidized ZrSn liner on the inner face is also tested.

After a first basic irradiation period of 144 days corresponding to a burnup of 5.3 GWd/tU, the primary defect is simulated using a valve allowing water to enter at the top end cap. A new irradiation period of 118 days at 270 W/cm is performed before unloading and out of pile characterization.

During these tests, the temperature is monitored with thermocouples at the top and bottom of the test rods. The entry of water simulating the primary defect causes an increase in temperature in the upper part of the rod and a decrease in the lower part of the rod. This decrease in the lower part of the rod is attributed to the presence of hydrogen, which is more conductive than the steam or the filling gases.

These tests showed:

- Very high local hydrogen concentrations far from the water entry point, typical of secondary hydriding;
- Severe damage to all fuel rods (sometimes with breakage during handling);
- No influence of the pre-oxidized ZrSn liner;
- No influence of the gap size (110 µm vs 170 µm).

IFA-684

The IFA-684 campaign is dedicated to study how to mitigate secondary hydriding. An operating action is envisaged and consists in shutting down the reactor just after the occurrence of the primary defect. The other solutions are material evolutions: testing of different types of alloys or liners and testing of the addition of carbon monoxide in the filling gases to capture the hydrogen.

The base irradiation is similar to IFA-631 and the post primary defect period is 32 days at 280 W/cm.

The conclusions of these tests are:

- No influence of the type of cladding or the type of liner;
- No effect of CO in the composition of the filling gas;
- Rapid severe hydriding (within a month after the primary defect);

- A shutdown of the reactor to allow full filling of the rod with water prevents the development of secondary hydriding.

IFA-742

The IFA-742 campaign is dedicated to the study of hydrogen uptake kinetics and the influence of power on the development of secondary hydriding.

A base irradiation of about 100 days is conducted for different test rods whose enrichment allows to reach powers of 180, 260 and 340 W/cm. The irradiation times after simulation of the primary defect are short: 3 days at 180 W/cm; 3 days and 12 hours at 260 W/cm; 12 hours, 3 hours and 1 hour at 340 W/cm.

The observations of the IFA-742 campaign are:

- All tests led to severe secondary hydriding (presence of blister and perforation);
- High hydrogen levels located at 25 cm from the bottom cap for 1.2 m rods with water entry at the top;
- Perforated rods have the highest hydrogen content;
- Hydrogen content in the order of 1500-2000 ppm reached in 12 hours at 340 W/cm;
- Correlation between the duration of post primary defect irradiation and the degree of hydriding;
- No significant influence of the irradiation power.

4.2 Simulation of secondary hydriding with SHOWBIZ

4.2.1 Simulation scenario

The following scenario has been chosen taking into account the constraints of the software architecture:

- Water ingress: "valve" model with refrigerant pressure, a primary defect section as parameter. This induces a flow of water in/out of the mesh affected by the primary defect. This ingress can be totally or partially closed after internal/external pressure equilibrium or left open to simulate new water ingresses when the pressure gets lower due to steam or hydrogen consumption.

- Gaseous species in the pellet-clad gap: the gaseous species are steam, hydrogen and the total of the other gases (filling gases + fission gas without distinction to allow the calculation of the internal pressure of the rod).

- Steam-hydrogen gas transport: advection-diffusion-creation model with gas diffusion model based on binary coefficients:

$$\frac{\partial c_i}{\partial t} = \nabla.(D_i \nabla c_i) - \nabla.(\boldsymbol{v} c_i) + Q_i(t)$$

- Axial gas propagation: Darcy-type gas transfer model with porosity and permeability coefficients for all gaseous species. These coefficients must allow to simulate both an equivalent gap thickness (if open) or a permeability in the case of a closed fuel-clad gap.

- Internal oxidation: correlation model with a cubic law and coefficient from Lee et al:

$$\Delta W_{ox}^3 = k_{ox} t\,, \qquad k_{ox} = k_{ox}^0 \exp\left(-\frac{Q_{ox}}{RT}\right)$$

- The steam is consumed until it is exhausted, the hydrogen is distributed between the channel mesh and the cladding mesh with a pickup coefficient to take into account the hydrogen uptake of the metal.

- Hydrogen creation: sources of hydrogen creation other than from internal oxidation are neglected.

- Massive hydriding: correlation model with a linear law and coefficients from the literature. A further condition incorporates a dependency on the ratio $\left(\frac{p_{H2}}{p_{H20}}\right)$:

$$\left(\frac{p_{H2}}{p_{H20}}\right) > \beta = \left(\frac{p_{H2}}{p_{H20}}\right)_{critical}$$

- Degradation of the inner oxide layer: reduction of the oxide by diffusion of native oxygen, possibility of critical thickness or oxygen content. It is not foreseen to implement the possibility of inner skin cracking nor random defects.

- State of water: activation of the models conditioned by the temperature (above the saturation temperature of water). The presence of liquid water instead of steam is not considered.

- Diffusion and precipitation of hydrogen in the clad with pre-existing software models.

4.2.2 FUEL+SHOWBIZ architecture

In the frame of the FUEL+ platform, IRSN is developing a set of computer codes devoted to the simulation of fuel behaviour all along the fuel cycle for normal and accidental conditions. This platform regroups a pre-irradiation software FIRST for normal operation and transient conditions – transport and storage accidents, SCANAIR devoted to reactivity insertion accidents, DRACCAR dedicated to loss-of-coolant accidents and SHOWBIZ, a multiphysics software which focuses the weakening effect of species H and O on the cladding.

The SHOWBIZ latest version 2022 [36] proposes a multiphysics modelling of the fuel cladding taking into account both oxidation and hydriding together with thermal conduction and visco-elastic mechanical behaviour. Finite Volume Method is used for solving the heat transfert and the H and O transport within a 3D meshing of the fuel cladding. Finite Element Method is used for solving the mechanical deformation of the cladding geometry.

SHOWBIZ architecture is based on a modular design, the main physical phenomena being handled in separate modules. Each module can be executed either independently or coupled to other modules which then facilitates the study of mutual dependencies for coupled physical models. The modules are coupled explicitly using a sequential execution with implicit scheme resolution and loop parallelization remaining internal to a module.

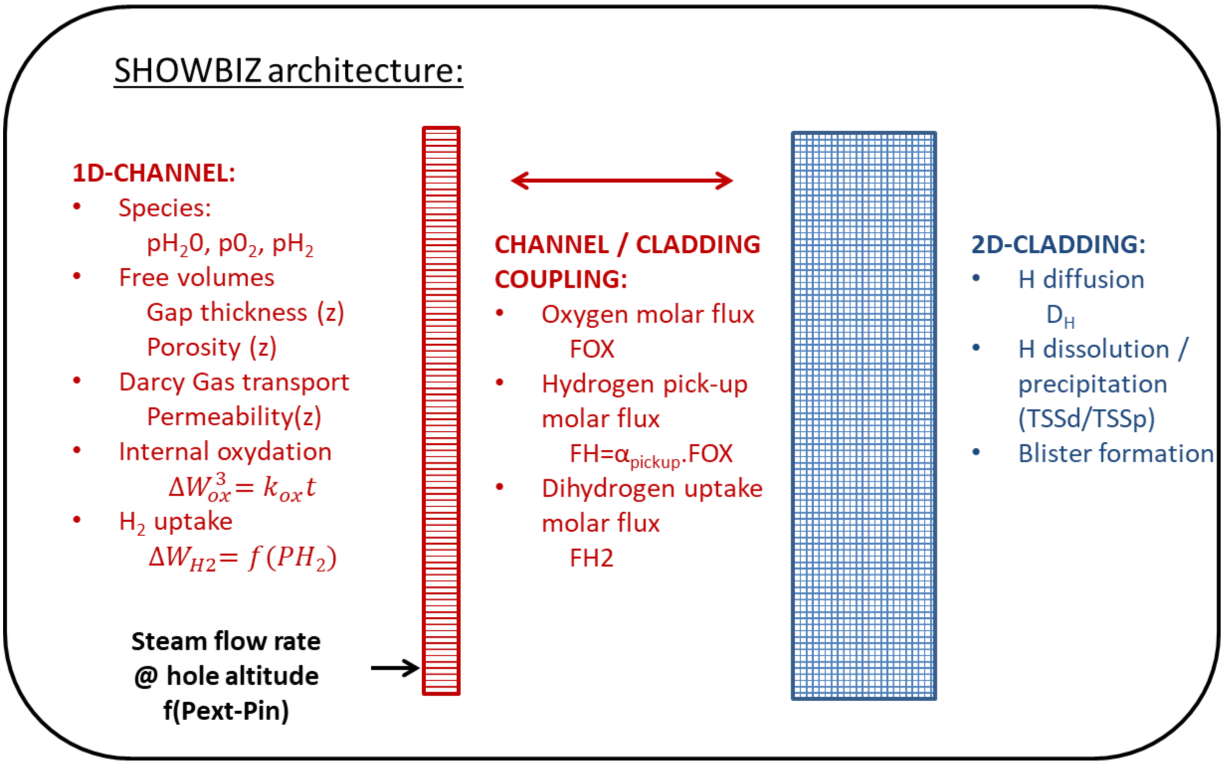

Fig. 44. Illustration of the SHOWBIZ software design for secondary hydriding modeling.

The specific module CHANNEL has been developed for the modeling of secondary hydriding, which is the main objective of Task 4.3 of the R2CA project. The aim of this module is to simulate the gas distribution in the internal free volumes of the fuel rod and their interaction with the internal side of the cladding. It consists of a one-dimensional channel geometry where steam inlet and multi gaseous species consumption/creation, transport and diffusion are solved according to the mass concervation and the reaction kinetics as boundary conditions. The coupling of the CHANNEL module with the H and O concentration in the 3D cladding geometry has been achieved through H and O molar flux boundary conditions at the internal faces of the cladding (see Fig. 44).

4.2.3 Physical models of the CHANNEL module

The CHANNEL module is a one-dimensional finite volume model with the same Nz axial discretization of the facing 3D cladding regular meshing.

Each Nz domain defines a control volume with axial boundaries in between and one axisymetrical radial boundary with the cladding. Nz-1 axial control volume boundaries are thus considered, the first and the last being closed with a no flux condition across them.

Three gaseous species are considered: H_2O, H_2 or He. For a control volume i at time (t+Δt), the molar quantities conservation leads to the following system:

$$\frac{d}{dt}n^i_{H2O} = \frac{n^i_{H2O}(t+\Delta t)-n^i_{H2O}(t)}{\Delta t} = F^{darcy,i-1}_{H2O} + F^{fick,i-1}_{H2O} - F^{darcy,i}_{H2O} - F^{fick,i}_{H2O} - Q^i_{ox} + Q^{ihole}_{H2O}$$

$$\frac{d}{dt}n^i_{H2} = \frac{n^i_{H2}(t+\Delta t)-n^i_{H2}(t)}{\Delta t} = F^{darcy,i-1}_{H2} + F^{fick,i-1}_{H2} - F^{darcy,i}_{H2} - F^{fick,i}_{H2} + (1-\varepsilon)Q^i_{ox} - Q^i_{H2}$$

$$\frac{d}{dt}n^i_{He} = \frac{n^i_{He}(t+\Delta t)-n^i_{He}(t)}{\Delta t} = F^{darcy,i-1}_{He} + F^{fick,i-1}_{He} - F^{darcy,i}_{He} - F^{fick,i}_{He}$$

with:

- $\mathrm{n}_{\mathrm{gas}}^{\mathrm{i}}$ the molar quantity of gas in the mesh i,
- $\Delta\,\mathrm{t}$ the time step,
- $\mathrm{F}_{\mathrm{gas}}^{\mathrm{darcy,i-1}}$ the advective flux through the face $i-1$ connecting the $i-1$ and i meshes,
- $\mathrm{F}_{\mathrm{gas}}^{\mathrm{darcy,i}}$ the advective flux through the face i connecting the i and $i+1$ meshes.
- $\mathrm{F}_{\mathrm{gas}}^{\mathrm{fick,i-1}}$ the diffusive flux through the face $i-1$ connecting the $i-1$ and $i-1$ meshes,
- $\mathrm{F}_{\mathrm{gas}}^{\mathrm{fick,i}}$ the diffusive flux through the face i connecting the i and $i+1$ meshes.
- $\mathrm{Q}_{\mathrm{ox}}^{\mathrm{i}}$, the steam sink term due to oxidation of the cladding, thus steam leaves the channel,
- $\mathrm{Q}_{\mathrm{H2O}}^{\mathrm{ihole}}$, the steam source term in the channel through the primary defect localized at the $ihole$ mesh.
- ε the hydrogen pickup coefficient, $\varepsilon.\,\mathrm{Q}_{\mathrm{ox}}^{\mathrm{i}}$ the hydrogen pickup entering the cladding, $(1-\varepsilon)\mathrm{Q}_{\mathrm{ox}}^{\mathrm{i}}$ is therefore the H2 source term due to oxidation of the cladding,
- $\mathrm{Q}_{\mathrm{H2}}^{\mathrm{i}}$ the H2 sink term due to the hydriding of the cladding.

This system is solved at each time step with a Newton-Raphson iterative method.

4.2.3.1 *Darcy advective molar flow*

This section details the gas flow equations based on the Darcy law. Here the gravitationnal forces are neglected and the flux is a function of a pressure drop over a given distance.
Let i be the face that connects the mesh i and $i+1$, the gas face velocity vi then expresses as:

$$v = \frac{(P^i - P^{i+1})}{R_h}$$

where R_h is the global friction loss of the two half meshes i and $i+1$ and writes:

$$R_h = \frac{R_h^i}{2} + \frac{R_h^{i+1}}{2} = \frac{1}{2}\left(\frac{\eta^i}{k^i}\Delta Z^i + \frac{\eta^{i+1}}{k^{i+1}}\Delta Z^{i+1}\right)$$

with:

- k^{i+1} and k^i the permeability coefficients of meshes $i+1$ and i in m^2,
- η^{i+1} and $\eta^i$the gas dynamic viscosity of meshes $i+1$ and i in kg/(m.s),
- ΔZ^{i+1} and ΔZ^i the height of the $i+1$ and i meshes, respectively, in the axial direction.

Depending on the velocity sign, the molar flux of gas crossing this face writes:

$$F_{gas}^{darcy,i} = \frac{Av^i n_{gas}^i}{V^i} \text{ for } v^i > 0,\; F_{gas}^{darcy,i} = \frac{Av^i n_{gas}^{i+1}}{V^{i+1}} \text{ for } v^i < 0$$

with:

- n_{gas}^i and n_{gas}^{i+1} , the amount of molar quantities of gas inside the mesh i and $i+1$,
- V^i and V^{i+1} the total volume of gases in meshes $i+1$ and i in m^3,

- A the section area of the fuel rod perpendicular to the flow.

Note that the volume of gases in mesh i depends on the mesh porosity Φ^i such as:

$$V^i = \Phi^i V^i_{geom}$$

with V^i_{geom}, the geometrical volume of the ith mesh.

4.2.3.2 Gas diffusive molar flow

The gas flow induced by diffusion crossing the face i writes for each gas:

$$F^{fick,i}_{gas} = \frac{2S^i}{\frac{\Delta Z^{i+1}}{D^{i+1}_{gas}} + \frac{\Delta Z^i}{D^i_{gas}}} \left(\frac{P^{i+1}_{gas}}{P^{i+1}} + \frac{P^i_{gas}}{P^i}\right)$$

with:

- $S^i = (V^i + V^{i+1})/(\Delta Z^i + \Delta Z^{i+1})$ the crossing area of face i with V^i and V^{i+1}, the volume of gases in the $i+1$ and i meshes, respectively,
- D^i_{gas} and D^{i+1}_{gas} the diffusivity of gas in mesh i and $i+1$ with unit m^2/s,
- ΔZ^{i+1} and ΔZ^i the height of the $i+1$ and i meshes, respectively, in the axial direction.

4.2.3.3 Inlet steam flow

Let us consider the mesh ih where the hole is located, the steam velocity v entering the channel is related to the pressure drop as follow:

$$v = \frac{k^{ih}}{\eta} \frac{(P_{ext} - P^{ih})}{r^{ih}_c}$$

where:

- P_{ext} is the external pressure,
- P^{ih} is the pressure inside the channel in the mesh ih where the hole is located,
- r^{ih}_c is the external cladding radius at the mesh ih, the distance between the cladding surface and the center of the fuel rod,
- k^{ih} is the permeability coefficient of the mesh ih,
- η is the dynamic viscosity of the entering steam.

The molar flow of the steam on this mesh, Q^{ih}_{H2O}, then writes:

$$Q^{ih}_{H2O} = \frac{\rho S_h v}{MM_{H2O}} = \frac{\rho k^{ih} S_h}{\eta MM_{H2O}} \frac{(P_{ext} - P^{ih})}{r^{ih}_c}$$

with

- MM_{H2O} the molar mass of H_2O in kg/mol,
- ρ the density of the steam that depends on the external pressure P_{ext},
- S_h the hole geometry.

4.2.3.4 Internal oxidation

The oxidation molar flow at the mesh i writes:

$$Q_{ox}^{i} = \tau_{H2O}^{i} 2\pi r^{i} \Delta Z^{i} P_{H2O}^{i}$$

with:

- τ_{H2O}^{i} the oxidation rate in mesh i,
- $P_{H2O}^{i}$the partial pressure of gas H_2O in mesh i,
- r^{i} the internal radius of the cladding at mesh i,
- ΔZ^{i} the height of mesh i in the axial direction.

The oxidation rate τ_{H2O}^{i} is calculated from a cubic weight gain correlation with time and an Arrhenius temperature dependency. The pre-exponential factor k_{ox}^{0} and the activation energy E_{ox} values are taken from the work of Lee *et al.*[23]:

$$\Delta W_{ox}^{3} = k_{ox} t\,, \qquad k_{ox} = k_{ox}^{0} exp\,(-\frac{\mathrm{E}_{ox}}{RT})$$

4.2.3.5 Hydriding from dihydrogen

The hydriding rate is considered constant for each time step. The hydriding molar flow at the mesh i is given by

$$Q_{H2}^{i} = \tau_{H2}^{i} 2\pi r^{i} \Delta Z^{i} P_{H2}^{i}$$

with

- τ_{H2}^{i} the hydriding rate in mesh i,
- P_{H2}^{i} the partial pressure of gas H_2 in mesh i,
- r^{i} the radial coordinate of mesh i,
- ΔZ^{i} the height of mesh i in the axial direction.

The hydriding rate depends on the dihydrogen partial pressure and has been established from the EK data (see §4.2.4). A condition depending on the partial pressure ratio $\frac{P_{H2}^{i}}{P_{H2O}^{i}}$ has also been implemented where the hydriding rate equals zero if the following condition is not satisfied:

- $\left(\frac{p_{H2}}{p_{H2O}}\right) > \beta = \left(\frac{p_{H2}}{p_{H2O}}\right)_{critical}$

4.2.4 Hydriding rate from EK experiments

In the frame of the R2CA T4.3, EK performed hydrogen uptake measurements in order to overcome the lack of data at temperatures under operating conditions [35]. The investigated cladding materials were E110G and Zircaloy-4 at 300, 330, 370 and 400°C. In the following, we focus on Zircaloy-4 data to determine a hydriding rate correlation from the hydrogen pressure drop in the experimental chamber.

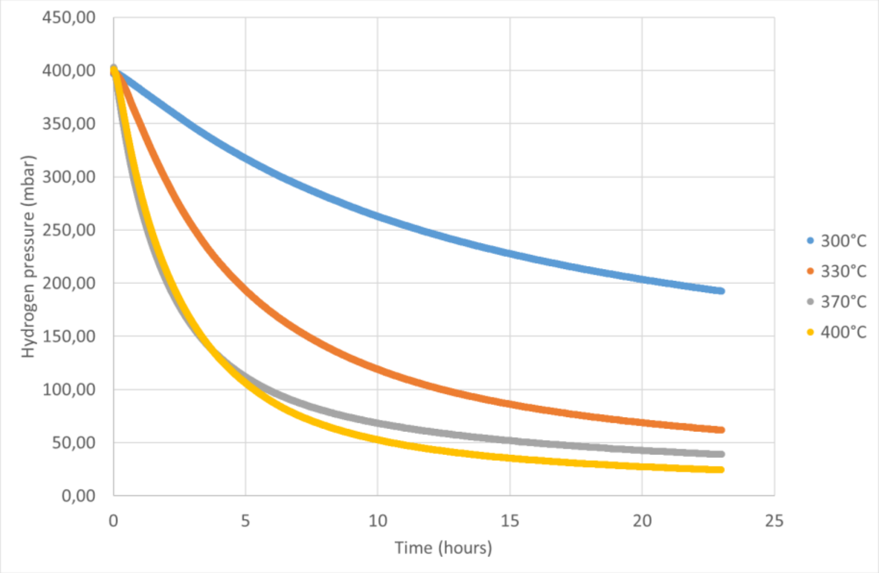

Fig. 45. Dihydrogen pressure evolution with time in the charging chamber for Zircaloy-4 samples [34]

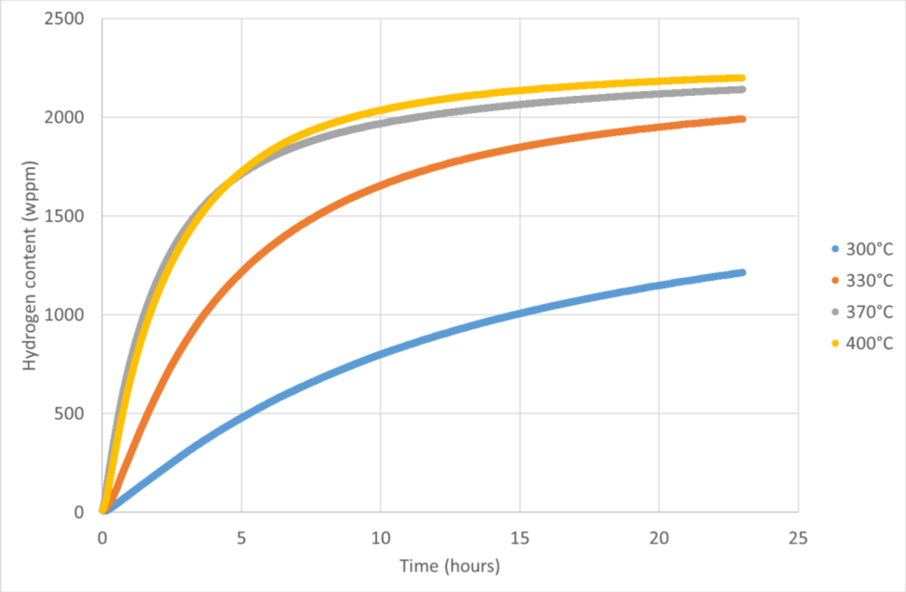

Fig. 46. Averaged Hydrogen content estimated evolution with time for Zircaloy-4 samples

The averaged hydrogen content evolution in the samples can be estimated from the pressure measurement in the chamber assuming that the pressure drop is entirely due to hydrogen absorption by the Zircaloy-4. The Fig. 46 illustrates the mean H content (in wppm) evolution with time deduced from the initial molar dihydrogen quantity filling the chamber and the accurate weighting of the samples.

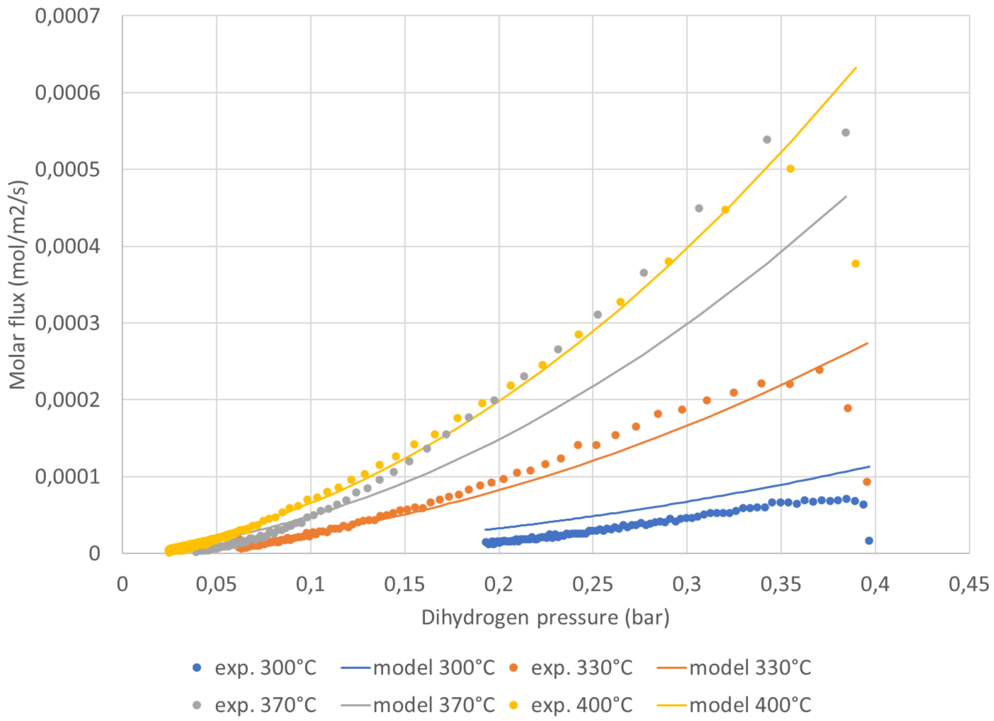

Fig. 47. Experimental hydrogen molar flux evolution with dihydrogen pressure for Zircaloy-4 samples and corresponding hydrogen molar flux calculated with the proposed model

The molar hydrogen flux (mol/m^2/s) can then be calculated knowing the total surface of the samples. Fig. 47 shows the molar hydrogen flux for Zircaloy-4 samples plotted versus the dihydrogen pressure. The hydrogen molar flux and thus the hydrogen absorption increase with the temperature in the range 300-400°C.
A temperature dependent quadratic evolution of the hydrogen molar flux with dihydrogen pressure has been proposed and fit over the experimental data. Results of this correlation are plotted in solid lines on Fig. 47 for each temperature and shows a good agreement.

$$\tau_{H2}[mol/m^2/s] = (aT + b)P_{H2} + (cT + d)P_{H2}^2$$

With a, b, c, d as fitting parameters and P_{H2} the dihydrogen pressure in bar and T the temperature in Kelvin.

a	2.7301E-05
b	-1.5026E-02
c	2.8136E-06
d	-1.5725E-03

4.2.5 General assumptions and pre-irradiation conditions

The fuel rod geometry is defined as follows:

Internal cladding radius:	4.18mm
External cladding radius:	4.75mm
Total length:	3.60m

The fuel stack is considered on the total length of the cladding thus plenums are not taken into account in the calculation.
An IRSN reference case of UO_2 and mixed oxide (MO_X) core of a pressurized water reactor has been chosen to initialize the pressure and temperature with a realistic history of irradiation. The corresponding averaged linear power history is illustrated in Fig. 48. The case of the fuel rod has been chosen in order to minimize the internal pressure of the rod and subsequently maximize the pressure difference with the primary circuit which is the driving force for the entry of water through the primary defect. The time of occurrence of the primary defect has been chosen at the beginning of the second irradiation cycle (approx. 260 days).
The FRAPCON code is used to calculate the internal pressure and internal / external temperatures of the fuel rod at this moment. These pressure and temperatures values are used in the SHOWBIZ model as imposed boundary conditions and remain fixed during the secondary hydriding calculation. Therefore, the internal pressure of the fuel rod is 68 bar at 260 days (see Fig. 49). The internal and external temperatures of the fuel rod are illustrated in Fig. 50, respectively 350°C and 380°C in the upper part of the fuel rod during normal operating conditions.

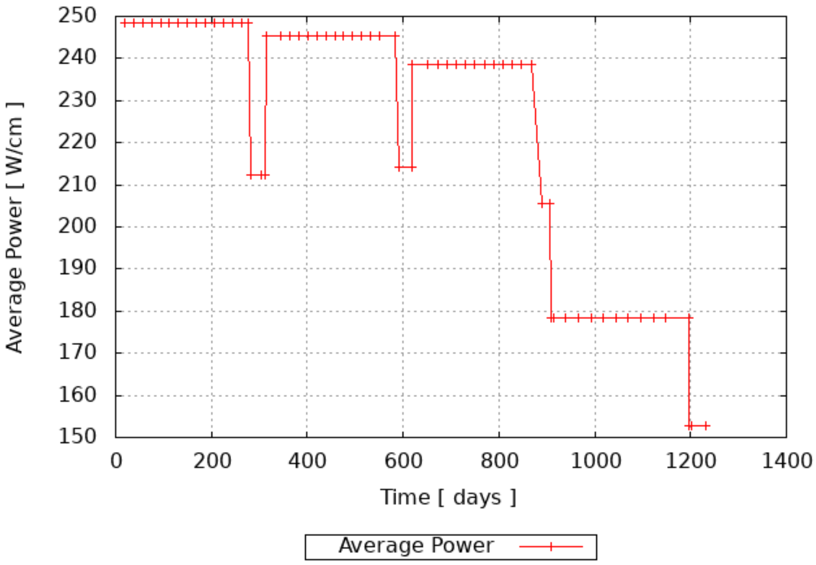

Fig. 48. Average linear power for the reference MO_X fuel rod used to initialize the secondary hydriding calculation

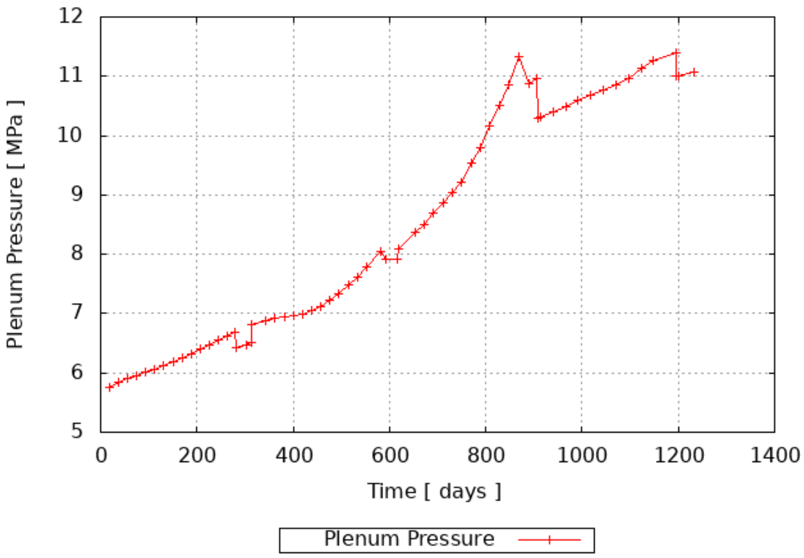

Fig. 49. Internal pressure of the reference MO_X fuel rod calculated with FRAPCON code

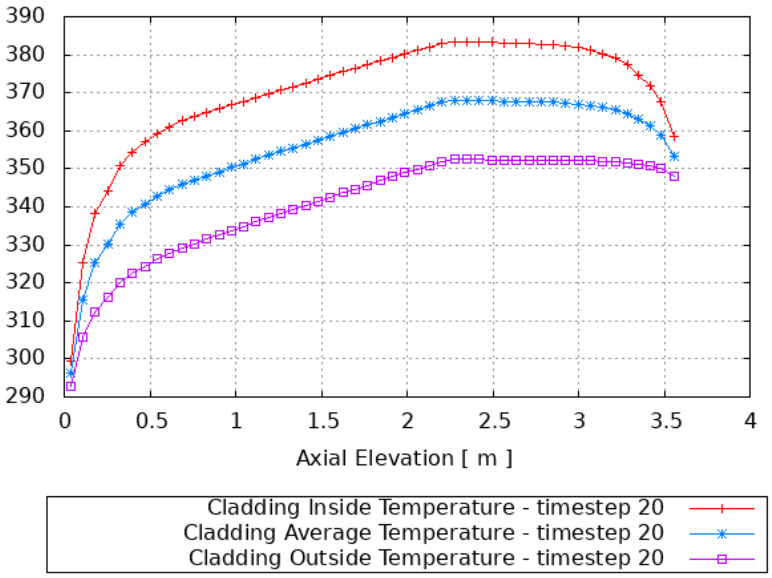

Fig. 50. Internal and external temperatures of the reference MOX fuel rod calculated with FRAPCON code

4.2.6 Results

In the following, we present SHOWBIZ results for a defective fuel rod with a primary defect located at 30cm from the bottom of the fuel rod that occurs at the beginning of the second irradiation cycle. In this case, the discretization is of 50 axial meshes, 1 azimuthal mesh and 20 radial meshes in the thickness of the cladding.
Fig. 51 shows the evolution of the gas distribution in the defective fuel rod. The partial pressure of H_2 (black), partial pressure of H_2O (red) and He (green) are represented at 0.1s (a), 1s (b), 10s (c) and 1 month (d). We see that the water enters the fuel rod at the primary defect position. From the very first seconds, the steam is consumed by the internal oxidation of the cladding and both steam and dihydrogen fill the free volumes and push the He gas higher in the fuel rod. Pressure equilibrium is reached in less than 10s (see Fig. 51c).

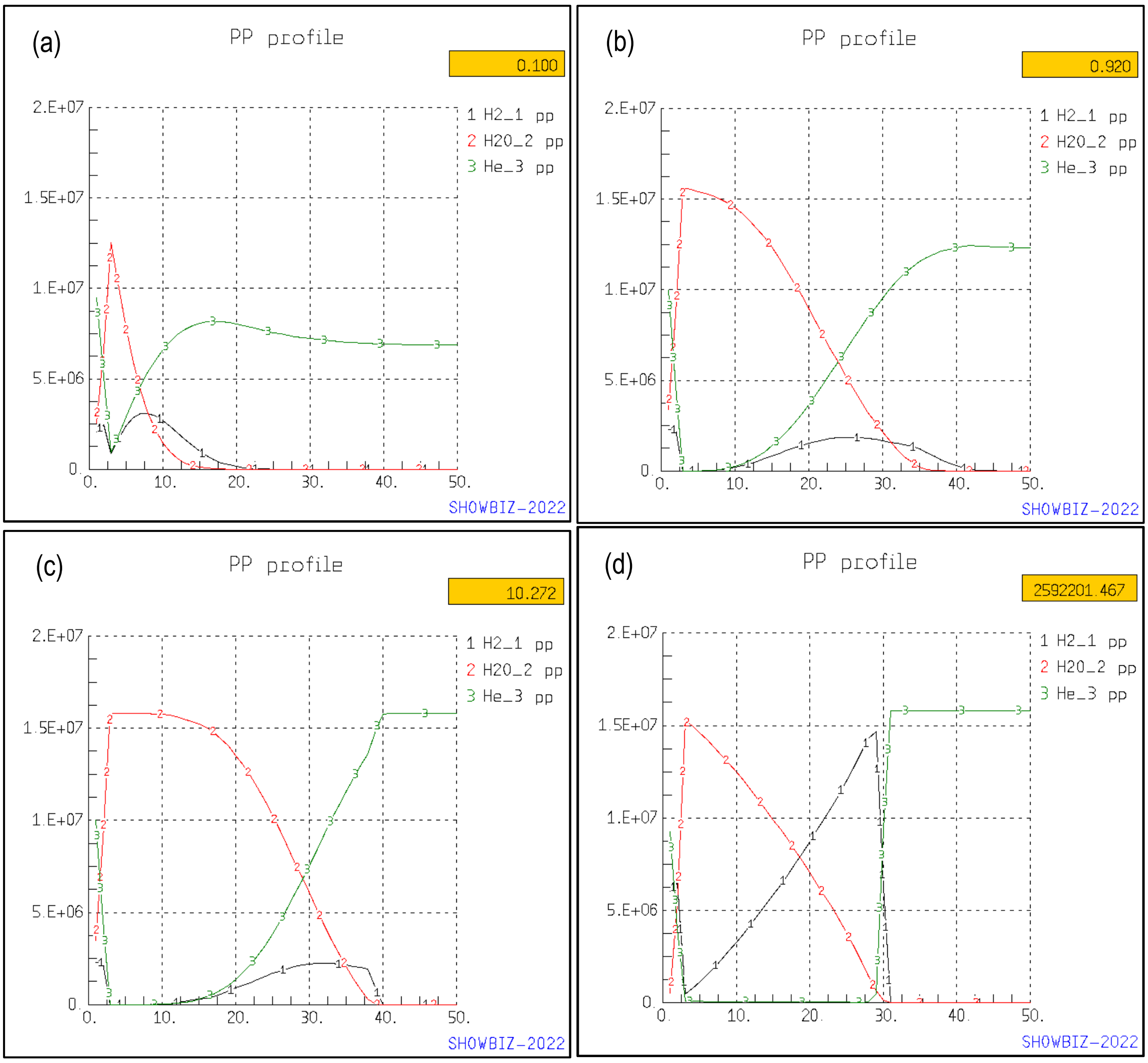

Fig. 51. Partial pressure of H_2, H_2O and He (Pa) axial profile along the 50 meshes at 0.1s (a) 1s (b) 10s (c) and 30 days (d). The primary defect is located at mesh 3

After this rapid initial phase, a cyclic regime establishes with consumption of H_2 where the partial pressure of H_2 is higher than the partial pressure of H_2O, new entry of water to compensate this depression etc. We observe that the diffusion of He is compensated by the new entries of water. After few hours, the gas distribution is established with almost pure H_2 atmosphere at mesh 30 that corresponds to a distance of 2m from the primary defect.
Fig. 52 shows the evolution of the hydrogen content inside the cladding. We see that the hydrogen uptake is very localized above 2m. In one day (Fig. 52a), a concentration of 100wppm is reached. At day 3 (Fig. 52b) the terminal solid solubility at precipitation is reached at the external side of the cladding and precipitation starts.

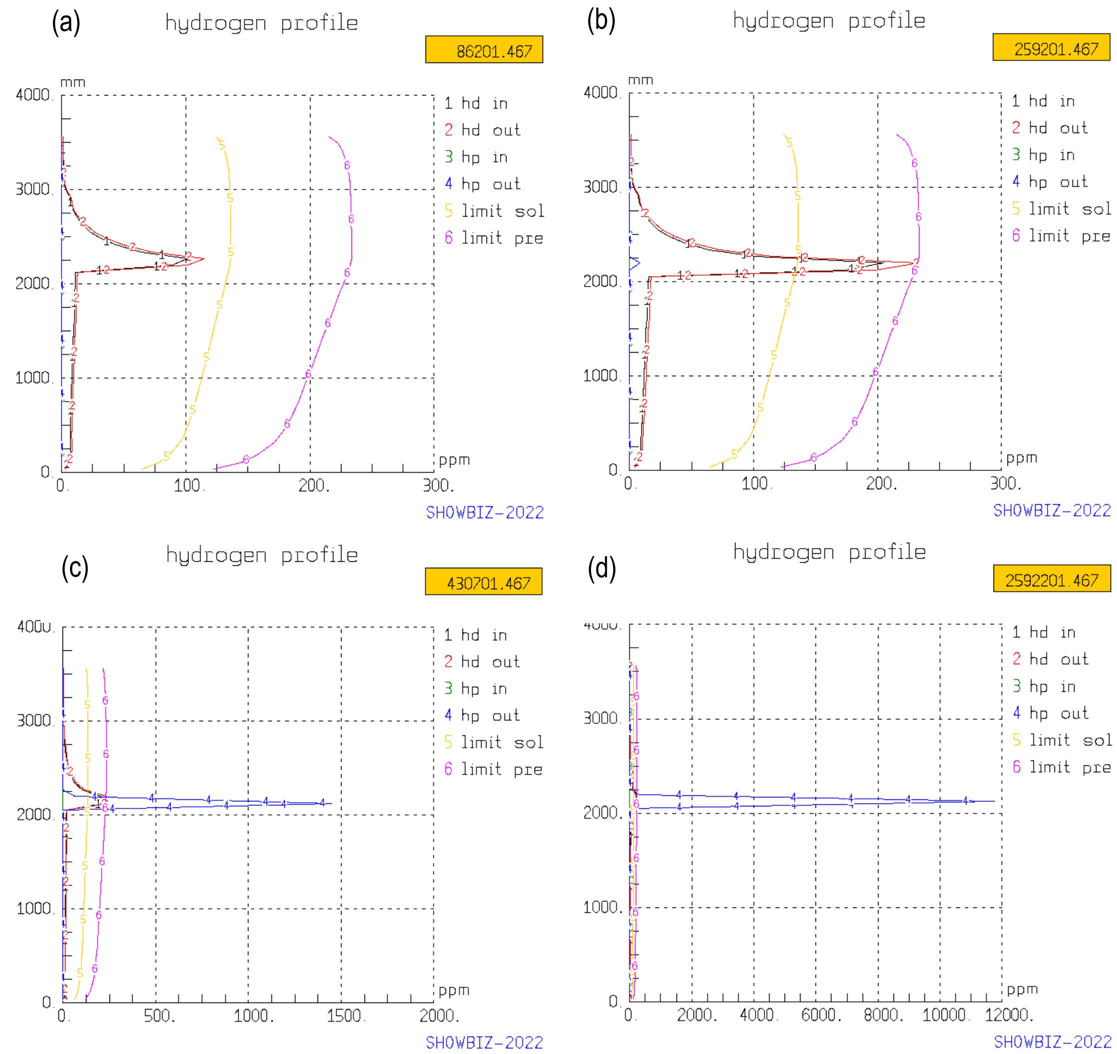

Fig. 52. Evolution of the axial profile hydrogen content in wppm within the cladding. The duration after the occurrence of the primary defect are 1 day (a), 3 days (b), 5 days (c) and 30 days (d). Axial profiles at the internal side of the cladding (in) and the outside (out) are plotted for H in solid solution (hd) and H precipitated (hp). Terminal solid solubility are also plotted for the external side temperature

The hydrogen uptake continue at the same location and the hydrogen diffuses towards the external side of the cladding due to a lower temperature. At day 5 (Fig. 52c), the precipited concentration is 1500wppm and as high as 12000wppm after a month (Fig. 52d).
The Fig. 53 illustrates the formation of a secondary defective region with very high H content (above 1000wppm. The precipitated hydrogen accumulates at the external side of the cladding and form a blister. One month after the occurrence of the primary defect and with normal operating conditions, 1/3rd of the cladding thickness is affected by the secondary hydriding.

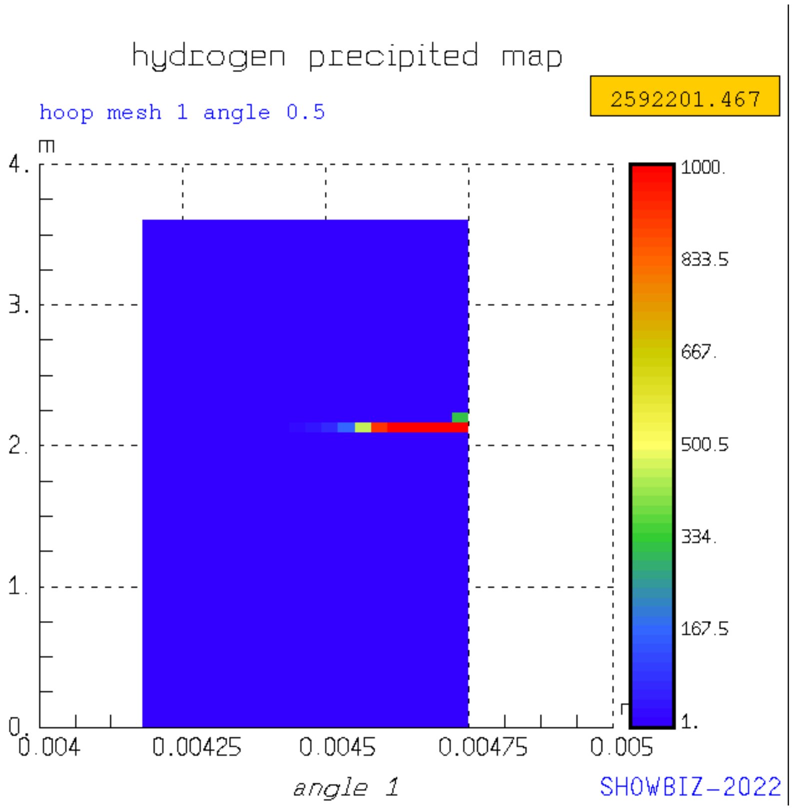

Fig. 53. 2D map of the precipitated hydrogen content in the cladding a month after the occurrence of the primary defect

4.3 Conclusion

The IRSN SHOWBIZ software is able to qualitatively model the secondary hydriding phenomena from water penetration to the formation of hydride blisters. The key physical mechanisms are the internal redistribution of the gaseous species, the internal oxidation and the hydrogen uptake and are sufficient to explain the position of the secondary defect respective to the position of the primary defect. Uncertainties remain regarding the kinetics of axial gas transport and chemical reactions at the internal side of the cladding while experimental data under irradiation condition are lacking and are limiting elements to have a more quantitative modeling.
The main conclusions of this work concerning the modeling of secondary hydriding in normal operating conditions are the relevance of using:

- a Darcy model for gas transport in the case of a closed pellet-clad gap,
- a condition over the partial pressure ratio between dihydrogen and steam rather than considering an internal protective oxide layer for the hydrogen uptake localization.

References

[1] Review of fuel failure in water cooled reactor, IAEA Nuclear Energy Series No. NF-T-2.1 (2010)

[2] E. Adams and R.E. Richie, On-Line Correlation of RCS Xenon Activities with PWR Fuel Assemblies Containing Leaking Fuel Rods, International Conference: Water Chemistry of Nuclear Reactor Systems, San Francisco CA, (2004)

[3] Fragema fuel reliability: from detection of fuel failures to the feedback on design and fabrication, A. Dumont, AIEA-TECDOC-709, Fuel failure in normal operation of water reactors: experience, mechanisms and management, (1992)

[4] J.C. Clayton, Internal hydriding in irradiated defected zircaloy fuel rods - a review, DOE Research and development report WAPD-TM-1604 (1987)

[5] J.C. Clayton, Internal hydriding in irradiated defected zircaloy fuel rods, Zirconium in the Nuclear Industry 8th, STP 1023, ASTM (1989) p.266-288

[6] J.H. Davies, J.H., Secondary damage in LWR fuel following PCI detection - characteristics and mechanisms, IAEA Spec. Meeting on Behavior of Defected Zirconium Alloy Clad Ceramic Fuel in Water Cooled Reactors, IWGFPT-6 (1980) p.135-140, Transactions of the Am. Nuc. Soc. 50 (1982) p269-270

[7] D.R. Olander et al, Chemical processes in defective LWR fuel rods, J Nucl. Mater. 248 (1977) 214–219

[8] J.M. Markowitz, "Internal Zirconium Hydride Formation in Zircaloy Fuel Element Cladding Under Irradiation," WAPD-TM-351 (1963)

[9] D.R. Olander et al, Steam oxidation of fuel in defective LWR rods, Journal of Nuclear Materials 270 (1999) 11-20

[10] D.R. Olander, Nucl. Technol. 74 (1986) 215.

[11] F. Garzarolli, R. von Jan, and H. Stehle, "The Main Causes of Fuel Element Failure in Water-Cooled Power Reactors," Atomic Energy Review, 17, 31-128 (1979)

[12] Y.-S. Kim et al, HYDRIDING FAILURE ANALYSIS BASED ON PIE DATA, Proc. JAERI 99-009 (1999) p278-285

[13] K. Une, Kinetics of reaction of zirconium alloy with hydrogen, Journal of the Less-Common Metals 57 (1978) p93-101

[14] Y.S. Kim, W.-E Wang, D.R. Olander, High-pressure hydriding of Zircaloy, JNM 240 (1996) 27-31

[15] Y.S. Kim, W.-E Wang, D.R. Olander, High pressure hydriding of sponge-Zr in steam-hydrogen mixtures, JNM 246 (1997) 43-52

[16] E.A. Gulbransen, K.F. Andrew, Metall. Trans. 185 (1949)

[17] J. Belle et al, J. Electrochem. Soc. 101 (1954) 211

[18] I.A. Evdokimov et al, Secondary hydriding criteria under irradiation conditions, Nuclear Engineering and Design 241 (2011) p1414-1420

[19] I.A. Evdokimov et al, A Mechanistic Approach to Develop the Secondary Hydriding Criteria, IAEA 8 int. Conf. on WWER fuel performance, modelling and experimental support, Bulgaria (2009)

[20] Evdokimov I.A., Likhanskii V.V., "In-Pile Criteria for the Initiation of Massive Hydriding of Zr in Steam-Hydrogen Environment," Proc. 15th Int. Symp. on Zirconium in the Nuclear Industry, Sunriver, OR, USA, June 24-28, 2007. Journal of ASTM International, Vol.5, No.1, 2008

[21] H Mogard et al, Studies in the R2 test reactor of secondary damage formation in LWR fuel rods with simulated defects, IAEA-TECDOC-709, Fuel failure in normal operation of water reactors: experience, mechanisms and management, (1992)

[22] Y. Kim and S. Kim, Kinetic studies on massive hydriding of commercial zirconium alloy tubing, JNM 270, 1-2, p.147-153, 1999

[23] J.-M. Lee et al, A study on the reaction of Zircaloy-4 tube with hydrogen/steam mixture, Journal of Nuclear Materials 491 (2017) p105-114

[24] D.H. Locke, The behaviour of defective reactor fuel, Nuc Eng and Design 21 (1972) 318-330

[25] Gräslund, C., Lassing, A. (1997). Study of secondary hydriding in BWR test fuel. Proceedings of the European Working Group "Hot Laboratories and Remote Handling". Studvisk Nuclear AB

[26] Grounes, M., Lysell, G., & Bengtsson, S. (1997). Fuel R&D at Studsvik II. General studies of fuel behaviour including pellet-cladding interaction. Nuclear engineering and design, 168(1-3), 151-166

[27] Grounes, M., Gräslund, C., Lysell, G., & Tomani, H. (1997). Fuel R&D at Studsvik III. Studies of special phenomena in fuel behaviour: lift-off and defect fuel degradation. Nuclear engineering and design, 168(1-3), 167-176

[28] J. Wright et al, Summary of test reactor experiments to simulate secondary fuel degradation and its mitigation, Water Reactor Fuel Performance Meeting WRFPM 2017, Jeju Island, Korea (2017)

[29] E.YU. Afanas'eva et al, Simulation of the hydriding failure of fuel elements in water-cooled reactors, Atomic Energy, Vol. 95, No. 4, 2003

[30] E.YU. Afanas'eva et al, Modelling of Fuel Rod Hydriding Failures in Water Reactors, Transactions of the 17th International Conference on Structural Mechanics in Reactor Technology (SMiRT 17) Prague Czech Republic, August 17 -22, (2003)

[31] M.S. Veshchunov and V.E. Shestak, Modeling of Zr alloy burst cladding internal oxidation and secondary hydriding under LOCA conditions, Journal of Nuclear Materials 461 (2015) 129-142

[32] Rudling, P. (2001). Secondary degradation mechanisms-a theoretical approach to remedial actions (No. SKI-R--00-32). Swedish Nuclear Power Inspectorate

[33] Technical report IRSN/2021-00357, Endommagement des crayons inétanches en fonctionnement normal – Hydruration secondaire, IRSN, 2021

[34] Technical report IRSN/2021-00890, Rapport d'avancement sur l'hydruration secondaire et son implementation dans le logiciel SHOWBIZ – Contribution au livrable D4.5 du projet H2020 R2CA, IRSN 2022

[35] Technical report EK-2021-437-1-1-M0, Hydrogen uptake tests with zirconium alloys at reactor operational temperatures, EK, 2021

[36] Technical Report IRSN/2022-00062, *SHOWBIZ 2022 - theoretical manual*., IRSN, 2022

5 UJV: Internal oxidation and hydriding of the clad in TRANSURANUS

The main objective of the contribution from UJV in this task consisted of enhancing the TRANSURANUS code by means of a model for secondary hydriding based on a model for the diffusional gas transport in the fuel rod cladding gap. The model should then be combined with the new model for hydrogen redistribution and precipitation/dissolution that is being developed at JRC in collaboration with other users of the TRANSURANUS code (see below). The effect of the resulting hydrogen concentration on the mechanical properties of the cladding can then be take into consideration, in the same way as was done for LOCA simulations [see ref. 1 §6].

In a first step, a standalone model has been developed for vapour and hydrogen at UJV. Validation and testing of the model were based on the comparison with experimental data from the OECD Halden Reactor Project, as shown in Fig. 54.

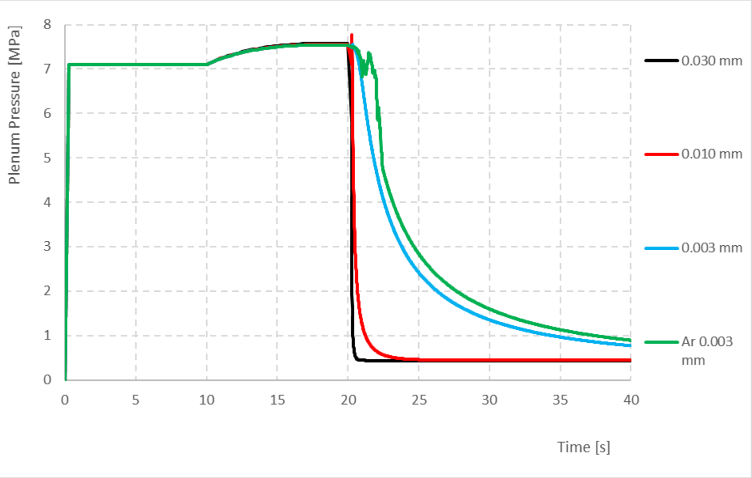

Fig. 54. Comparison of the plenum pressure (MPa) versus time (s) predicted by the standalone model developed at UJV, with experimental data from the Haden Reactor Project

Although the model shows very encouraging results, there are still some numerical instabilities that need to be addressed before it can be implemented in the TRANSURANUS code. This will be beyond the time frame of the R2CA project, given the shift of focus of the activities at UJV for ensuring nuclear fuel supply in the Russian type VVER reactors operated in the Czech Republic in the wake of the war in Ukraine. For this reason, the new specific Euratom project APIS has been launched, in which UJV is actively participating.

6 JRC: Hydrogen uptake and redistribution in the cladding

6.1 Hydrogen uptake

The hydrogen uptake modelling in the TRANSURANUS code is different for base irradiation and accident conditions. In the course of the previous ESSANUF project [2], a model for hydrogen uptake during normal operation conditions has been implemented on the basis of that presented by [3]:

$$\mathrm{F}(s) = \kappa_1 + \frac{\kappa_2}{s\kappa_3}\left(1 - e^{-s\kappa_3}\right)$$

$$c_H = A\frac{s}{\left(r_o - r_i\right)}\frac{2r_o}{\left(r_o + r_i\right)}$$

where
F(s) = hydrogen pickup fraction in the cladding (/)
s = corrosion layer thickness
r_o = reference cladding outer radius
r_i = reference cladding inner radius
c_H = integrated hydrogen uptake (ppm)

In order to take into account hydrogen uptake under LOCA conditions, a standalone model was developed that is based on two fundamental steps [4], i.e. the modelling of the solubility of the hydrogen in the metal, and the kinetics of the absorption process. Therefore, the actual hydrogen content (cH) of the cladding can be expressed as follows:

$$c_H(t) = c_S \cdot \omega(t)$$

Where c_S represents the solubility limit in atomic ratio (H/Zr) and ω(t) is a time-dependent factor describing the absorption kinetics.
At high temperature (> 600°C) the hydrogen in the Zirconium is in interstitial solid solution. The solubility limit is proportional to the square root of the partial pressure of the ambient gas according to Sieverts` law. However, due to the saturation of the available interstitial sites in the Zr lattice, this law tends to overestimate the equilibrium hydrogen concentration above the (H/Zr) atomic ratio of 0.6. In order to consider this saturation effect, Moalem et al [5] proposed a modified relation:

$$c_S = \frac{K\sqrt{p_H}}{1 + \frac{K}{M}\sqrt{p_H}}$$

where p_H is the hydrogen partial pressure in the environment, M symbolises the total number of interstitial sites for hydrogen dissolution per Zr atoms and K is the solubility constant. The solubility is temperature dependent and can be expressed with an exponential function of the Gibbs free energy (G):

$$K = \exp\left(-\frac{\Delta G}{RT}\right) = \exp\left(-\frac{\Delta H + \delta H}{RT} + \frac{\Delta S + \delta S}{R}\right)$$

where ΔH and ΔS are the partial molar enthalpy and entropy of the gas solution in as-received cladding, respectively. However, the oxygen already diffused into the metal influences the hydrogen solubility considerably. The variation of the molar quantities in oxygen-containing cladding is represented by δH and δS. We assumed that, on the one hand, the lattice dilatation and configuration change due to oxygen uptake influence the partial molar enthalpy through a linear function of the oxygen content and, on the other hand, the blocking of the hydrogen uptake by interstitial oxygen atoms causes the variation of the partial molar entropy. Consequently, δH and δS are expressed as follows:

$$\delta H = R \cdot B \cdot c_O$$

$$\delta S = R \cdot \ln\left(1 - A \cdot c_O\right)$$

where c_O is the oxygen concentration (atomic ratio) in the cladding, B is the proportionality factor for the molar enthalpy change and A represents the factor of interstitial sites for hydrogen uptake blocked by an oxygen atom.

For the kinetics of the hydrogen absorption, we assume that at high temperatures, the diffusion of H in zircaloy is much higher than the dissociation rate of hydrogen molecules on the cladding surface and their subsequent chemisorption. As a result, the rate equation for H-uptake is written as [6]:

$$\frac{d\omega}{dt} = c_S\ \eta\left(1 - \omega^2\right)$$

Where ω denotes the hydrogen content of the zirconium relative to the absorption, or the solubility limit, (c_H / c_S), t is the time and η corresponds to the kinetics constant.

The integration of the previous equation with the initial condition $c_H(t=0) = 0$ yields:

$$\omega(t, c_S) = \frac{\exp\left(c_S\, 2\eta\, t\right) - 1}{\exp\left(c_S\, 2\eta\, t\right) + 1}$$

The kinetics constant η is expressed with an Arrhenius function fitted to experimental data:

$$\eta = \exp\left(4.56 - 1.24 \cdot 10^4 / T\right)$$

In the frame of a bilateral agreement with the JRC, Nucleocon has implemented the standalone model for H-uptake during LOCA conditions in the TRANSURANUS code [7]. The model for hydrogen uptake under H_2 rich atmosphere has been compared with the experimental data of EK by NINE and described below.

6.2 First Model of hydrogen migration

Radial hydrogen migration in LWR cladding is an important performance feature. More precisely, the diffusion and precipitation of the hydrogen picked up in LWR fuel claddings is a key aspect for fuel safety given its impact on the material resistance to failure. Hydrogen redistribution has been modelled by Sawatzky in 1960 [8] and by Marino in 1972 [9]. Hydrogen redistributes under high temperature (and stress) gradient during irradiation leading to considerable local variations of concentration that affect the cladding properties. Indeed, the hydriding in zircaloy cladding may give rise to the formation of dense hydrides regions, which negatively affect the alloy ductility. Especially at high burnup, the so-called hydride rim is related to the formation of an increased hydrogen concentration in the vicinity of the cladding waterside (i.e. primary hydriding). In the event of a defective fuel rod, hydrogen can also be picked up at the cladding fuel side (secondary hydriding), which may lead to a massive hydriding that may evolve in the formation of hydrides blisters.
In order to predict the potential appearance of hydriding it is crucial to model the uptake, followed by the in-clad hydrogen migration and precipitation. In other words, the estimation of the extent and concentration of the hydrides formed is needed to characterise the mechanical state of the cladding. This is especially important if transient mechanical loads would come into play after the hydriding (i.e., conditions that would lead to cladding failure), be it in reactor in the event of a RIA, or during storage of spent nuclear fuel. Therefore, the first step following hydrogen uptake, consists of modelling of the hydrogen radial distribution, which is the subject of this report. In this following,

we therefore outline the implementation of a first model for the radial redistribution of hydrogen absorbed in zirconium cladding for the TRANSURANUS fuel rod performance code of the European Commission. The model relies on the solution of the diffusion equation and includes the Soret effect in cylindrical geometry. From the numerical point of view, it is similar to the model for the Pu redistribution in cylindrical MOX pellets of FBR fuels, already considered in the PUREDI model of TRANSURANUS.
In the TRANSURANUS fuel performance code, hydrogen absorption is considered during both normal operation conditions and LOCA type conditions. Hydrogen in solid solution in zirconium can redistribute and will precipitate to form zirconium hydrides as the temperature is decreased below its solubility limit, which is a reversible process. The radial redistribution model is based on the work of Courty et al. [10], who suggested the adoption of the standard equation of thermal diffusion:

$$\frac{\partial c_H^s}{\partial t} = -\nabla \cdot J_{Hs}$$

$$J_{Hs} = -D_H \left(\nabla c_H^s + c_H^s \left(1 - c_H^s\right) \frac{Q_H}{RT^2} \nabla T \right)$$

where

J_{Hs} = vector flux of soluble hydrogen species per unit area and unit time,
c^s_H = concentration of hydrogen in solid solution,
R = universal gas constant,
T = absolute temperature,
Q_H = heat of transport for hydrogen in zircaloy,
D_H = diffusion coefficient of hydrogen in zircaloy.

In line with Courty et al. [10], we neglect diffusion of hydrogen in the delta phase of hydride, as well as the Dufour effect, and the coupling of the stress state to the chemical potential of dissolved hydrogen. We can neglect the diffusion in the hydride since the stoichiometry of the hydride phase is fixed. In fact, there is little or no driving force for diffusion of hydrogen in the hydrides, and the diffusivity of hydrogen in hydrides has been measured to be at least 3 times smaller than the diffusivity of hydrogen in zirconium.
The Dufour effect results in a small heat flux due to a concentration gradient in dissolved hydrogen, i.e. it is the Onsager relationship reciprocal to the Soret effect. For the Zr-H system, the heat flux due to the Dufour effect is estimated to be three orders of magnitude smaller than the heat flux due to Fourier's Law, hence we neglect it also in the current model.

Unlike Jernkvist et al.[11], we do not consider any free hydrogen in the hydride phases since we neglect their mobility in this phase like Courty [10]. Besides, Jernkvist et al. applied a constant ratio of free hydrogen in the hydrides to that in the metal phase of 0.05.

If axial symmetry is assumed and axial gradients are neglected, dissolved H can migrate only along the radial coordinate (r) so that Eqs. (1) and (2) can be rewritten in a similar way as for Pu in PUREDI [12], Am in AMREDI [13] and O in OXIRED [14] as follows:

$$\frac{\partial c_H^s}{\partial t} = \frac{1}{r}\frac{\partial}{\partial r}\left\{ r D_H \left(\frac{\partial c_H^s}{\partial r} + c_H^s \left(1 - c_H^s\right) \frac{Q_H}{RT^2} \frac{\partial T}{\partial r} \right) \right\}$$

As concerns boundaries (i.e., at the clad outer R_o and inner R_i radius), Neumann's conditions are to be applied in accordance with the oxidation kinetics at both sides. More precisely, we consider the conservation of mass boundary:

$$\frac{d\overline{c}_H^s}{dt} \cdot V = -J_{Hs}(R_o) \cdot S$$

where

$\bar{c}_H^s$ = total absorbed amount of hydrogen in the cladding section/slice

V = volume of metallic cladding considered in the current section/slice

$J_{Hs}(R_o)$ = flux of H atoms entering the volume through the outer surface

S = outer surface of the cladding through which the hydrogen is taken up

Considering a hermetic cladding without inner oxidation for the moment, the variation of the total hydrogen concentration in the section/slice per unit time is determined by the H-uptake model (the existing "conhy" or "hzr" global variable names can be used as described in the Handbook [15]):

$$\frac{d\bar{c}_H^s}{dt} = \frac{\bar{c}_H^s(t+\Delta t) - \bar{c}_H^s(t)}{\Delta t}$$

Leading to

$$J_{Hs}(R_o) = -\frac{d\bar{c}_H^s}{dt}\frac{\left(R_o^2 - R_i^2\right)}{2R_o}$$

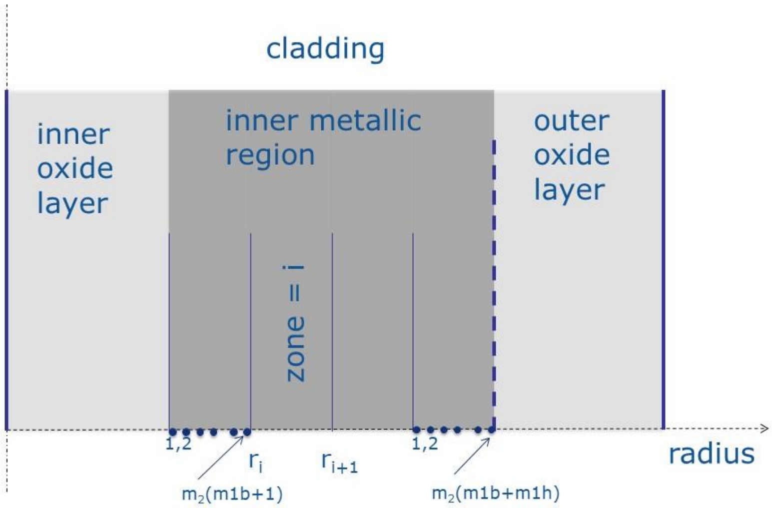

Fig. 55. schematic discretisation of cladding in TRANSURANUS. Variable names m1, m1h, m1h and m2 are taken from the TRANSURANUS Handbook [15] and correspond to the coarse zone (m1) and fine zone (m2) discretisation in the fuel ("b" refers to brennstoff) and cladding ("h" refers to cladding)

At the inner side of the cladding, the flux of hydrogen uptake is zero when the cladding is intact. After rod burst, the flux of hydrogen entering the cladding could be obtained in a similar way as for the outer surface:

$$J_{Hs}\left(R_i\right) = 0 \qquad \text{before burst}$$

$$J_{Hs}\left(R_i\right) = -\frac{d\bar{c}_H^s}{dt}\frac{\left(R_o^2 - R_i^2\right)}{2R_i} \qquad \text{after burst}$$

This is not considered at the moment in the hydrogen uptake model. It should be underlined, however, that a zero-flux boundary condition with an intact cladding does not imply that the solid solution concentration profile is flat at the inner surface. Indeed, if there is a temperature gradient, the concentration profile has to show a finite gradient in order to compensate for the flux induced by the Soret effect:

$$\nabla c_H^s = -c_H^s \frac{Q_H}{RT^2} \nabla T$$

This will be taken into consideration in our numerical model.

6.2.1 Consideration of hydride precipitation and dissolution

When the dissolved hydrogen concentration exceeds the thermal solid solubility limit for precipitation (TSSp), brittle zirconium hydrides precipitate. Although different forms exist, it is commonly considered that essentially delta hydrides form, typically in the colder outer part of the cladding. If the temperature increases above the terminal solid solubility for dissolution (TSSd), on the other hand the hydrides can re-dissolve. There is certain hysteresis, i.e. a difference between the limit for precipitation and dissolution, which is attributed to the additional energy required to form the hydrides that have a lower specific volume. As a result, there is no precipitation nor dissolution when the dissolved hydrogen concentration lies between both limits or phase equilibria (TSSp and TSSd).

When the rate of cooling or heating is moderate, precipitation and dissolution are diffusion controlled and their kinetics strongly depend on temperature. Precipitation proceeds by diffusion of interstitial hydrogen atoms to dislocations and/or grain boundaries where hydrides can nucleate and grow. Similar to the model of Ham [16] for precipitation on a periodic array of dislocations, we consider a point-kinetics model for the phase transformation. The modelling of the precipitation and dissolution in fuel performance codes relies thus on a rate equation that also reflects the hysteresis as follows:

$$\frac{dc_H^p}{dt} = \begin{cases} K_p\left(c_H^s - TSSp\right) & c_{Hs} > TSSp \\ 0 & TSSp \geq c_{Hs} > TSSd \\ K_d\left(c_H^s - TSSd\right) & c_{Hs} \leq TSSd, c_{Hp} > 0 \\ 0 & c_{Hs} \leq TSSd, c_{Hp} = 0 \end{cases}$$

where the model parameters K_p, K_d, TSSp and TSSd have a typical Arrhenius form. It should be kept in mind that the first order approximation to the diffusion-controlled phase transformation is appropriate only for near-equilibrium conditions, i.e. with moderate temperature variations such that $\frac{\left|c_H^s - TSSd\right|}{TSSd} \leq 1$. We make this assumption in our simplified model for hydrogen in zirconium cladding. This could also be taken into consideration for the time-step control.

The precipitation/re-dissolution affects the local balance equation for dissolved hydrogen, in that a corresponding source term is added:

$$\frac{\partial c_H^s}{\partial t} = \frac{1}{r}\frac{\partial}{\partial r}\left\{ rD_H \left(\frac{\partial c_H^s}{\partial r} + c_H^s\left(1 - c_H^s\right)\frac{Q_H}{RT^2}\frac{\partial T}{\partial r} \right) \right\} + S_{p/d}$$

The source term ($S_{p/d}$) corresponds to the rate of change of the hydrogen concentration contained in the hydrides given above, and we consider the same boundary conditions at the inner and outer surface of the cladding. It should be underlined that the rate or precipitation is orders of magnitude lower than the rate of dissolution, which could require special attention for the time-step control.

Finally, when considering hydrogen in cladding as a result of oxidation, the concentrations are much smaller than one, hence we obtain

$$\frac{\partial c_H^s}{\partial t} = \frac{1}{r}\frac{\partial}{\partial r}\left\{ rD_H \left(\frac{\partial c_H^s}{\partial r} + c_H^s \frac{Q_H}{RT^2}\frac{\partial T}{\partial r} \right) \right\} + S_{p/d}$$

6.2.2 Numerical algorithm of HYREDI

The cladding is divided into m – 1 radial zones (cf. Fig. 56) that need not to be equidistant. In the following, a superscript (i) indicates a radial zone whereas a subscript indicates the value at the node r_i.

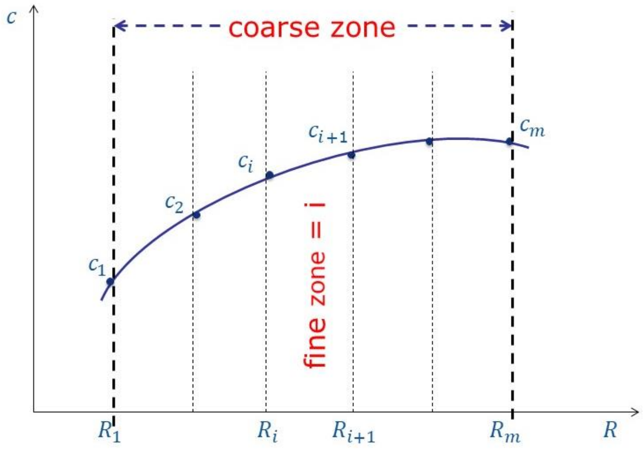

Fig. 56. discretisation for dissolved hydrogen concentration in HYREDI

For simplicity, the subscript Hs in the definition of the physical quantities in section 2 is omitted (i.e., c = c_{Hs}, D = D_H, J = J_{Hs}, etc.).
For the discretisation with respect to space, we write for each zone the balance in a conservative form (integrating the PDE in a cylindrical ring, and dividing by the volume of the ring):

$$w^{(1)}\dot{c}_1 + \left(1 - w^{(1)}\right)\dot{c}_2 = -\frac{2\, r_2 J_2}{r_2^2 - r_1^2} + S_i \qquad \text{Zone 1 (A1)}$$

$$w^{(i)}\dot{c}_i + \left(1 - w^{(i)}\right)\dot{c}_{i+1} = -\frac{2\left(r_{i+1} J_{i+1} - r_i J_i\right)}{r_{i+1}^2 - r_i^2} + S_i \qquad \text{Zone 2....m – 2 (A2)}$$

$$w^{(m-1)}\dot{c}_{m-1} + \left(1 - w^{(m-1)}\right)\dot{c}_i = -\frac{2\left(r_m J_m - r_{m-1} J_{m-1}\right)}{r_m^2 - r_{m-1}^2} + S_i \quad \text{Zone m-1 (A3)}$$

where can be written as $S_i = S_{1,i} c_{H,i}^s - S_{2,\mathrm{i}}$ (with S1 = (-Kp) or Kd or 0, and S2 = S1 x(-TSSp) or TSSd), w is an area weighting factor, obtained by assuming a linear dependent concentration over the cylindrical ring (which is equivalent to the finite element discretisation method with linear basis function), leading to:

$$w^{(i)} = \frac{r_{i+1} + 2r_i}{3\left(r_{i+1} + r_i\right)} \qquad \text{(A4)}$$

and the flux J_1 is taken zero at this stage of the model development, i.e. we disregard hydrogen uptake at the inner surface of the cladding. The expression for the outer flux J_m will be dealt with in more detail below.
The time-derivative of dissolved hydrogen concentration is discretized with the backward Euler method or implicit time stepping scheme as follows:

$$\dot{c}_i = \frac{c_{i,n+1} - c_{i,n}}{\Delta t} \qquad \text{(A5)}$$

Concerning the term J_i, its discretization requires the definition of the radial derivative of c, for which we chose the central difference approximation:

$$\left.\frac{\partial c}{\partial r}\right|_i \approx \frac{1}{2}\frac{c_{i+1} - c_i}{r_{i+1} - r_i} + \frac{1}{2}\frac{c_i - c_{i-1}}{r_i - r_{i-1}} \qquad \text{(A6)}$$

The subscript n is omitted since the concentrations c_i are taken at time n+1 (i.e. are unknown). This is a fully implicit formulation. A comparison between implicit and explicit scheme was not yet performed for hydrogen, unlike for PUREDI where it showed a perfect agreement.
In order to write the equation system in a more convenient form for the numerical implementation, the following quantities are defined:

$$f_{i+1} = \frac{1}{2}\frac{1}{r_{i+1} - r_i} \qquad f_i = \frac{1}{2}\frac{1}{r_i - r_{i-1}} \qquad \text{(A7a,b)}$$

$$g_i = \frac{Q}{RT^2}\frac{\partial T}{\partial r} \qquad \text{(A8)}$$

$$h_{i+1} = \frac{2r_{i+1}}{r_{i+1}^2 - r_i^2} D_{i+1}\Delta t \qquad h_i^{*} = \frac{2r_i}{r_{i+1}^2 - r_i^2} D_i \Delta t \qquad \text{(A9a,b)}$$

The radial derivatives and the flux of dissolve hydrogen (J_i) can be respectively rewritten as:

$$\left.\frac{\partial c}{\partial r}\right|_i \approx c_{i+1} \cdot f_{i+1} + c_i\left(f_i - f_{i+1}\right) - c_{i-1} \cdot f_i \qquad \text{(A10)}$$

$$J_i = -D_i\left[c_{i+1} \cdot f_{i+1} + c_i\left(f_i - f_{i+1}\right) - c_{i-1} \cdot f_i + c_i \cdot g_i\right] \qquad \text{(A11)}$$

It can be noticed that all the values given in Eq. (A8) are known since they are defined at the previous time step according to the linearization of the diffusion equation by $c_H^s\left(1 - c_H^s\right) \approx c_{H,n+1}^s\left(1 - c_{H,n}^s\right)$ and taken at r = r_i.
According to the previous definitions, the system given by Eqs. (A1)-(A3) can be rewritten as follows:

$$\begin{aligned}
&c_1\left\{w^{(1)}\left(1 - S1_1\Delta t\right) + h_2 f_2\right\} + \\
&c_2\left\{\left(1 - w^{(1)}\right)\left(1 - S1_2\Delta t\right) - h_2\left(f_2 - f_3 + g_2\right)\right\} + \\
&c_3\left\{-h_2 f_3\right\} = \\
&w^{(1)}\left(c_{1,n} - S2_1\Delta t\right) + \left(1 - w^{(1)}\right)\left(c_{2,n} - S2_2\Delta t\right)
\end{aligned} \qquad \text{Zone 1} \qquad \text{(A12)}$$

$$\begin{aligned}
&c_{i-1}\left\{-h_i^* f_i\right\}+\\
&c_i\left\{w^{(i)}\left(1-S1_i\Delta t\right)+h_{i+1}f_{i+1}+h_i^*\left(-f_{i+1}+f_i+g_i\right)\right\}+\\
&c_{i+1}\left\{\left(1-w^{(i)}\right)\left(1-S1_{i+1}\Delta t\right)-h_{i+1}\left(-f_{i+2}+f_{i+1}+g_{i+1}\right)+h_i^* f_{i+1}\right\}+\\
&c_{i+2}\left\{-h_{i+1}f_{i+2}\right\}=\\
&w^{(i)}\left(c_{i,n}-S2_i\Delta t\right)+\left(1-w^{(i)}\right)\left(c_{i+1,n}-S2_{i+1}\Delta t\right)
\end{aligned}$$

Zone 2….m – 2

(A13)

For the last zone, however, we must elaborate the expression for the hydrogen flux at the outer surface somewhat differently:

$$J_m=-D_m\left[\left(\frac{c_m-c_{m-1}}{r_m-r_{m-1}}\right)+c_m g_m\right]=-D_m\left[f_m^*\left(c_m-c_{m-1}\right)+c_m g_m\right]$$

The equation thus becomes

$$\begin{aligned}
&c_{m-2}\left\{-h_{m-1}^* f_{m-1}\right\}+\\
&c_{m-1}\left\{w^{(m-1)}\left(1-S1_{m-1}\Delta t\right)+h_{m-1}^*\left(-f_m+f_{m-1}+g_{m-1}\right)+h_m f_m^*\right\}+\\
&c_m\left\{\left(1-w^{(m-1)}\right)\left(1-S1_m\Delta t\right)+h_{m-1}^* f_m-h_m\left(f_m^*+g_m\right)\right\}=\\
&w^{(m-1)}\left(c_{m-1,n}-S2_{m-1}\Delta t\right)+\left(1-w^{(m-1)}\right)\left(c_{m,n}-S2_m\Delta t\right)
\end{aligned}$$

Zone m – 1

(A14)

For the m unknowns, we need m equations. The last equation is given as J_m = J_{Hs}, where the right-hand side represents the influx of hydrogen due to oxidation as outlined above, and since

$$J_m=-D_m\left[\left(\frac{c_m-c_{m-1}}{r_m-r_{m-1}}\right)+c_m g_m\right]=-D_m\left[f_m^*\left(c_m-c_{m-1}\right)+c_m g_m\right]$$

We have

$$c_{m-1}\left(-f_m^*\right)+c_m\left(f_m^*+g_m\right)=\frac{d\bar{c}_{Hs}}{D_m\Delta t}\frac{\left(R_o^2-R_i^2\right)}{2R_o} \quad \text{(A15)}$$

As can be seen, Eqs. (A12)-(A15) consist of m equations for m unknowns. The resulting form of the equations system to calculate the hydrogen redistribution is pentadiagonal, which can be solved effectively like for the Pu redistribution. Since the fully implicit scheme guarantees numerical stability even for extremely large time steps, the time step length, which controls the hydrogen redistribution, has to be limited.

6.3 Summary and outlook

In this work, we outline the implementation of a first model for the radial redistribution of hydrogen absorbed in zirconium cladding, under the influence of the concentration and temperature gradients. The model relies on the solution of the diffusion equation and includes the Soret effect in cylindrical geometry. From the numerical point of view, it is similar to the model for the Pu redistribution in cylindrical MOX pellets of FBR fuels, considered in the PUREDI model of TRANSURANUS.

Numerous tests will be required in order to obtain a time step criterion similar to Eq. (A16) as a good compromise between accuracy and computational cost:

$$\Delta t \le 0.01 \cdot \max\left\{c_{i,n+1} - c_{i,n}\right\} \qquad \text{(A16)}$$

Subsequently, the model can be further extended for consideration of:

- The volume fraction of hydrides in reducing the flux term, as explained by Veshchunov et al.[17], Stafford et al. [18], Jernkvist [19] and Varias et al. [20]. This is important when the volume fraction of hydrides becomes important (but Stafford et al. have artificially limited this to 10% in BISON [18]). The current model presented above is therefore valid for claddings with modest hydrogen uptake like M5. However, this extension will require rewriting the equations with the additional multiplication term as suggested by Veshchunov, and since the equation becomes more non-linear (flux term depending on hydride volume fraction, i.e. indirectly on the hydrogen concentration itself), we have to introduce an iterative procedure like for the steady-state solution in OXIRED [14]. As alternative we can use the new thermo-diffusion model developed by K. Lassmann for oxygen, plutonium, americium and hydrogen redistribution in a temperature gradient. The new model mainly involves a new transient solution that complements the previous approximation of OXIRED. It relies on the finite difference formulae for unequal intervals based on Lagrange's interpolation with an implicit time integration.
- Diffusion in hydrides [19] can be envisaged as additional flux term for hydrogen, which should be rather trivial, but considering uncertainties pertaining to the diffusion coefficients, this can be introduced later.
- Implementation of a hydride nucleation and growth model like Passelaigue et al. in BISON [21], in order to consider growth of hydrides when the dissolved concentration exceeds the dissolution limit (but remains below the precipitation limit).
- Effect of hydrogen front penetration like Feria et al. [22]
- Effect of stress gradient
- On hydrogen diffusion (additional diffusion term) like in Jernkvist et al. [19]
- On radial hydride formation like in the paper of Feria et al. [23] and comparison with mesoscale (phase field modelling) simulations of Thuinet et al. [24]
- As mentioned above, the effect hydrogen uptake at the inner cladding radius might be considered in a future version, once this version is fully operational.
- A first set of simple tests have been carried out and are encouraging, although they must be complemented with numerous systematic test with representative conditions: both in-pile (zero initial concentration, clad outer surface temperature around 575 K, inner temperature approximately 50 K higher, hydrogen uptake due to normal oxidation), and storage conditions (non-zero initial concentration, clad outer surface temperature around room temperature or around 675 K for so-called dry-storage accidents like in [23]). This should also provide a basis for the time-step control mentioned above, and better define the limits of application of the model.
- Furthermore, a comparison with an analytical solution or the solution of Marino [9] and/or that in the technical appendix of Varias and Massih [20] should be considered, as well as a comparison with the BISON predictions for an irradiation followed by long-term storage [25], along with scenarios considered by Feria et al. [22].
- The preliminary HYREDI model presented in this work was initially planned to be further developed in collaboration with an organisation that is not involved in the R2CA project via a bilateral agreement. However, because of the unilateral cancellation of this collaboration by that partner, and in view of the

promising results obtained by Feria et al [22] in the course of the R2CA project, a new bilateral collaboration agreement between JRC and CIEMAT has been established. The objective is to implement and test the coupling of the HYDCLAD model of CIEMAT, which already accounts for the precipitation and dissolution, with the TRANSURANUS code. This coupling would be similar to that with FRAPCON [23]. Additional financial support has been requested in order to boost this collaboration with a mobility grant for a PhD student from CIEMAT to JRC in Karlrsuhe, which would also enable the code comparison for some selected LOCA cases. It is uncertain, however, whether this can be completed within the time frame of the R2CA project.

References

[1] C. Berthinier, C. Rado, C. Chatillon, F. Hodaj, Thermodynamic assessment of oxygen diffusion in non-stoichiometric $UO_{2\pm x}$ from experimental data and Frenkel pair modeling, Journal of Nuclear Materials 433 (2013) 265.

[2] C. Győri, M. Jonson, G. Robertson, P. Blair, A. Schubert, P. Van Uffelen, Extension and validation of the TRANSURANUS code in the course of the ESSANUF project (Paper 3.10), in: 12th International conference on WWER fuel performance, modelling and experimental support (INRNE, Nessebar, Bulgaria, 2017).

[3] G. Zhou, G. Wikmark, L. Hallstadius, J. Wright, M. Dahlback, L. P. Brandes, S. Holcombe, U. Wetterholm, A. Lindquist, S. Valizadeh, Y. Long, P. Blair, "Corrosion and Hydrogen uptake behavior and modeling for modern BWR cladding materials at high burnup", Proceedings of Top Fuel, Paris, France, 6-10 September.

[4] Cs. Győri, P. Van Uffelen, A. Schubert, J. van de Laar, E. Perez-Feró, E. Szabó, Z. Hózer, G. Spykman, "Model developments for the simulation of LOCA events by means of the TRANSURANUS Code ", Proceedings of 7th Int. Conf. on WWER Fuel Performance, Modelling and Experimental Support, Albena, Bulgaria, 17-21 September.

[5] M. Moalem, D. R. Olander, The high-temperature solubility of hydrogen in pure and oxygen-containing Zircaloy, Journal of Nuclear Materials 178 (1991) 61.

[6] E. Fromm, G. E., Gase und Kohlenstoff in Metallen, Springer Verlag, 1976.

[7] C. Győri, "Modelling of Hydrogen Absorption in Zr-Based Claddings under Postulated LOCA Conditions. ", in, Report for TRANSURANUS Software Licence Agreement No. 33964, NucleoCon, 2020, p. 27.

[8] T. Barani Mechanistic modeling of fission gas behavior in conventional and advanced nuclear fuel, Ph.D.-thesis, Politecnico di Milano, Italy, 2020.

[9] S. E. Lemehov, F. Jutier, Y. Parthoens, B. Vos, S. Van Den Berghe, M. Verwerft, N. Nakae, MACROS benchmark calculations and analysis of fission gas release in MOX with high content of plutonium, Progress in Nuclear Energy 57 (2012) 117.

[10] O. Courty, A. T. Motta, J. D. Hales, Modeling and simulation of hydrogen behavior in Zircaloy-4 fuel cladding, Journal of Nuclear Materials 452 (2014) 311.

[11] P. Van Uffelen, A. Schubert, Z. Soti, C. Gyori, S. Boneva, H. Hozer, L. Luzzi, P. Blair, M. Jonson, B. Hatala, J. Klouzal, M. Ieremenko, V. Peri, S. Bznuni, The application of the TRANSURANUS Fuel Performance Code to VVER fuel - An overview, in: 13th Int.Conf.on WWER Fuel Performance - Modelling and Experimental Support (INRNE, Nessebar, Bulgaria, 2019).

[12] V. Di Marcello, A. Schubert, J. van de Laar, P. Van Uffelen, Extension of the TRANSURANUS plutonium redistribution model for fast reactor performance analysis, Nuclear Engineering and Design 248 (2012) 149.

[13] V. Di Marcello, V. V. Rondinella, A. Schubert, J. van de Laar, P. Van Uffelen, Modelling actinide redistribution in mixed oxide fuel for sodium fast reactors, Nuclear Energy 72 (2014) 83.

[14] K. Lassmann, The oxired model for redistribution of oxygen in nonstoichiometric uranium-plutonium oxides, Journal of Nuclear Materials 150 (1987) 10.

[15] L. Cognini, A. Cechet, T. Barani, D. Pizzocri, P. Van Uffelen, L. Luzzi, Towards a physics-based description of intra-granular helium behaviour in oxide fuel for application in fuel performance codes, Nuclear Engineering and Technology 53 (2021) 562.
[16] F. S. Ham, Stress-assisted precipitation on dislocations, Journal of applied physics 30 (1959) 915.
[17] V. D. Marcello, A. Schubert, J. van de Laar, P. V. Uffelen, The TRANSURANUS mechanical model for large strain analysis, Nuclear Engineering and Design 276 (2014) 19.
[18] D. S. Stafford, Multidimensional simulations of hydrides during fuel rod lifecycle, Journal of Nuclear Materials 466 (2015) 362.
[19] A. Toptan, D. J. Kropaczek, M. N. Avramova, Gap conductance modeling I: Theoretical considerations for single- and multi-component gases in curvilinear coordinates, Nuclear Engineering and Design 353 (2019) 110283.
[20] M. Lainet, B. Michel, J.-C. Dumas, M. Pelletier, I. Ramière, GERMINAL, a fuel performance code of the PLEIADES platform to simulate the in-pile behaviour of mixed oxide fuel pins for sodium-cooled fast reactors, Journal of Nuclear Materials 516 (2019) 30.
[21] T. Barani, G. Pastore, A. Magni, D. Pizzocri, P. Van Uffelen, L. Luzzi, Modeling intra-granular fission gas bubble evolution and coarsening in uranium dioxide during in-pile transients, Journal of Nuclear Materials 538 (2020) 152195.
[22] P. Van Uffelen, A. Schubert, Z. Soti, Assessing the effect of some ATF materials and uncertainties on their properties under normal operation conditions by means of the TRANSURANUS code in: Pacific Basin Nuclear Conference 2022 (CNS, Chengdu, P.R. China, 2022).
[23] A. Toptan, D. J. Kropaczek, M. N. Avramova, Gap conductance modeling II: Optimized model for UO2-Zircaloy interfaces, Nuclear Engineering and Design 355 (2019) 110289.
[24] M. García, R. Tuominen, A. Gommlich, D. Ferraro, V. Valtavirta, U. Imke, P. Van Uffelen, L. Mercatali, V. Sanchez-Espinoza, J. Leppänen, S. Kliem, A Serpent2-SUBCHANFLOW-TRANSURANUS coupling for pin-by-pin depletion calculations in Light Water Reactors, Annals of Nuclear Energy 139 (2020) 107213.
[25] D. Pizzocri, Modelling and assessment of inert gas behaviour in UO_2 nuclear fuel for transient analysis, Ph.D.-thesis, Politecnico di Milano, Italy, 2018.
[26] C. G. Broyden, A Class of Methods for Solving Nonlinear Simultaneous Equations, Mathematics of Computation 19 (1965) 577.
[27] P. Van Uffelen, Cs. Győri, A. Schubert, J. van de Laar, Z. Hozer, G. Spykman, Extending the application range of a fuel performance code from normal operating to design basis accident conditions, Journal of Nuclear Materials 383 (2008) 137.

7 NINE: Independent assessment and benchmark on Secondary Hydriding modelling

In the frame of a bilateral collaboration with the JRC, C. Gyori from NucleoCon developed a model for hydrogen absorption in Zr-based cladding under accident conditions, considering both hydrogen uptake due to oxidation and gaseous hydriding ([26] in §6). The activities of NINE for Task 4.3 included a literature study of current status about hydriding modelling in TRANSURANUS, but focus on testing the TRANSURANUS model for H-uptake from NucleoCon against the data of EK (available on the R2CA share-point, and described above).

The main limitations concerning the application of such model in the specific case are due to the fact that the TRANSURANUS model was developed specifically for LOCA conditions ([27] in §6), characterised by high cladding temperatures (i.e. cladding temperature ≥ 600 °C), while the EK experimental study focused on normal operation temperatures (i.e. cladding temperature ≤ 400 °C). Such different conditions imply that the extrapolation of the model outside its temperature range should be carefully tested and verified with proper experimental data. This is also reflected in the relatively large uncertainty band on the fitted model parameters.

The model of hydrogen absorption in Zr-based claddings under postulated LOCA conditions (high temperature) due to gaseous hydriding is based on the following assumptions:

- The hydrogen uptake of the cladding is calculated as a product of the equilibrium hydrogen concentration (solubility limit) and a time-dependent factor representing the kinetics of the absorption;
- The equilibrium concentration in hydrogen atmosphere is defined through Sievert's law, considering the hydrogen partial pressure in the environment as well as the oxygen content of the metal;
- The solubility parameters have been fitted to the experimental data of FZK and AEKI (now EK), separately for Zircaloy-4 and for Zr1Nb;
- The equilibrium concentration during steam oxidation is calculated through an effective hydrogen solubility constant, since the driving phenomena in H_2 (adsorption and bulk diffusion of neutral hydrogen atoms) and in steam (proton diffusion) are assumed fundamentally different;
- The kinetics of the hydrogen uptake is controlled by chemisorption (identical kinetics parameters are considered for Zircaloy and Zr1Nb as a first approximation at this stage);
- A simple bounding approach is applied for the simulation of hydrogen uptake in steam-hydrogen mixture: The dominating process (gaseous hydriding or oxidation) is evaluated in each time step and the process resulting in the larger increase of the hydrogen concentration is considered in the actual time step.

The solubility of gases in metals under isothermal conditions is proportional to the square root of the partial pressure of the ambient gas, as described by the Sievert's law:

$$c_g = K\sqrt{p_g}$$

Where c_g is the ambient gas solubility, K is the solubility constant and p_g is the partial pressure of the ambient gas. Such law has been corrected to take into account the deviation of the equilibrium hydrogen concentration considering the decrease of the free interstitial sites in the zirconium (H/Zr atomic ratio > 0.6)

$$c_S = \frac{K_S\sqrt{p_H}}{1 + \frac{K_S}{C}\sqrt{p_H}}$$

Where C is the total number of interstitial sites for hydrogen dissolution per Zr atoms. The total number of interstitial sites for hydrogen dissolution depends on the material phase and ranges between 2, for HCP α-phase, and 6, for

BCC β-phase. Considering the Zr phase diagram, the area of interest for the EK experiments is the one highlighted in red in figure 1, i.e. α-phase only (Fig. 57).

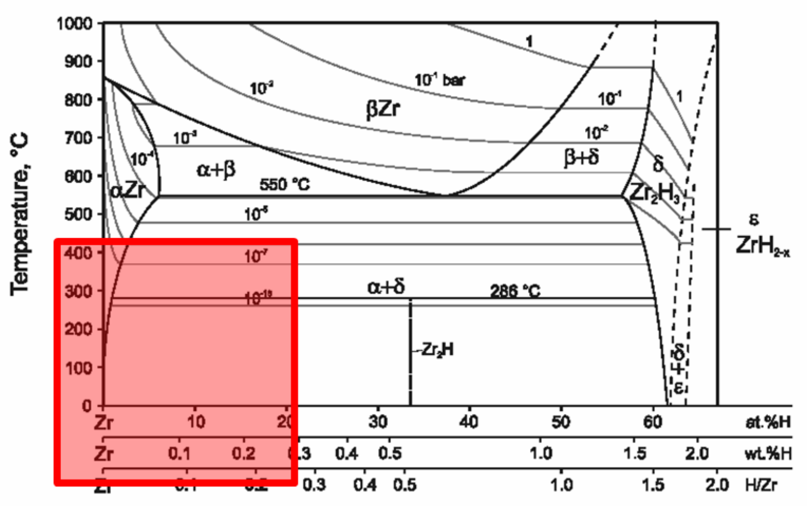

Fig. 57. Zr phase diagram with red-highlighted area of interest for EK experiments

The results of the simulations in terms of H uptake calculations are presented in Table 11 and Fig. 58. The model implemented in TRANSURANUS show better agreement with experimental data for both Zr4 and E110 materials at the lowest temperatures that seems in contrast with the modelling assumption of high temperature condition. At the highest temperatures of EK experiments, i.e. for 370 °C ≤ T ≤ 400°C, the H-uptake is over-predicted, especially for Zr4, up to factor of 7.

Table 11. Comparison of results for H uptake calculated by TRANSURANUS and experimental data of EK

	Absorbed H (ppm)	
Test	Measured	TRANSURANUS
E110 - 300°C	221	212
E110 - 330°C	907	686
E110 - 370°C	1556	2262
E110 - 400°C	2746	4846
Zr4 - 300°C	1203	760
Zr4 - 330°C	1980	2193
Zr4 - 370°C	2129	7409
Zr4 - 400°C	2188	15620

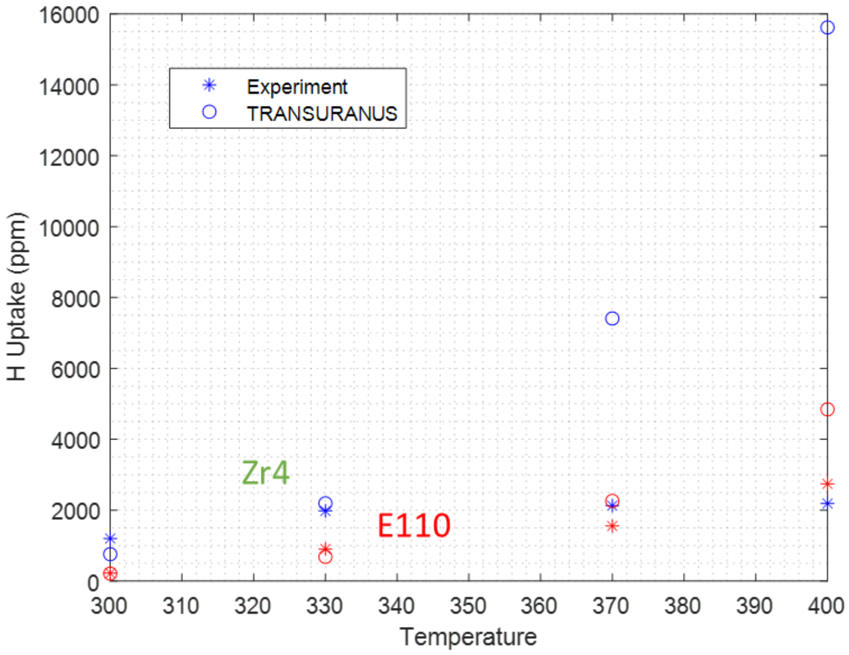

Fig. 58. Comparison of measured hydrogen uptake concentration measured at EK and the preliminary model prediction of TRANSURANUS as a function of temperature

Such results suggest that the extrapolation of the modelling parameters in much lower temperature ranges with respect to those at which they were fitted does not allow obtaining reliable results. IN the experiments of EK, only the low temperature alpha phase was present, for which a re-evaluation of the C-parameter seems necessary. Furthermore, uncertainties on activation energy for H solubility should be also re-considered at such conditions, as well as the boundary conditions for the H partial pressure with respect to the total pressure to take into account the role of Ar. It should also be pointed out that neither the presence of water nor oxygen were modelled, although a thin oxide layer was observed on the sample surface, which might have inhibited or delayed the hydrogen uptake.

8 CONCLUSION

In the frame of R2CA project, task WP4.3 focused on the study of secondary hydriding affecting defective fuel rods during normal operating conditions.

The bibliography which was carried out made it possible to update the current state of knowledge concerning the possible physical mechanisms involved in the formation of secondary defects after water ingress in a defective fuel rod. It is worth pointing out that, at the beginning of the project, the hypotheses put forward to explain the whole phenomena were only qualitative and very few data were available. No simulation tools were available either concerning normal operating conditions, at least for PWRs. Within the project, a scenario for secondary hydriding modelling has been proposed based on the main following physical mechanisms identified:

- Internal gas transport in the free volume of the fuel rod
- Internal oxidation
- Hydrogen uptake
- Hydrogen redistribution with the cladding

The objectives were to update or implement the identified models in the available simulation tools such as fuel performance codes (TRANSURANUS (JRC), FRAPTRAN) or fuel rod simulation code SHOWBIZ (IRSN). Depending on the degree of maturity of the models, prototypes or standalone models have been envisaged prior to a further implementation in the simulation codes.

Concerning internal gas transport in the cladding-pellet gap, a first approach was to test a diffusional gas transport model in a standalone model giving encouraging results. The second approach was to consider both a diffusional transport and a forced-convection model where the transport is driven by pressure differences. The use of Darcy's law appeared relevant for considering the gas transport through the cracks and open porosities of a fuel rod with a closed pellet-cladding gap. A modified Darcy's law also allows for modeling the water ingress due to the difference between internal rod pressure and PWR coolant pressure at the occurrence of the primary defect.

Internal oxidation of the cladding was supposed to be the main mechanism for dihydrogen creation inside a defective fuel rod. Oxidation of the fuel pellet has been neglected. Few data are available in the literature for oxidation of zirconium alloys by a vapor / hydrogen mixture at PWR coolant temperature. The kinetics proposed by Lee et al. for different hydrogen to vapor ratio at relevant temperatures was used.

Another scientific challenge was to characterize the hydrogen uptake by the cladding material at representative PWR coolant temperatures. To face the lack of data at relevant temperatures, hydrogen uptake tests have been carried out on Zr-alloy cladding tube samples between 300 and 400°C. These data have been used to establish a simple correlation for hydrogen uptake based on the hydrogen partial pressure. A more mechanistic approach was tested by deriving the Sievert model valid at higher temperatures (LOCA representative temperatures) but the applicability at lower temperature is still subject to discussion.

The hydrogen redistribution within the cladding is the driving and key phenomena for the formation of a secondary defect (blister). Different models were derived during the project.
First of all, a model for the radial redistribution of hydrogen absorbed in zirconium cladding, under the influence of the concentration and temperature gradients, has been implemented first in the TRANSURANUS code.
A stand-alone external model for was also derived from the Hydrides Nucleation-Growth-Dissolution model and coupled with FRAPTRAN. This model was shown to be able to reproduce the formation of a hydride blister. This model will be further implemented in the TRANSURANUS code or used to improve the SHOWBIZ modelling of the hydrogen precipitation.

Finally, for the first time, a preliminary calculation of the whole secondary hydriding phenomena in a defective PWR fuel rod have been performed, from the water inlet to the formation of a hydride blister. With the hypothesis of a primary defect located at the bottom of the fuel rod, the modelling is able to reproduce the formation of a secondary defect 2 meters above after 30 days. However, uncertainties still remain on the kinetic of the internal oxidation of the cladding and the kinetic of hydrogen pickup from a hydrogen and vapor atmosphere. It is therefore difficult to quantitatively estimate the global kinetics of the fuel rod degradation. That is why, even if a failure criterion could be proposed based on the hydride blister thickness and from mechanical analysis on the remaining clad thickness, it is still too premature to propose a best estimate failure criterion.